ANALYSIS AND SYNTHESIS OF PRECISION RESOLVER SYSTEM

NAY LIN HTUN AUNG
(B.Eng, YIT, M.Eng, NUS)

A THESIS SUBMITTED

FOR THE DEGREE OF DOCTOR OF PHILOSOPHY
DEPARTMENT OF ELECTRICAL AND COMPUTER ENGINEERING

NATIONAL UNIVERSITY OF SINGAPORE

2015

DECLARATION

I hereby declare that the thesis is my original work and it has been written by me in its entirety. I have duly acknowledged all the sources of information which have been used in the thesis.

This thesis has also not been submitted for any degree in any university previously.

NAY LIN HTUN AUNG

01 DEC 2015

Acknowledgements

First and foremost, I would like to express my gratitude to my co-supervisor, Adjunct Associate Prof. Bi Chao from Data Storage Institute, for his guidance, in-depth knowledge, support and encouragement during the course of this work. I would also like to thank my main supervisor, Associate Prof. A. Al. Mamun from department of Electrical Computer Engineering, National University Singapore, for his valuable suggestions and critical review of my work.

I would like to thank for all the help I have received from my colleagues, Mr. Lim Choon Pio, Dr. Jiang Quan, Dr. Lin Song, Dr. Hla Nu Phyu and Dr. Yu Yinquan, from the motor team in Data Storage Institute, who helped me one way or another.

Special thanks go to my wife, Ma Tin Lay Nwe, mother of my lovely daughter, Khaing Nay New, for her consistent support and encouragement till I complete this dissertation.

I wish to acknowledge the opportunity of pursuing a PhD by providing tuition fee support and a yearly book allowance in the form of Scientific Staff Development Award (SSDA) offered by Agency for Science Technology and Research (A*STAR) .

Table of Contents

Summary

A resolver is an absolute electromagnetic transducer that converts shaft angle to analog signal. Resolvers have been widely used in industrial and defense applications which rely on accurate angular position feedback. This thesis presents a detailed investigation into the improvement of accuracy in a resolver system. The aims of the thesis are to identify the factors that influence the accuracy of the resolver system, to develop techniques to improve the resolver accuracy and to develop a low-cost but reasonably accurate resolver.

The investigation covers the areas of demodulation, calibration, error detection and compensation in resolver to digital conversion (RDC), and development of axial brushless resolvers.

A demodulation technique based on synchronous integration of the amplitude modulated resolver outputs is developed. Due to integration, the noise and disturbance effects are averaged out and the achievable accuracy is improved without the need of applying filters. The effectiveness of the method is demonstrated with the experimental data using a commercial resolver operated at a spin-stand.

Due to resolver imperfections, RDC designed for ideal resolver signals results in position errors. Formulation is done to predict the error characteristics if RDC uses direct inverse tangent method and the results are compared and validated with the angle tracking method.

A method for initial calibration of a resolver by using Discrete Fourier Transform and Least Squares method is proposed in this work. In addition, an error model based on complex Fourier expression of position angle signal is used to detect the error parameters of a resolver on real time and error compensation is achieved by using the integration loops together with amplitude tracking loop. Experimental results show

that the calibration is effective and the compensation technique is able to obtain the accurate position with a small error.

Requirements of precise manufacturing and special electromagnetic structure make the conventional brushless resolvers expensive. Reduction of cost without degradation of performance is a challenging problem in resolver design. It demands for novel and innovative design techniques to be explored. Final part of this thesis is devoted to the systematic design procedures for axial resolvers based on PCB technology. The procedures include determination of winding configurations and performance comparison of various coil shapes. Two-phase and three-phase resolvers with six-layer PCBs are fabricated using this novel technique and their performances are evaluated. It is shown that the fabricated resolvers can be used to replace the conventional types depending on application.

List of Tables

List of Figures

1 Introduction

1.1 Background

Feedback control is necessary in almost all modern control systems, and the performance of a system highly depends on its sensing devices which give feedback to the control unit. Various types of sensors are used to measure the parameters of interest in those applications. The shaft angular displacement or position is an essential parameter in rotary motion systems. The two common types of sensors employed in measuring shaft position are resolvers and encoders. In principle of operation, resolvers employ electromagnetic induction whereas encoders can be mechanical, inductive, capacitive or optical. The most common type of encoder is the optical encoder. Based on signal format of the sensors' direct outputs, it can be noted that resolvers provide analog outputs while optical encoders typically provide digital outputs. In addition, the two types of sensors are classified according to the nature of the position information they provide. Resolvers deliver the absolute angular position. Encoders' position information can be incremental or absolute, but the incremental encoders are more common. Absolute angular position sensor can provide the current position of the shaft immediately after the sensor is powered. On the other hand, incremental types provide the information about change in position or the relative position. For the incremental type, homing or a reference positioning is required to retrieve the current position of the shaft.

When a choice is to be made between the two types, resolvers are usually preferred for applications requiring mechanical robustness and reliability over extremely long operational lifetimes [1]. Resolvers have been widely used in industrial and defence applications which rely on the feedback of accurate angular position sensing systems [2], for example, in servo drives used in extreme environments like strong vibration, fog and smoke condition, and high temperature

[3]. In these environments, it is difficult to use optical encoders. When considering motors for servo drives, permanent magnet synchronous motors (PMSM) are well suited due to their low inertia, high energy and small motor size. In order to drive a PMSM, the rotor position information is required all the time to control the three phase currents. This kind of motors can be found in many applications like robotics, machine tools, radars, satellites, and electric vehicles. Recently, emergence of electric vehicles and industrial automation with robots have also drawn more developments in various types of new rotary position sensors [4~ 5].

1.2 Rotary encoders

An encoder's main function is to detect an encoded pattern. Decoding the pattern will generally result in the desired position information. There are different types of rotary encoders based on different physical principles such as mechanical, optical, capacitive or inductive. For non-contact shaft position measurement in PMSM drives, optical encoders are commonly used. An optical rotary encoder comprises a stationary light source, a disk with encoded pattern mounted on a rotatable member and a stationary detecting member to sense the changes in the pattern. These changes resulting from motion of the rotating member are sent out as digital pulses to the external electronics, where these pulses are used to retrieve the position information. This operating principle requires the precise alignment of the components in the encoder.

The encoded pattern on the disk determines whether an encoder is absolute or incremental and the disk can be made with steel, glass or plastic. Absolute encoders have complex pattern and they are usually more expensive than the incremental. The output of an absolute encoder is multi-bit digital signal requiring a multi-wire connector. The accuracy of an encoder increases with increased number of bits and therefore more wires in the connector. Encoder resolution and accuracy depends on the number of tracks on the coded disk. With integrated semiconductor techniques for

etching the glass disk and aligning the detectors, pulse per revolution (PPR) over 10,000 with exceptional precision can be achieved [6]. Recent developments report that optical encoders can even be realized up to 225,000 PPR [7].

Since the materials and the structure used in optical encoders are not rugged, the optical encoders generally cannot withstand excessive shock or strong vibration and the environment that can contaminate the code disk. Moreover, since the decoding electronics is usually integrated inside an encoder, the performance of the encoder is not tolerant to extreme temperature changes. However, the electronics required to convert encoder signals to digital position format are simple and generally supplied as part of the encoder. This makes encoders attractive for implementation in servo drives.

1.3 Synchros

The description of resolvers is not complete without synchros. The predecessors of resolvers are the synchros which are primarily used for transmitting the position angle information from one place to another. In general, synchros operate in a pair: a transmitter and a receiver. Because of their reliability, accuracy, ruggedness, and compact size, synchros are found in weapon systems and navigation systems of navy and aerospace equipment [8].

Based on their operation, syncrho systems are categorized into two groups: torque systems and control systems. In torque systems, the transmitter converts mechanical input, which can be the position of a shaft, to electrical signals and transmits the position information embedded electrical signals to the receiver. The receiver then converts the received electrical signals into a mechanical output, the torque, to position the light loads such as dials, pointers, or similar indicators. A typical setup of a torque synchro system is provided in Figure 1.1. In control systems, similar operation is carried out but the synchros are employed together with the servo systems to move the heavy loads such as gun directors, radar antennas and missile

launchers. Synchros are also classified according to their input, output and operating frequency.

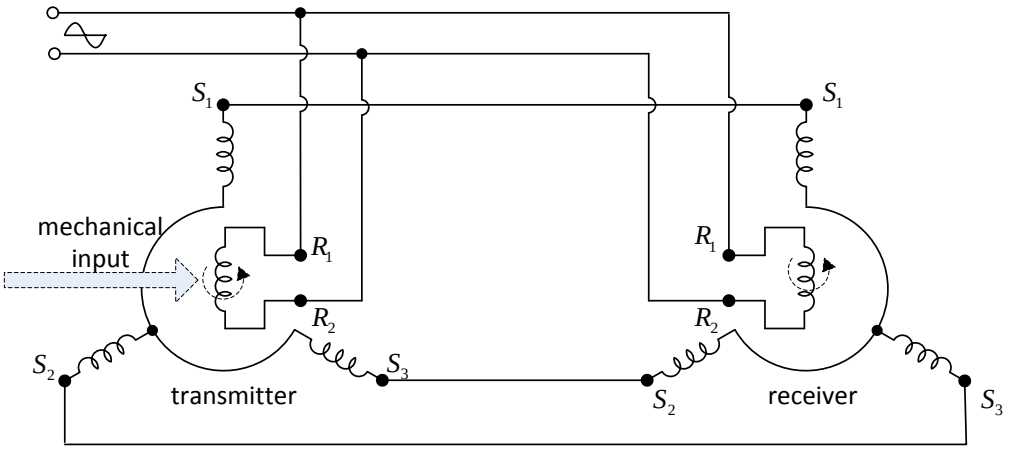

Figure 1.1. A typical torque synchro system

Synchros are rugged and reliable because their construction is the same as that of electrical machines, which are the workhorse of industry. A synchro comprises two parts: the rotating part, rotor and the stationary part, stator. The materials used for stator and rotor are laminated iron sheets and copper magnet wires. These are the same materials used in electrical machines, and a synchro therefore shares the merits of an electrical machine.

From its construction and operation, a synchro can be described as a rotary transformer with variable coupling. The amplitude of the output voltages of a synchro varies with respect to the rotor position due to the variation in electromagnetic induction coupling between the windings on rotor and stator. The position relationship between the stator and rotor windings is defined in the schematic diagram. In a general transmitter type synchro, shown in Figure 1.1, the stator has three Y-connected windings whose magnetic axes are 120degrees apart to one another, and the rotor has one single winding. The rotor winding is energized by an external alternating voltage source via slip rings and brushes, and it acts as a primary

winding of the transformer. Due to electromagnetic coupling, rotor position dependent voltages are induced in the stationary secondary windings on the stator.

When an excitation voltage, $V_{R1\text{-}R2}\sin(\omega t)$, is applied to the rotor winding, the three output voltages across the stator winding terminals may be described by

$$\begin{aligned} V_{S3-S1} &= NV_{R1-R2}\sin(\omega t)\sin\theta \\ V_{S2-S3} &= NV_{R1-R2}\sin(\omega t)\sin(\theta+120^\circ) \\ V_{S1-S2} &= NV_{R1-R2}\sin(\omega t)\sin(\theta+240^\circ) \end{aligned} \tag{1.1}$$

where N is the transformation ratio of the transformer and θ is the shaft position angle. For the sake of simplicity, resistance of the windings and motion induced electromotive forces (emfs) in the windings are not considered in these equations. This relationship shows that the induced voltages in the stator windings have the shaft position information in the form of a balanced three phase power system. When the syncrhos are operated in pairs, any unbalance in the interconnected three phase system due to a change in rotor position of the synchro transmitter will be automatically eliminated by the synchronous motion of the rotor of the synchro receiver. This automatic synchronization ability is found to be very useful in many mission critical applications, such as navy and aerospace systems.

Synchros can also be used as angular position transducers for positioning control applications. In this case the three-phase outputs are converted into two-phase format using a Scott-T transformer, and the angular position is retrieved from the two converted outputs. An angle estimation process requires an electronic interface to retrieve the position information and convert it into digital format. To use a syncro as a standalone rotary position sensor is more costly and complicated than a resolver due to conversion of three-phase to two-phase outputs.

1.4 Resolvers

Resolvers can be considered as a two-phase variant of synchros and they are practically suitable to be used as absolute angular transducers. For the shaft position sensing, they can be employed as stand-alone rotary position sensing devices. A typical schematic winding diagram of a basic resolver is shown in Figure 1.2.

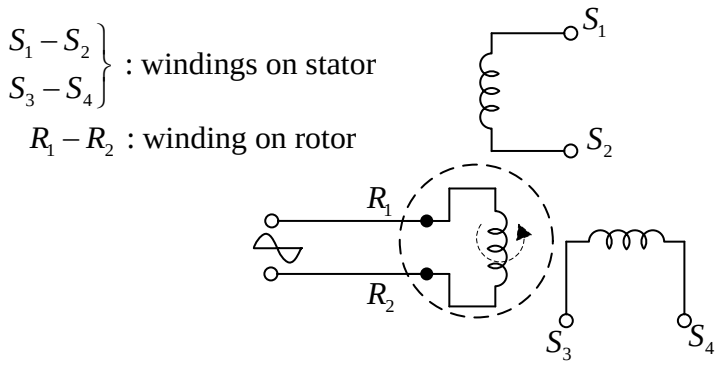

Figure 1.2. Resolver schematic winding arrangement

In resolvers, the stator has two separate windings which are displaced mechanically 90 degrees phase difference in the space. It should be noted that a resolver has four output terminals whereas a synchro has three output terminals. When an alternating voltage, $V_{R1\text{-}R2}\sin(\omega t)$, is applied to the rotor winding, similar to the equations described in synchros, the induced quadrature voltages in the stator winding may be given by:

$$\begin{cases} V_{S1-S2} = NV_{R1-R2}\sin(\omega t)\sin\theta \\ V_{S3-S4} = NV_{R1-R2}\sin(\omega t)\cos\theta \end{cases}. \tag{1.2}$$

From the vector analysis, one can realize that the two outputs represent the resolved components of a rotating position vector. On the other hand, it can be observed that a resolver transforms the polar coordinate components to the Cartesian coordinate components. For this capability, resolvers were originally used in

trigonometric computation and coordinate transformation in military applications. They can also be used as pairs, (i.e., a transmitter and a receiver), as in syncrhos depending on the applications. In the case of such applications, resolvers are called synchro resolvers.

1.4.1 Principle of resolver operation

Same as the operation of synchros, resolvers operate based on the principle which is described in Faraday's law of electromagnetic induction. The mathematical expression of Faraday's law can be given by

$$e(t) = -\frac{d(\phi N)}{dt} = -\frac{d\psi}{dt} \tag{1.3}$$

where, *e(t)* is the induced emf, ϕ the flux, *N* the number of turns of the winding and ψ the flux linkage linked with the winding. In words, it states that an emf is induced in a medium when the magnetic flux linkages associated with the medium is changed. This principle is well known in operation of a transformer where both primary and secondary are stationary. However, in resolvers, the primary side can be rotated and the secondary side is fixed. Therefore, the operation of a resolver is more close to that of a rotary transformer with two secondary windings which give the quadrature format outputs.

In general, a transformer transfers electrical energy from one circuit to another by electromagnetic induction. For the maximum power transfer, the primary and the secondary windings have to be closely wound to obtain the maximum flux coupling. However, a rotary transformer has an inherent gap between the primary and secondary. Because of this gap, the B-H loop of a rotary transformer is similar to that of an inductor. This gap also results in a high reluctance path which in turn causes a low primary magnetizing inductance. This low primary inductance leads to high

magnetizing current. Therefore, the rotary transformer does not share any distinguished features of an ideal transformer [9].

Furthermore, although resolvers have magnetic structure similar to rotary transformers, they are used to transfer the signal. The secondary side of a resolver is normally connected to a high impedance electronic circuit interface board, and the load current in the secondary winding can be negligible. The operating condition of a resolver is therefore like a transformer with open-circuited secondary windings. For this reason, a resolver can be simply described as a rotatable variable inductor according to its functionality.

Based on the desired accuracy, resolvers are also available in two types: single speed and multispeed. Single speed resolvers have two output windings and multispeed resolvers have an extra pair of windings, and hence multispeed resolvers have a total of four output windings. The extra pair of windings provides the quadrature outputs as in a single speed resolver's outputs. In a single speed resolver, the demodulated output frequency is the same as the rotor frequency. However, in a multispeed resolver, the frequency of the demodulated outputs from the extra pair of windings is several times higher than the rotor frequency depending on the number of poles applied in its electromagnetic structure. Multispeed resolvers can have the accuracy of a few arc-seconds [10].

1.4.2 Excitation for resolvers

In the early developments of resolvers, power to a resolver is provided using slip rings and brushes [10]. This generates electrical noise and shortens the resolver lifetime. To provide excitation to the resolver primary winding in a brushless way, conventional resolvers later used axial rotary transformers in place of slip rings and brushes. Figure 1.3 shows a cut-away view of an axial type rotary transformer. This results in the development of commonly known brushless resolvers. There is another

type of resolvers, so called variable reluctance resolvers, whose outputs vary based on reluctance changes due to the specially shaped rotor without windings. In variable reluctance resolvers, a rotary transformer is not required for excitation power supply. These two types of resolvers are introduced in the following sections.

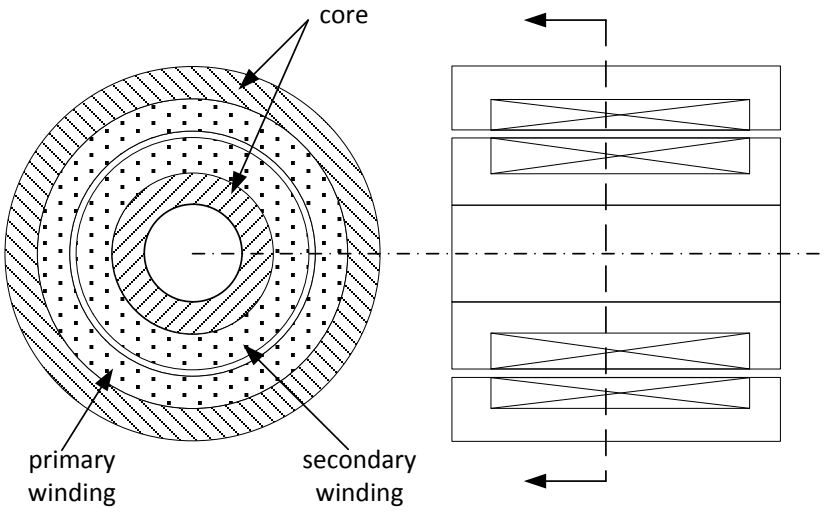

Figure 1.3. Rotary transformer for resolver excitation

1.4.3 Brushless resolvers

In view of electromagnetic structure, the brushless resolvers can be described as two rotary transformers which are connected in series. A schematic windings arrangement of a brushless resolver is shown in Figure 1.4. The first transformer is to supply exciting signal to the resolver and the second is to convert the shaft position into electrical signals. As the purposes of the two transformers are different, the design and construction of them are also different. The first transformer T_1 is essentially a general rotary transformer and it is designed to operate in the frequency range (from 400Hz to 20kHz) [10]. It is used to transfer the power to the constant load which is the resolver primary winding R_1-R_2. The second transformer, which is a sensing part of the resolver with windings S_1-S_2 and S_3-S_4, is used to transfer the signal and its outputs vary with respect to the position of the shaft. The construction of the sensing transformer is similar to a small electrical machine. The rotor of the

sensing transformer, where the primary windings are allocated, is a wound field rotor. This type of rotor is commonly found in wound-rotor induction motor and synchronous motor. The stator has a cylindrical structure of slotted laminations where the two secondary windings S_1-S_2 and S_3-S_4 are displaced mechanically 90 degrees apart. It can be observed that variation in magnetic coupling, or variation of mutual inductance between the primary and secondary windings in a brushless resolver is due to the relative position of the windings.

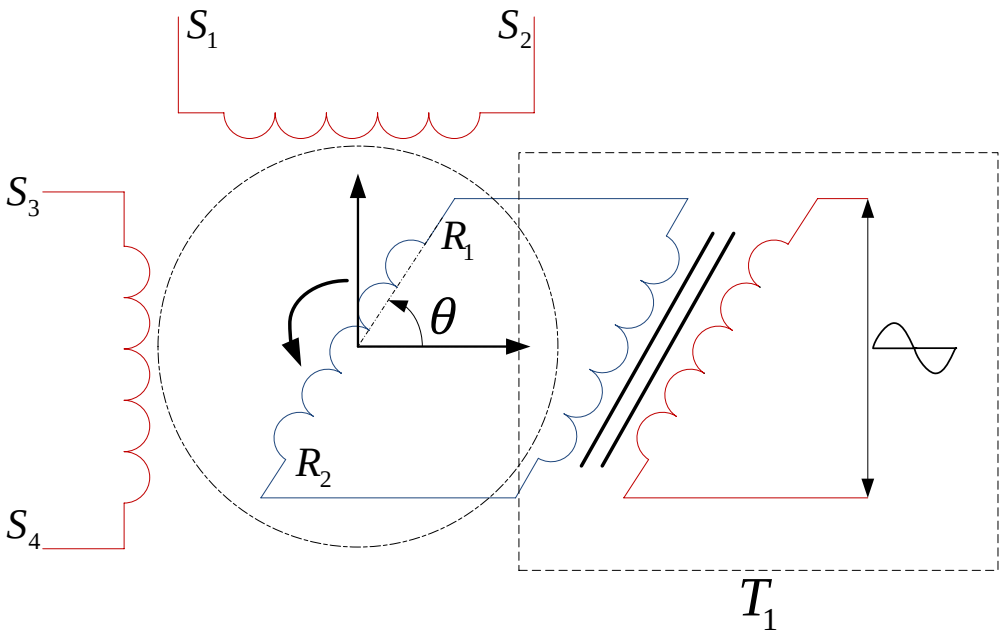

Figure 1.4. Schematic winding diagram of a brushless resolver

The combination of two different structures makes the brushless resolvers expensive as the manufacturing process requires different parts and procedures for assembly. On the other hand, the cascaded structure makes it difficult to shorten the axial length when a low profile design is required.

1.4.4 Variable reluctance resolvers

In order to produce resolvers with low cost and simplified structure, there was a need for alteration in electromagnetic structure of brushless resolvers. Variable reluctance (VR) resolvers were developed to fulfil this requirement. VR resolvers overcome the main shortage of brushless resolvers by allocating the primary winding of resolver sensing transformer to the stator side. Now both the primary and secondary windings of resolver reside on the stationary part. By doing so, the power required for excitation can be supplied directly to the stator from the external source. A typical schematic winding diagram of a two-pole VR resolver is shown in Figure 1.5. To achieve the shaft position dependent electrical outputs, the electromagnetic induction principle is used as before. Unlike brushless resolvers, the variation in induced emfs at the stator is due to the reluctance variation from the specially shaped rotor having salient poles. This can be explained by (1.3) together with the relationship between the flux and the magnetic reluctance as:

$$\phi = \frac{Ni}{R_m} = \frac{Ni\mu A}{l} \ , \tag{1.4}$$

where Ni is the magneto-motive force, R_m the magnetic reluctance of the magnetic passage, l the length of the air gap, and A the cross sectional area of the air gap. In this case, variation in magnetic coupling is due to variation in air gap length. If the winding resistances, motional induced emfs and direct flux linkages from primary to secondary windings are ignored, VR resolvers provide the same output signals as brushless resolvers do.

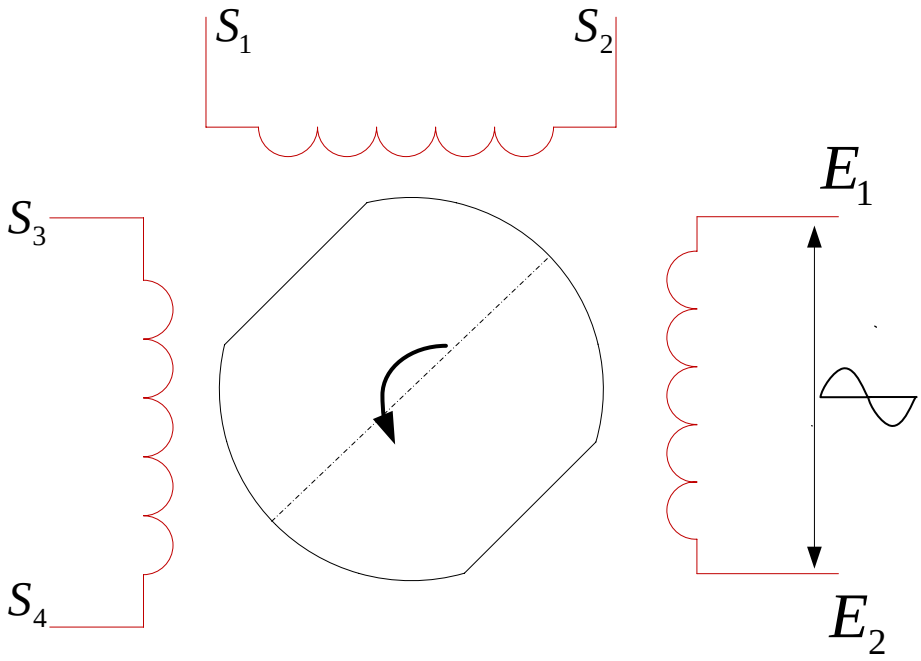

Figure 1.5. Schematic winding diagram of a VR resolver

Due to simplicity of the structure and no separate transformer for excitation, the manufacturing cost of the reluctance resolver is reduced. In addition, it makes low profile resolvers feasible. In electric vehicles, VR resolvers are gaining high acceptance due to easy integration to the engines and suitability to the operating environment [11]. However, the accuracy of VR resolvers is not as good as that of brushless resolvers [12].

1.4.5 Retrieving the position angle from resolver

Without considering the effects of winding resistances and motional induced electromagnetic force (emf), the resolver output voltages can be expressed by (1.2). This set of simplified equations resembles the modulated signal in double-sideband amplitude modulation (DSB-AM) in electronic communication. With this analogy, the excitation signal in a resolver is a carrier or reference signal and the position

signal is the modulating signal. The ideal resolver outputs are then modulated quadrature signals. Figure 1.6 illustrates the ideal input and output signals of a resolver.

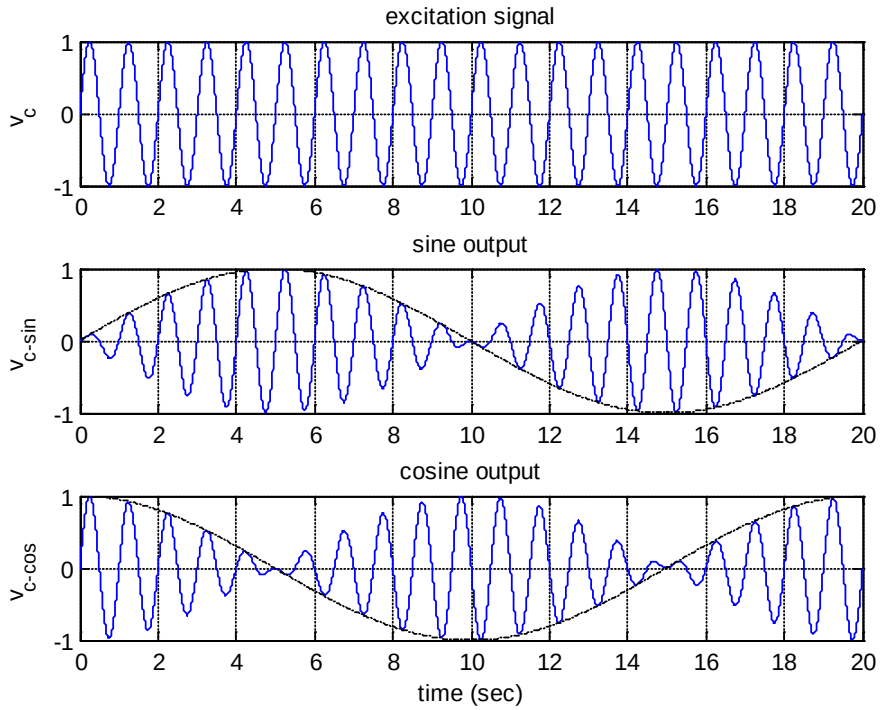

Figure 1.6. Resolver's input and output signals

To retrieve the position angle from resolvers requires two steps. The first is to demodulate the resolver outputs to recover the envelopes that represent the quadrature position signals. The second is to compute the position angle. The retrieving process of resolver signals to digital position angle value is usually referred as resolver to digital conversion, and the electronics interface that performs the conversion is known as resolver to digital converter (RDC).

1.4.5.1 Demodulation of resolver signals

The demodulation or the envelope recovery can be achieved by using either peak detection or product detection. Both methods require the excitation signal in the

process. The peak detection method is based on the fact that when the excitation signal reaches at its maximum point, the output voltages are just the sine and cosine to shaft position angle multiplied by the product of transformation ratio and peak amplitude of the excitation signal. This can be described as

$$\begin{cases} V_{S1-S2}\big|_{\sin(\omega t)=1} = NV_{R1-R2}\sin\theta \\ V_{S3-S4}\big|_{\sin(\omega t)=1} = NV_{R1-R2}\cos\theta \end{cases} \tag{1.5}$$

In order to implement this method, it requires a way to generate a trigger signal at the peak of the excitation signal so that sampling can be performed at this right instant. This sampling instant is the optimal one because the noise effect is the least and the motional induced emf, which is in quadrature to the excitation signal, is minimal at this point.

The product detection, which is another common method of demodulation, is based on the frequency shifting concept. The operation block diagram of the method is shown in Figure 1.7.

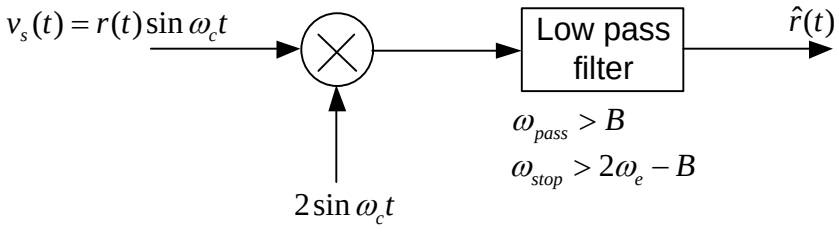

Figure 1.7. Demodulation by product detection

By multiplying the modulated signal with its own carrier signal, the high frequency carrier signal is shifted to the twice of its original frequency in the frequency band. Filtering the high frequency component with a low pass filter results in the base band signal, which is the desired position signal represented by the

envelope of the modulated signal. It is assumed that modulated signals and the carrier signal are in phase in this approach.

1.4.5.2 Computation of position angle

Open loop approach

Once the demodulated signals are received, the rest is to compute the position angle. The simple and straight forward approach is to take the inverse tangent of the ratio of the two demodulated signal as

$$\theta = \begin{cases} \tan^{-1}\left(\frac{v_s}{v_c}\right) & if\ v_c \geq 0 \\ \tan^{-1}\left(\frac{v_s}{v_c}\right) + \pi & if\ v_c < 0 \end{cases}, \tag{1.6}$$

where v_s and v_c are demodulated resolver outputs from sine and cosine winding respectively. This approach is considered to be open-loop computation and it is sensitive to noise.

Closed loop approach

The closed loop computation, which is less sensitive to noise, is based on the sine of the subtraction of two angles as below:

$$\sin(A-B) = \sin(A)\cos(B) - \cos(A)\sin(B). \tag{1.7}$$

If (A-B) is small enough, we can linearize the above relationship into

$$\sin(A)\cos(B) - \cos(A)\sin(B) \approx A - B. \tag{1.8}$$

Suppose that we have an estimated angle, $\hat{\theta}$, and assume $NV_{R1\text{-}R2}=1$ in (1.5) without losing generality, using the above relationship, we obtain the difference between the true angle and the estimated angle, which is as an error term represented by

$$\varepsilon = (\theta - \hat{\theta}) \approx \sin(\theta)\cos(\hat{\theta}) - \cos(\theta)\sin(\hat{\theta}). \tag{1.9}$$

Minimizing this error is equivalent to making the estimated angle equal the true angle. And hence the true angle is obtained. The conventional RDCs employ this type of computation together with the demodulation as shown in Figure 1.8. Consider that the current position output is $\hat{\theta}$. The input modulated signals, $v_{c-\sin}$ and $v_{c-\cos}$, are multiplied by $\cos\hat{\theta}$ and $\sin\hat{\theta}$, respectively. The difference of these two results is then demodulated as in product detection method and we obtain the error signal, $\sin(\theta - \hat{\theta})$. This error is fed to the integrator, yielding the angular speed. Finally the voltage controlled oscillator (VCO) converts the speed signal into the position estimate. This type of tracking converter is commonly referred as an Angle Tracking Observer (ATO). Tracking operation is in fact the same as the phase-locked-loop operation in a tracking mode. The closed loop approach results in not only the angular position but also the angular speed.

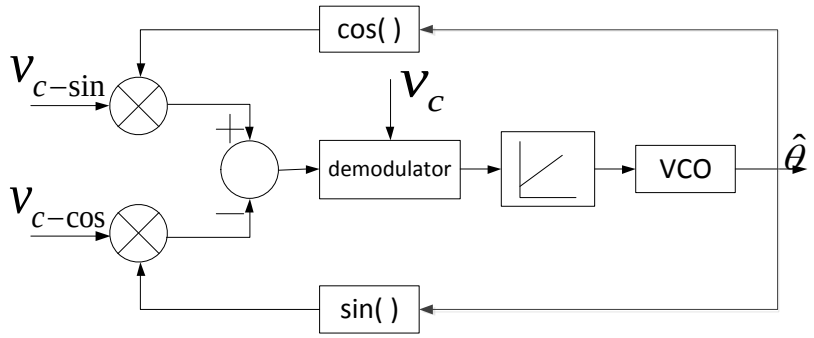

Figure 1.8. Blok diagram for a conventional RDC

1.4.6 Resolver specifications

The performance of a resolver can be specified using the following main parameters:

- Accuracy
- Transformation ratio

- Null voltage
- Phase shift
- Impedances

1.4.6.1 Accuracy

For every sensor, accuracy is the very first parameter of interest. Since a resolver gives an analog output, its theoretical resolution is infinite. Therefore, the useable resolution depends significantly on the implementation of conversion unit. On the other hand, accuracy of a resolver depends both on resolver itself and the conversion unit. Besides, accuracy can be affected by imperfect installation. In general, accuracy determines a sensor's degree of absolute correctness. In applications of resolver for angular position measurement, it refers to how much the angle obtained from the resolver system deviates from the actual angle. Since a resolver's direct outputs are nonlinear, accuracy is not a single value for all positions. The worst case accuracy is the meaningful accuracy to be defined.

When a resolver is in operation, the two demodulated outputs are quadrature sinusoidal signals. It means that when one signal reaches its maximum, the other is at its minimum. It can be reasoned that the accuracy at this position is usually expected to be the worst due to residual voltages, and the error at this position is referred as the inter-axis accuracy. In one revolution of a resolver, there are four such positions: 0 degree, 90 degrees, 180 degrees and 270 degrees. These positions are known as null positions of a resolver. Depending on perfectness of resolver's construction and installation, the accuracy may not be the same for all four null positions.

It should be noted that the outputs of a resolver are generated from the whole magnetic field induction in the device. It means that the accuracy of a resolver is tolerant to small local defects because the effects due to these defects could be neutralized when all the effects are combined to produce the final outputs. So it can

be said that the accuracy of a resolver is related to the global effect while the accuracy an encoder would be dependent on the local effects. In encoder applications, jitter in the output pulses is common and it is generated by the local defects.

1.4.6.2 Transformation ratio

In an ideal transformer, the total voltage induced into the secondary winding is determined by the number of turns in the primary to the number of turns in the secondary because windings can be tightly wound. The coupling coefficient in this case is unity. But in a real resolver, the coupling coefficient is always less than unity, and it depends on winding turns, separation between the windings, electromagnetic materials, saturation state and structure of the resolver. The transformation ratio for a resolver is defined as the ratio of output voltage to input voltage when the output is at maximum coupling. Transformation ratio for general resolvers can be in the range of 0.1 to 1.0. The transformation ratio is a parameter to be examined for RDCs when considering the generation of excitation signal and the acquisition of resolver.

1.4.6.3 Null voltage

Null positions in a resolver have been introduced when the accuracy parameter is described. Null voltage is the residual voltage remaining when the winding output is supposed to be zero at the inter-axis positions as shown in Figure 1.9. This voltage is associated with the perfectness in resolver construction and it is usually non-zero in all resolvers. The existence of a null voltage is illustrated in Figure 1.10. Depending on size, input voltage and input frequency, the total null voltage is approximately 1 to 3 millivolts per volt of input voltage [10].

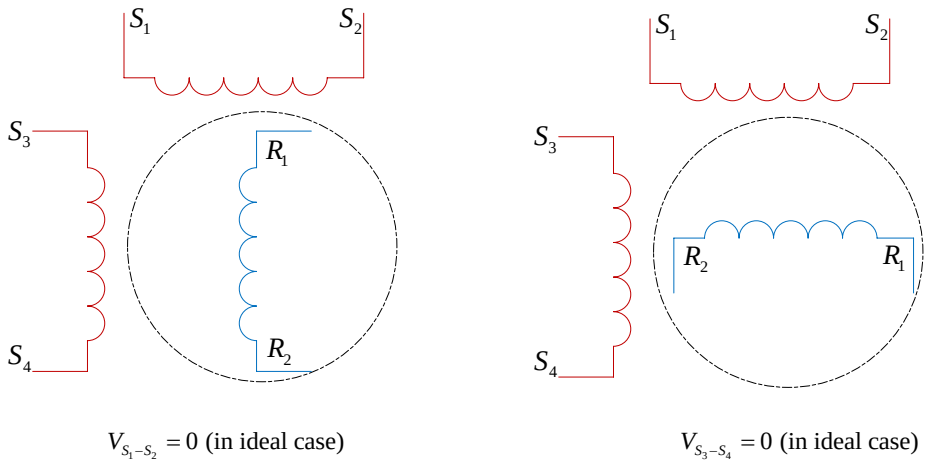

Figure 1.9. Inter-axis positions

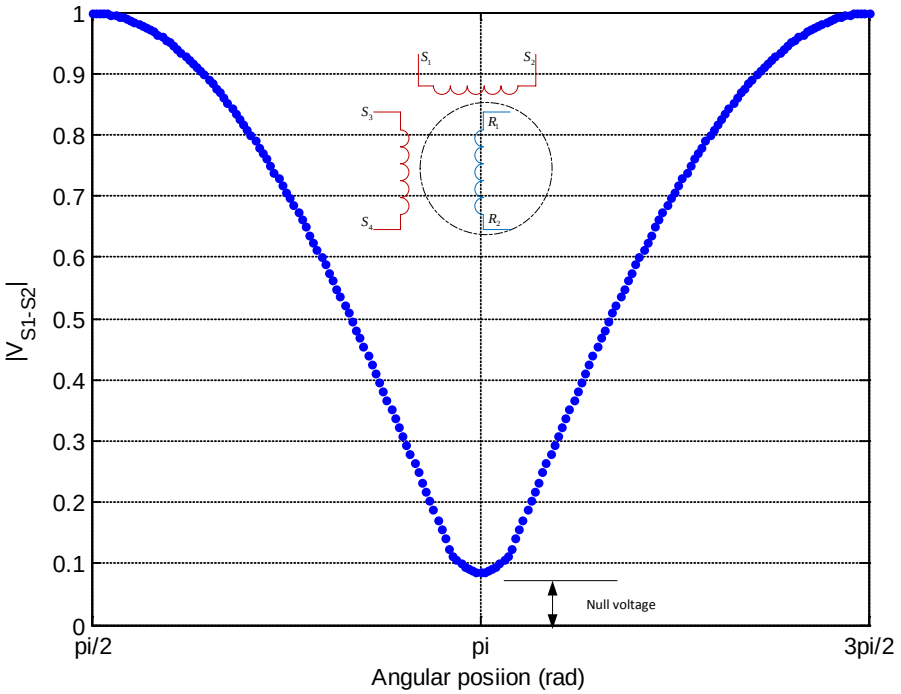

Figure 1.10. Null voltage

1.4.6.4 Phase shift

In a real resolver, the resistance of the windings cannot be neglected. A brushless resolver always has voltage drops due to resistance in both primary and secondary

windings of excitation transformer, and the primary winding of sensing transformer. A reluctance resolver has voltage drop in primary winding for excitation. These resistances can cause a phase shift between the resolver input voltage and output voltage. Phase shift for a resolver is defined as the phase difference between the input voltage and output voltage when the windings are at maximum coupling. Generally, single speed resolvers have leading phase shifts between 0 degree and 20 degrees [10].

1.4.6.5 Impedances

In order to interface with RDC or investigate the characteristics of a resolver, the information about impedances of a resolver are required. Like in transformers, resolver impedances are defined for both input and output in open and short circuit conditions. However, since the impedance is frequency dependent, only the impedances at the rated frequency are usually provided.

1.4.7 Linear resolvers

The aforementioned resolvers are known to be of non-linear type because their demodulated outputs are sinusoidal with respect to the shaft position. Nonlinear quadrature outputs can result in nonlinear sensitivity or resolution especially around when one output is at its maximum or minimum. It is obvious that processing of the linear outputs is computationally less expensive and more convenient than that of the nonlinear outputs. For sensor applications, linear outputs are preferred since they simplify the operation process. Hence the development of efficient techniques to linearize the resolver demodulated outputs has been one of the active research topics related to resolvers. A lot of efforts have been done by researchers, and several solutions have been used in industry. For example, with the same electromagnetic structure of a conventional resolver with the winding arrangement shown in Figure 1.11, the resolver can be operated as a linear device in a specific angular range.

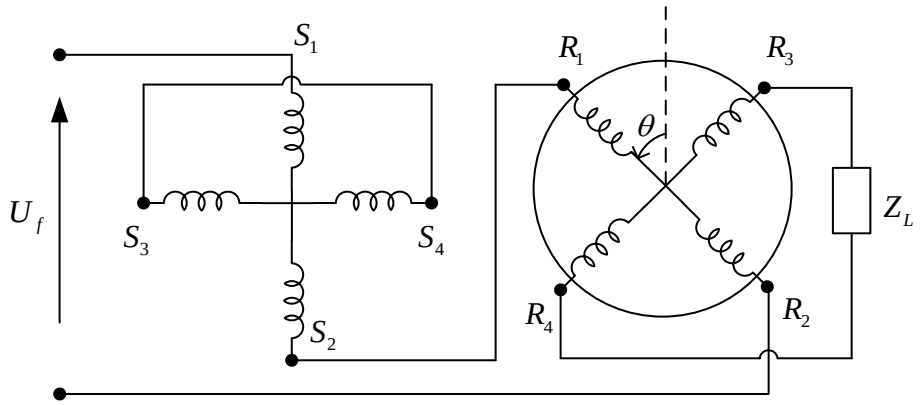

Figure 1.11. Linear resolver schematic

The winding arrangement of a linear resolver is a little different from that of a normal position sensing resolver. The two output windings, (i.e., the sine and cosine windings) are on the rotor and the input windings are on the stator. The stator has an additional compensation winding S_3-S_4. The cosine output winding R_1-R_2 is connected to the input winding S_1-S_2. Then the resolver output voltage which is a linear function of the shaft angle in a specific region can be obtained from the terminals of the sine output winding R_3-R_4. This winding arrangement requires slip rings and brushes for inter-connections. The simplified transfer function of a linear resolver can be expressed as

$$U_L = \frac{K_u \sin\theta}{1 + K_u \cos\theta} U_f \ , \tag{1.10}$$

where K_u is the transformation ratio, U_f the terminal voltage at S_1-R_2, and U_L the terminal voltage at R_3-R_4.

On the other hand, a normal resolver without connecting the cosine output winding to the input winding will generate

$$U_L = K_u U_{S1-S2} \sin(\theta) \ . \tag{1.11}$$

In order to obtain a linear transfer function characteristics, K_u should be in the range of 0.54 ~ 0.57. The curve of the transfer function with K_u = 0.55 is shown in Figure 1.12. The optimal linearity can be achieved in the region where θ = ±60 degrees. As the rotor windings have to be connected with an external circuit, and the linear range is limited in ±60 degrees, it is clear that the applications for this kind of linear resolvers are very limited. It is expected that a linear resolver is brushless, and can operate in 360 degrees range.

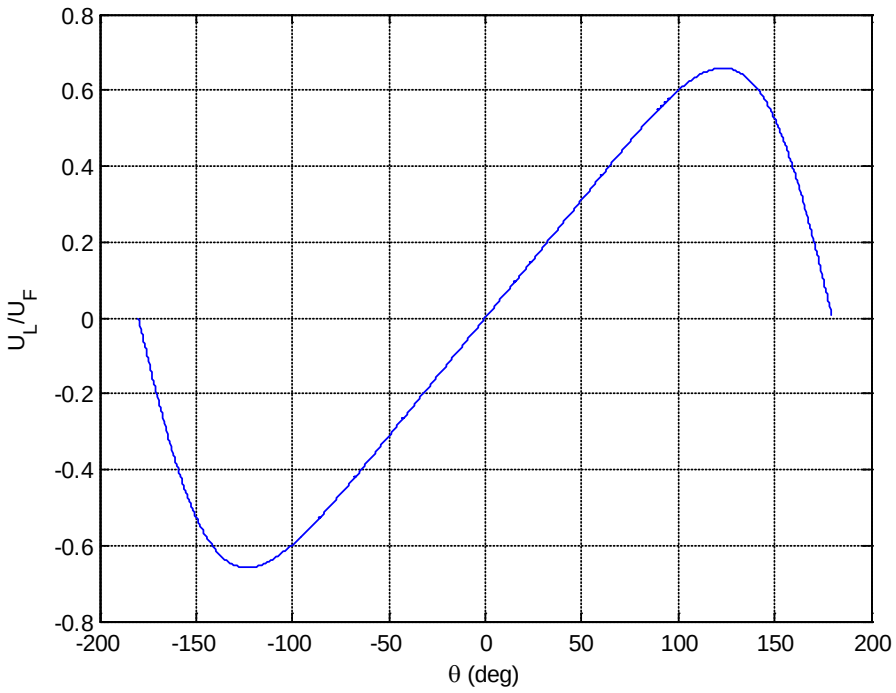

Figure 1.12. Transfer function of linear resolver

1.5 Thesis structure

Chapter 2 presents a review of significant and related research works on resolvers. Application of a resolver as an angular position sensor for the control purpose requires not only the resolver itself but also an electronic interface to decode the position signal to digital format. Thus the review covers those two areas of resolvers.

Chapter 3 describes the dynamic equations of a resolver to reflect the non-ideal characteristics of resolver signals. This is followed by analysis of systematic resolver errors.

Chapter 4 proposes a new demodulation technique to be used in resolver to digital conversion scheme. The technique is developed to minimize the noise effect which is unavoidable in practical implementation of the resolver. The mathematical development of the proposed technique is provided and the validity is proved. The effectiveness of the proposed method is verified with simulation and experiments.

Chapter 5 introduces an approach for initial calibration of a resolver considering the common resolver errors. In order to compensate the resolver errors in real time, an error compensation method based on a complex Fourier series model of the errors is also presented. The compensation method is validated with simulation works.

Chapter 6 explores a synthesis of a new axial type printed circuit linear resolver. The objective is to simplify the conventional brushless resolver structure without losing accuracy. The new electromagnetic structure adapts a slot-less configuration and a carefully devised winding arrangement to eliminate the error sources in conventional resolvers. Experiments are carried out to evaluate the performance of the prototypes built with the new structure.

Chapter 7 discusses the future work and conclusions from the findings of the research works presented in the previous chapters.

2 Literature review

2.1 Introduction

In order to use a resolver as a rotary angular sensor, we need two physical units: one is the resolver itself and the other is an analog to digital interface, so called RDC, which decodes the resolver outputs to obtain the position angle. Based on these two functional units, research works related to the resolver can be categorized into two main groups accordingly.

The first group focuses on the resolver unit. Their research activities cover the areas of design improvement to achieve better accuracy, development of new designs and design guidelines, development of mathematical models to investigate resolver characteristics, and evaluation of resolver performance with computer aided analysis tools like finite element analysis (FEA) under various non-ideal operating conditions. Their objectives are to overcome the shortages in the existing design and to create new designs with low cost without sacrificing the accuracy.

The second group focuses on RDCs. Compared to the first group this group generates a considerable number of reports. Their research works involve development of new algorithms, application of new electronic components and implementation of new converters. They generally aim to achieve the converters having higher accuracy, lower cost and smaller size.

2.2 Design and development of resolvers

Most of the reports related to design and development of resolvers are concerned with the variable reluctance type. Hanselman et al. (1989) provided design guidelines for a variable reluctance resolver structure which can be integrated into brushless motors. In the guidelines, the effects of design parameters and construction

techniques on position accuracy are discussed and the difficulty in achieving high position accuracy is assessed [13].

Sun et al. (2004) proposed a new variable reluctance (VR) resolver with a simplified structure for integration with motor systems. In early construction of VR resolvers, a reasonable tooth number must be maintained on both stator main-pole and rotor to obtain certain precision. This imposes a constraint on reducing the size of the resolver. The proposed VR resolver directly utilized the salient pole effects of the rotor and a simple winding arrangement on the stator. From the test results of resolver samples, it is observed that the precision obtained meets the requirement for commutation of brushless motors in most cases [12]. The continued work of the authors is found in [14-15]. The study in [14] presented the adjustment of three design parameters in VR resolver to improve the accuracy. To minimize the harmonics and null-voltages, it is suggested to increase the number of stator poles, shape the stator tooth into a salient one and arrange the winding in a sinusoidal distribution. Regarding the shaping of salient rotor poles, a new design approach based on an inverse electromagnetic field problem was introduced in [15]. In this work, samples are built using the new design and tests are carried out to examine the achievable accuracy. It is found that the accuracy obtained is low compared to the brushless resolver but it is good enough for the commutation purpose. The study pointed out that the sources of the position errors are from odd-time harmonics and null-voltages in the resolver outputs, which are inherent in reluctance resolvers.

Greg Leibovich and Sara Senanian (2012) introduced a novel structure of VR resolver with couple-pole configuration. This structure is especially designed for the type of single speed resolvers. The rotor structure consists of a skewed magnetic ring which is sandwiched between the two non-magnetic members forming a complete cylindrical ring. The structure results in a uniform air-gap between the stator and the rotor. The variation in reluctance is obtained by change in magnetic flux coupling path between the rotor and stator due to the skewed magnetic ring. The accuracy

achieved with this new structure is reported to be 15 arc-minutes [16]. The report focused on introduction of a new structure, manufacturing process and experimental results from the prototypes and had not presented the design procedures.

The VR resolver with salient rotor structure creates design challenges when an attempt is made to reduce the diameter and the height. When the stator diameter is less than 30mm, it is difficult to realize the winding to meet the required accuracy. To overcome this, Liu et al. (2013) built a novel VR resolver with asymmetric teeth on the stator, which has a minimal number of active teeth and a simplest structure [17]. Because of the asymmetric magnetic circuit, the structure produces null voltages causing error in position information. To eliminate this error, compensating coils are added in series with asymmetric teeth. Experimental results show that the novel resolver has an equivalent precision of ±30 arc-minutes compared to the same type of conventional VR resolvers [17]. But the new structure requires simple manufacturing process and thus has the advantages of being cost-effective and reliable.

The same structure with detailed design procedures can be found in [18-19]. In these studies, 3D finite element method (FEM) in time stepping analysis is used to analyse the induced emfs in resolver output windings. The analysis revealed that there is a discontinuity around the zero crossings of both sine and cosine outputs. From the experimental results of the prototype with the optimized design, the resolver was able to limit the zero error to 8 arc-minutes when the eccentricity is 0.03mm [19].

Davood Pazouk et al. (2013) presented the synchros using a couple-pole configuration with E-cores stator laminations for the low cost of . In the development, initial design and analysis is performed using 2D FEM. Stator winding turns are determined based on an harmonic elimination approach to have a sinusoidal magneto motive force. The design is realized in two prototypes and the experiments verify its validity [20].

2.3 Modelling and performance analysis of resolvers

When the characteristics of a brushless resolver are studied, the common approach does not take into account of the rotary transformer which supplies power to the resolver. This results in an incomplete model and the predicted performance without the parameters from rotary transformer may not be reliable. This issue is addressed by Jiuqing et al. (2001). In their work, the rotary transformer is represented by a transfer function using a general transformer model and the sensing transformer is represented by its dynamic equations. The relationship between the two members is later set up in the analysis. The study highlighted that the resistance of the rotary transformer should be minimized to obtain accurate shaft angle measurement [21]. Their findings in fact should be complemented with the ratio of rotor frequency to excitation frequency. If this ratio is small enough, the resistance effect can be negligible.

In order to estimate the parameters of a brushless resolver without the first rotary transformer, Arab-Khaburi et al. (2007) developed a mathematical model based on the d-q axis theory. The development adapts the parameters identification method applied for induction motors. Electrical and mechanical parameters required for the model is obtained using DC charge excitation, and weight, pulley and belt method, respectively. The developed model is verified by experiments. The experimental results prove that this model can be used to study the dynamic and steady state behaviour of a brushless resolver [22]. The extension of this study taking into account of the eccentricity effect, which could be resulted from imperfect bearing or installation, is presented in [23]. The eccentricity effect is included in the model via different parametric inductances on d-q axis and stator currents. The model is validated by experiments.

In most of the brushless and reluctance resolvers, the electromagnetic field coupling is in radial direction. A novel structure of a brushless resolver with an axial field orientation is presented by Tootoonchian et al. (2012). The new structure is introduced to overcome the shortcoming generated by static eccentricity problem in brushless resolvers for high precision servomechanism. The excitation rotary transformer in the new structure becomes a flat plane type, similar to a pot-core transformer. The sensing member with axially distributed slots and windings enclose the excitation transformer radially. In essence, the new structure is a radial to axial direct transformation. The optimal shape of rotor of the sensing member is emphasized in the study. Analysis of the new structure is carried out by using d-q model and 3D time stepping finite element method, as well as performing experiments with the prototypes [24]. It is shown that the optimized axial brushless resolver is more tolerant to static eccentricity. In [25], a novel algorithm for suppressing the eccentricity error is proposed. The algorithm is developed by transforming the resolver voltage-current equations into a set of linear system equations and applying a state feedback control to eliminate the error.

Figueiredo (2011) developed a new mathematical model for pancake type brushless resolvers. The modelling takes the two-step approach. In the first step, a nominal model based on two traditional transformers connected in series is developed. The parameters needed for this model can be evaluated experimentally. This model is used to compute the resolver nominal design values. In the second step, a linearized differential model is built up to investigate the effects of design parameters. The objective of the model is to allow the manufacturers to manipulate the winding related parameters to achieve the desired performance [3].

Another study on brushless resolvers is reported by Michalski et al. (2007). A model of the magnetic circuit for high-resolution, multi-pole, two-speed brushless resolvers is introduced in this study. The research aims to provide a cost-effective

solution for modelling resolvers manufactured by a single punch die. Based on the circuit model, samples are built and tests are performed. It is found that the measurement results are different from the theoretical calculations. The investigations on the source of errors reveal that the error is due to the imperfect manufacturing [26].

2.4 Resolver to digital conversion

Majority of research on resolver focuses on conversion of resolver outputs to digital position format. Improving the accuracy, reducing the size and the cost are the common objectives of the research. The conversion can be generally grouped into two methods: the hardware-based and the software-based. Most of the hardware-based solutions aim to investigate the accurate and cost effective methods for open loop angle computation.

2.4.1 Hardware-based conversion

The direct approach to compute the position angle is taking the inverse tangent of the ratio of the two demodulated signals. This approach uses both signals at one time. Kaewpoonsuk et al. (2006) introduced an alternative approach of taking inverse sine of the demodulated sine output and reconstructing it to achieve the final linear output. They proposed a hardware-based method to estimate the position angle without microprocessor or DSP. To implement the method, a converter is built with four functional units: demodulation circuit, OTA-based inverse since function circuit (sine-to-triangular wave converter), triangular-to-sawtooth converter and control logic circuit. It is demonstrated that the converter can linearly produce the position signal in full range of 360° [26]. The authors' related works are found in [27-28]. They used opamps and analog switches to construct the triangular-to-sawtooth converter in [27]. However, in [28], a unity gain amplifier is used for the same conversion.

A similar approach without using OTA is proposed by Ben-Brahim et al.(2009). The authors presented a novel scheme to determine the angle from the demodulated resolver signals. The scheme is based on a comparison between the excitation signal and the resolver output signals. The realization of the converter requires low-cost analog and digital electronics without using processors and LUTs. It is a pure hardware solution. The converter provides the output voltage linearly proportional to the shaft angle. A separate signal generator is required to generate the excitation signal and the two other signals, which are synchronized to the excitation signal. The feasibility of the scheme is demonstrated by developing the converter circuits followed by the experiments [29].

Kaewpoonsuk et al. (2010) presented a new demodulation method based on sinusoidal-amplitude detector. The method is realized by electronic components such as rectifiers, amplifiers, sinusoidal-amplitude detectors and control switches. The operation concept is very similar to an envelope detector which rectifies the input signal and holds the peak values. The rectified envelope is corrected to the proper polarity using the excitation signal. It assumed the ideal resolver signals and the study did not include angle computation [30].

To avoid the nonlinear characteristics of the sinusoidal phase comparator which is commonly used in traditional RDCs, Yim et al. (1992) proposed a new RDC structure. The proposed design uses the product detection method to demodulate the resolver output signals. Demodulation is done outside the loop in conjunction with a bang-bang type phase comparator. Since the proposed phase comparator gives only two states, VCO can be implemented digitally resulting a good performance in linearity. Therefore poor tracking performance in the case of a large initial tracking error is avoided. To compensate the time lag due to low pass filters, a time lag compensation circuit is added. The proposed converter has the advantage of suppressing the noise significantly. The converter is built around mixed analogue and

digital circuits. The performance of the converter depends on the components properties such as offsets and drifts of op amps and multipliers [31].

In general, the hardware based techniques require mixed analog and digital components. The commonly found analog components in implementing the techniques such as analog amplitude demodulators and analog multipliers are generally affected by non-ideal behaviours like offset and nonlinearity. The error compensation schemes to improve the accuracy and flexibility to accommodate the design changes are difficult to achieve with hardware techniques. Besides the hardware components add the weight and take the space. This can be constraints to some applications. So more and more research works are now concentrating on the software approach to realize the conversion.

2.4.2 Software-based conversion

In order to overcome the limitations of the conventional RDC chips such as components tolerance, parameter variations, and inflexible dynamic and static performance, A. O. Di Tommaso and R. Miceli (2003) proposed an alternative solution of the new high accuracy software based RDC. The demodulation method used in conversion process is similar to the synchronous peak detection method but it is enhanced with FIR filter and decimation. This demodulation approach improves the position signal amplitude resolution by reducing the bandwidth of the signal fed to the tracking loop while suppressing the noise. The implementation requires oversampling of resolver signals. Due to the filter, a delay is introduced. The sampling rate and decimation ratio are deliberately chosen so that the delay results in an integer sample value. This delay is compensated by adding a matched delay to the position estimate in the tracking loop which is constructed with a PI controller and an integrator. Unlike the conventional RDC, the tracking loop contains only low pass quantity and its dynamic and static characteristics can be configured by adjusting the

gains and damping factor. Regarding the quality of the resolver signals, the development of the RDC considered only the noise issue and assumed the signals are ideal [32].

Implementation of RDC using FPGA with VHDL was reported by Ji-Hye Jeon et al. (2007). In contrast to the conventional use of resolver, the input and outputs are reversed in the study. The operation is equivalent to the receiver synchro. The converter excites the sine and cosine windings on stator according to the desired rotor position. This generates a signal based on the difference between the desired rotor position and the actual rotor position. This signal is used to drive the servo motor to reduce the error. The study investigates the generation of input signals to achieve the perfect quadrature and the stabilization of generated signals [33].

In [34-35], Sarma et al. (2008) introduced a simple and cost-effective RDC using software approach. The carrier signal is generated by a second-order digital filter. This generator outputs a pair of sine and cosine signals: one is used for exciting the resolver and the other is used for synchronous sampling by detecting its zero crossings. Since the trigger signals for sampling are generated from noise-free signal, zero crossing points are not affected by the noise and the demodulating at the peak of the carrier is efficient. The angle computation is carried out by the inverse tangent method. To save the memory, only one octant is used in building the look-up table in conjunction with the octant detection logic for inverse tangent computation. The accuracy of the proposed method relies on the performance of ADC, DAC and, precision and resolution of the inverse tangent table. The method is supported by simulation work and realizing the algorithm on DSP. It should be noted that the development assumes that the resolver signals are ideal. The method has the advantage of having no delay in conversion process. It implies that the dynamics of the servo control will not be affected by using this method. The main drawback of

this method is that the accuracy is sensitive to noise even if the resolver signals are perfect.

Zhu Yi et al. (2010) proposed another conversion method using the software approach. The method provides a higher position resolution without increasing the carrier frequency compared to the synchronous peak detection. When looking up the table for direct inverse tangent computation, tangent and cotangent functions are employed alternately. The computation is based on modulated resolver outputs with discarding the sampled values around the carrier zero crossing by setting a threshold. The demodulation is carried out from the ratio of the squared of one signal to the squared of both signals. The method is suitable for ideal resolver signals. The digital positions achieved are not spaced uniformly [36].

2.4.3 Resolver accuracy improvement and errors compensation

In the above software approach studies, the resolver signals are assumed to be ideal. In [34-35], the proposed methods do not consider the noise effect. The accuracy of those methods depends on the quality of the resolver signals. Any imperfection of the resolver or disturbance in signals will introduce position errors in conversion. Since the control system performance highly depends on the accuracy of the feedback signal, it is desirable to obtain a reasonably accurate position output from the conversion process. This can be achieved by adding the compensation scheme to the conversion method.

Hanselman (1991) investigated the relation between the position angle errors and imperfect resolver signals. The investigation is made for angle estimation in the closed-loop computation. This study finds that the amplitude imbalance error bound for ½ LSB accuracy out of 10 bits resolution is as small as 0.62%. And the allowable quadrature error for the same configuration is only 3.1E-3 radians [37-39]. Various

schemes are reported for compensating the position errors due to imperfect resolver signals [40-52] .

When the conversion is implemented using DSP, noise is a limiting factor to obtain the target accuracy. In [40], B. A. Murray and W. D. Li (1993) realized an ATO using DSP and they investigated the quantization effects, the system dynamic performance and the rejection of noise. It is observed that quantization noise introduce errors at low speed operation. To overcome this problem, the phase error which is the difference between the estimated and actual angle is calculated using two multiplying DACs. All the findings are obtained from the simulation results.

In order to identify and cancel out the position errors induced by DC offset, imbalance amplitude and quadrature, A. Bunte and S. Beineke (2004) proposed an error compensation method based on complex Fourier series expression. The error contributions to the resolver signals are represented by the Fourier coefficients in this method. These coefficients are obtained by evaluating the cross-correlation of the line signals over certain fixed number of periods of the line signals. As a result, this method is not valid for online adaptation for fast point-to-point positioning with small distances for resolver line signals with less than one period [41].

V. D. Aksenenko and S. I. Matveyev (2005) presented a self-calibration technique of VR resolvers in a redundant system in [42]. The study proposes two approaches for self-calibration: the first approach uses the iterative method to update the error function which is constructed with few harmonics contents and the second approach employs the error model which is the function of measured angle considering wide range of harmonics band. The results from simulation and experiment prove that the significant improvement in accuracy is obtained with the proposed calibration methods.

If the direct inverse tangent approach is used, the converter can only give the position information. The rotor speed is often calculated by a derivative operation of the position estimate. This results in unfiltered speed which is undesirable for the applications that use the speed feedback information. In [43], A. Bellini and S. Bifaretti (2006) proposed a filter based on PLL to obtain the speed signal. This filter structure is similar to the angle tracking observer but with a steady-state linear Kalman filter in place of a normal loop filter. It is reported that using the Kalman filter avoids a significant lag on the speed estimation during starting and stopping transients, which generally occur at particularly constant acceleration. The method is demonstrated using a 16-bit fixed point DSP for an industrial synchronous motor drive.

Hoseinnezhad et al. (2007) proposed an approach for real-time tracking of resolver parameters is proposed specially for actuator-control applications with varying speed and long resting periods. If a resolver is not perfect and its demodulated outputs are plotted against each other, we obtain a Lissajous or elliptic figure. Thus the ellipse represents the characteristic of imperfection. This paper investigates the formulation of algebraic relationship between the parameters of the characteristic ellipse of the resolver and resolver parameters. The modified recursive least square estimator is used to fit the measured data to the ellipse. After the parameters are estimated, the calibration of resolver can be carried out to maintain the position accuracy. The method however has a high cost for the online calibration [44].

Another calibration technique to compensate the imperfect resolver signals was reported by Kaul et al. (2008). The method is developed using the error profiles of several integrated units of resolver and converter. The error profiles are obtained from calibrating the integrated units on a high precision rotary table. To ensure the accuracy of error profiles, repeated calibrations are carried out over a period few months. Harmonic analysis is performed on those error profiles to build up the

Fourier series representation for each unit. Error compensation method involves subtracting the predicted error from the converter output. It is reported that this compensation method improves 10 times better than the quoted accuracy [45].

S. Sarma and A. Venkateswaralu (2009) presented a novel scheme for resolver signals to digital position conversion that includes fault detection and identification of the sensor in [46]. This is in fact the extension work of [35]. The scheme mitigates the errors in position and speed estimate due to common resolver imperfections and provides fault indicators such as good resolver signal, degradation of signal, and loss of signal for fault tolerant operation and diagnosis of malfunctions in the sensor. Demodulation scheme is unchanged but the angle computation is performed using an adaptive PLL that accurately estimates the angular position and speed for a wide speed range. Regarding with resolver errors, amplitude imbalance, quadrature error and inductance harmonics are considered in the implementation. An adaptive quadrature phase detector is employed to estimate the phase shift due to imperfect quadrature. The position estimation uses only one resolver output with the adaptive PLL that comprises a modified phase detector. The method is validated with a resolver simulator and an Analog Devices DSP board. The reference phase shift and noise are not considered in this work.

Hwang et al. (2011) investigated an application specific error compensation technique in [47]. The application uses a resolver in the vector control of a permanent magnet synchronous motor. Due to imperfect gain and phase of a resolver, errors are introduced in the converter outputs. This study analyzed the effects of the position errors on the basis of the synchronous dq-axis current equations, including the position error. The position error is compensated by suppressing the ripple components of the d-axis current using the proportional integral (PI) controller of the proposed compensator. The integral operation that is used to estimate position error parameters takes into account of the bandwidth effect of the closed current control

loop. This is an application specific resolver errors compensation scheme and the effectiveness of the proposed method was supported with experimental results.

In [48-49], Bergas-Jané et al. (2012) presented a method to compensate the two systematic errors, gain and phase, based on a double synchronous reference frame-based phase-locked loop (DSRF-PLL). In addition, their works use the oversampling with decimation to increase the achievable position angle resolution. This method implements the software approach to replace the phase detector and loop filter in conventional RDCs. Carrier signal is generated from a pulse width modulation (PWM) followed by an analog multiplier. Demodulation is carried out as in the product detection method but with the reference phase shift compensated carrier signal. Instead of a normal low pass filter, a combination of low pass filter and decimation is carried out to complete the demodulation. The angle computation in this method is originated from synchronous frame phase-locked loop (SRF-PLL) which is essentially the same as the angle tracking observer. Without compensation, gain and phase errors degrade accuracy on computation of position and speed outputs. To eliminate the influence of these errors, DSRF-PLL and decoupling units are employed. DSRF-PLL is similar to SRF-PLL but it is composed of two rotating reference axes; one with the positive frequency and the other with the negative frequency. Thus, the demodulated outputs are decomposed into positive and negative sequence components by DSRF-PLL giving two pairs of signals. These signals are delivered to the respective positive and negative decoupling units where the errors are suppressed. The positive sequence quadrature component is finally fed into the usual phase tracking loop. The method is implemented with 32-bit DSP integrated with 12-bit ADCs. It is reported that the resolution of the calculated resolver angle is improved to 13 ~ 14 bit.

Another study of using DSRF-PLL to implement the converter was conducted by Yongxiang et al. (2012) in [51]. In this work, synchronous peak detection method is

used for demodulation. The rest parts of the RDC are unaltered. It gives the more detailed description on application of DSRF-PLL in RDC. The authors pointed out that when the quadrature error exists, there is a constant error in the estimated position and speed.

Khaburi (2012) presented a new conversion algorithm in [52]. To reduce the total cost, the resolver is excited by a square wave. The synchronous peak detection method is used to demodulate the resolver output signals. The initial estimation of the rotor angle is estimated from the direct inverse tangent computation. The angle is computed by a modified ATO. The modification is performed on the phase error calculation. For low speed operations, the small angle assumption on the difference of sine is acceptable. For high speed operations, the assumption fails and there is a constant error which depends on the rotor speed. To minimize this error, a proportional control is applied to the estimated angle. This control adjusts the error till it reaches in the acceptable range.

The above studies focus on the accuracy improvement in resolver outputs to digital position conversion. It can be concluded that error compensation is essential to improve or maintain the achievable accuracy. With the proper error compensation, even the accuracy of low cost resolvers can be improved reasonably. In software-based techniques, the accuracy depends on several factors such as ADC resolution, quantization, noise rejection, demodulation technique, DSP performance, excitation signal generation and error compensation. Also the accuracy requirement varies with the type of applications. Advances in DSP performance and continually decreasing DSP chip prices encourage more research on optimal algorithm to improve the accuracy of the position conversion. Besides, research on the improvements in the design of resolver sensor is also needed so that low cost resolvers could be manufactured.

2.5 Objectives

As seen in the literature survey, the research works can be categorized into two: the resolver itself and its converter. In general, the objectives of these works were to improve the accuracy of resolver and to reduce its size and cost. However, these two categories were separately studied. The results from one category had not been applied or considered in the study of the other. Since resolver and its converter operate as a system, it requires a consideration of both resolver and converter at the same time to have a complete study.

The research work in this thesis attempts to fulfil this requirement by taking the analysis and synthesis approach. In doing so, the main objectives of the thesis are:

- to have a better understanding of the factors that can affect the accuracy of a resolver system,
- to investigate means and ways to improve the accuracy of a resolver system, and
- to explore a new resolver structure that will mitigate the effect of error sources in a resolver system as well as reduce the cost.

3 Analysis of a brushless resolver

3.1 Introduction

A brief introduction of resolvers is presented in Chapter 1. Under the assumption of ideal conditions, the operation of a resolver is similar to a telecommunication system which employs amplitude modulation for transmission of signal. The rotor position and the excitation signal of resolver resemble the message signal and the carrier signal, respectively, of the amplitude modulated signal in telecommunication. However, this analogy cannot fully characterize the operation of a real resolver. In order to investigate the characteristics of a resolver, there is a need to comprehend the development of complete dynamic resolver equations based on its electromagnetic structure and principles of operation. In addition, it is necessary to identify the parameters that affect the accuracy. This chapter focuses on the analysis of a brushless resolver and the systematic errors likely to be found in it.

3.2 Voltage equations

The brushless resolver consists of an excitation rotary transformer and a sensing transformer, or the resolver sensor. In a brushless resolver, the rotary transformer operates as a linear device since the magnetic material of the resolver is usually unsaturated during operation. Therefore, a sinusoidal input with certain frequency to the excitation transformer produces the output with identical frequency. No additional harmonics of emf in the output winding is induced. However, the amplitude and phase of the output can be different from those of the input as they are dependent on winding parameters and electromagnetic structure. The operation of the resolver sensor is thus not affected by the excitation transformer and the voltage equations for the resolver can be derived separately.

Consider that the rotor winding of the resolver sensor is excited by a sinusoidal voltage source with amplitude, V_e and frequency, ω_e,

$$v_e(t) = V_e \cos(\omega_e t) \tag{3.1}$$

Since the applied voltage is sinusoidal, the flux produced should also be the sinusoidal. Assuming linear relationship between flux and excitation current ($\phi \propto i$),

$$i_e(t) = I_e \sin(\omega_e t) \tag{3.2}$$

where I_e is the amplitude of the excitation current.

Taking the resistance of stator windings into account, the induced output voltages can be described as:

$$\begin{aligned} v_s &= R_s i_s + L_s \frac{di_s}{dt} + \frac{d}{dt}\left\{M_{se}(\theta) i_e\right\} \\ &= R_s i_s + L_s \frac{di_s}{dt} + i_e \frac{d}{dt} M_{se}(\theta) + M_{se}(\theta) \frac{d}{dt} i_e \\ v_c &= R_c i_c + L_c \frac{di_c}{dt} + \frac{d}{dt}\left\{M_{ce}(\theta) i_e\right\} \\ &= R_c i_c + L_c \frac{di_c}{dt} + i_e \frac{d}{dt} M_{ce}(\theta) + M_{ce}(\theta) \frac{d}{dt} i_e \end{aligned} \tag{3.3}$$

where R_s, R_c; L_s, L_c; i_s, i_c; v_s, and v_c are the resistances, self-inductance, currents and voltages of the stator sine and cosine windings; M_{se} the mutual inductance between the stator sine winding and the rotor winding; M_{ce} the mutual inductance between the stator cosine winding and the rotor winding and θ the rotor position angle, respectively.

Since the stator windings are connected to the high impedance RDC interface, there will be negligible current in the stator windings and the current derivatives can also be ignored. This leads to the following equation set:

$$\begin{aligned} v_s &= i_e \frac{d}{dt} M_{se}(\theta) + M_{se}(\theta) \frac{d}{dt} i_e \\ v_c &= i_e \frac{d}{dt} M_{ce}(\theta) + M_{ce}(\theta) \frac{d}{dt} i_e \end{aligned} . \tag{3.4}$$

Assuming that there is no harmonics and DC offset in the mutual inductances, the sine and cosine windings are 90° displaced exactly, and the peak amplitudes of the sine and cosine windings are identical, one can express the mutual inductance as the following:

$$\begin{aligned} M_{se}(\theta) &= M \sin(\theta) \\ M_{ce}(\theta) &= M \cos(\theta) \end{aligned} . \tag{3.5}$$

With the rotor speed of ω_m, the voltage equations become

$$\begin{cases} v_s = I_e \sin(\omega_e t)\omega_m M \cos(\theta) + M \sin(\theta)\omega_e I_e \cos(\omega_e t) \\ v_c = -I_e \sin(\omega_e t)\omega_m M \sin(\theta) + M \cos(\theta)\omega_e I_e \cos(\omega_e t) \end{cases} . \tag{3.6}$$

In terms of the rotor winding resistance (R_e), and the inductance, (L_e), the exciting current may be expressed as:

$$i_e = \frac{V_e}{\sqrt{R_e^2 + \omega_e^2 L_e^2}} \sin(\omega_e t + \varphi) , \tag{3.7}$$

where

$$\varphi = -\tan^{-1} \frac{\omega_e L_e}{R_e} . \tag{3.8}$$

Using (3.2), (3.6) and (3.7), one obtains the resolver sensor output equations as:

$$\begin{cases} v_s = V_e \dfrac{M\omega_m}{\sqrt{R_e^2+\omega_e^2 L_e^2}}\cos(\theta)\sin(\omega_e t+\varphi) + V_e \dfrac{M\omega_e}{\sqrt{R_e^2+\omega_e^2 L_e^2}}\sin(\theta)\cos(\omega_e t+\varphi) \\ v_c = -V_e \dfrac{M\omega_m}{\sqrt{R_e^2+\omega_e^2 L_e^2}}\sin(\theta)\sin(\omega_e t+\varphi) + V_e \dfrac{M\omega_e}{\sqrt{R_e^2+\omega_e^2 L_e^2}}\cos(\theta)\cos(\omega_e t+\varphi) \end{cases}$$
. (3.9)

The resolver sensor output voltage equations described by (3.9) reveals the relationship between the rotor and stator parameters in a more complete sense. If the resistance in the rotor winding is considered to be negligible and the coupling coefficient of the rotor and stator winding is defined by:

$$k = \frac{M}{\sqrt{L_e L_s}}, \tag{3.10}$$

the simplified expression of (3.9) can be shown as

$$\begin{cases} v_s = k\sqrt{\dfrac{L_s}{L_e}}\dfrac{\omega_m}{\omega_e}V_e\cos(\theta)\sin(\omega_e t) + k\sqrt{\dfrac{L_s}{L_e}}V_e\sin(\theta)\cos(\omega_e t) \\ v_c = -k\sqrt{\dfrac{L_s}{L_e}}\dfrac{\omega_m}{\omega_e}V\sin(\theta)\sin(\omega_e t) + k\sqrt{\dfrac{L_s}{L_e}}V_e\cos(\theta)\cos(\omega_e t) \end{cases}, \tag{3.11}$$

where L_s is the inductance of each stator winding which is assumed to be the same. It is observed that each voltage equation has two terms: (1) the first term represents the speed voltage, and (2) the second term represents the transformer voltage. In general rotating electrical machines, the speed voltage is used to convert electrical power to mechanical power by producing torque. But for the resolver sensor, the speed voltage is a disturbance signal to the operation. The demodulation scheme in RDCs must take into account of this term and filter it out. On the other hand, the first term can be safely ignored if the ratio of the rotor frequency to the excitation frequency is significantly small. Ignoring the first term in (3.11), we can obtain the simplified ideal resolver output equations

$$\begin{cases} v_s = KV_e \sin(\theta)\cos(\omega_e t) \\ v_c = KV_e \cos(\theta)\cos(\omega_e t) \end{cases}, \tag{3.12}$$

where

$$K = k\sqrt{\frac{L_s}{L_e}} \tag{3.13}$$

is defined as the transformation ratio or the gain of the resolver.

3.3 Simulation of a brushless resolver

Before describing the systematic errors common to resolvers, a simulation case study of a traditional resolver is presented. We used an industrial brushless resolver to illustrate the electromagnetic field distribution and induction phenomenon. The simulation is focused to the position sensing and excitation transformer for the resolver is omitted. In this case, excitation signal is directly applied to the rotor winding in the electromagnetic model.

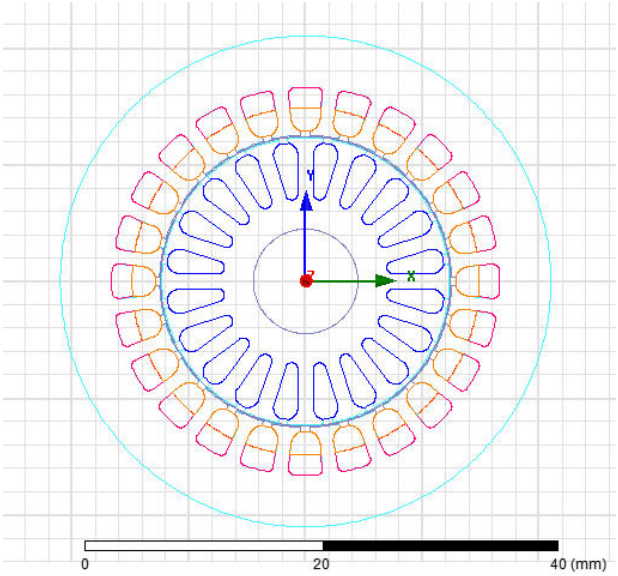

Figure 3.1. Model of the brushless resolver

The electromagnetic model of the resolver is shown in Figure 3.1. The rotor has 20 slots and the stator has 24 slots. Both windings in the stator and rotor are distributed to produce a sinusoidal magneto-motive force distribution, i.e. each slot has different number of turns. The winding distribution is provided in Figure B. 1. The excitation voltage is 115V and its frequency 400Hz. The details of the resolver specifications are provided in Appendix B. ANSYS, MAXWELL is used to perform the finite element analysis. A flux linkage snapshot of the resolver is shown in Figure 3.2. It can be seen that the resolver flux linkages form a 2-pole machine and flux are distributed evenly to left and right side of the machine.

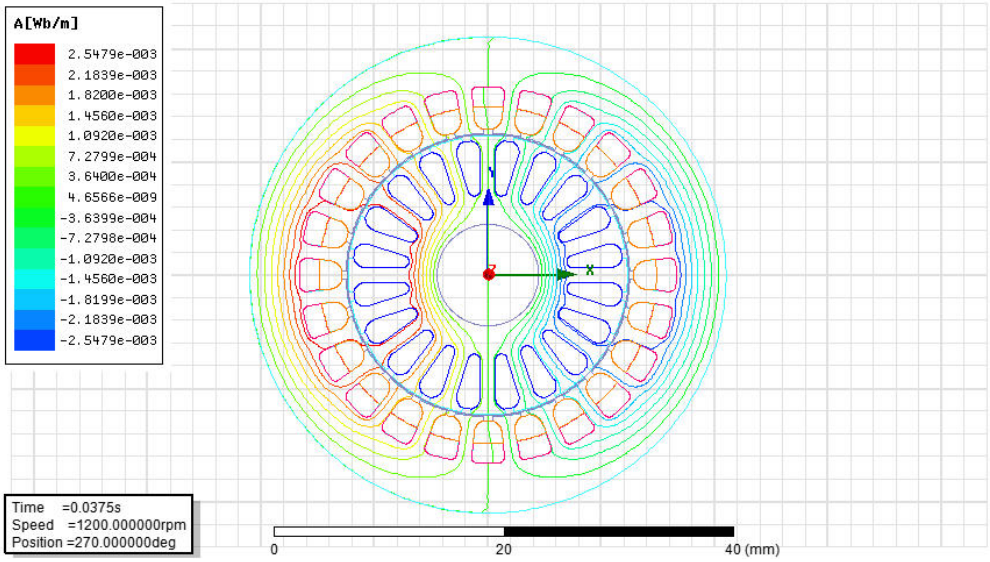

Figure 3.2. Flux linkage in the resolver

To observe the induced emfs, the simulation is done in transient analysis mode. When the resolver rotor speed is set to 1200 rpm, the induced emfs are obtained as shown in Figure 3.3. As described in the previous section, the outputs of the resolver are in fact the amplitude modulated signals. Therefore, the controller in a motor drive cannot use these outputs directly. Recovering the envelope and estimating the position angle from the recovered envelops are required. But in some applications for

the commutation purpose, the retrieved envelopes can be directly used by the controller.

For the demodulation, as the excitation frequency is only 400 Hz, and the rotor speed is 1200 rpm (20 Hz), there are only 20 peaks in one mechanical revolution. This implies that the product detection scheme is a right choice as it uses all the sampling data. The demodulated outputs using the product detection method is shown in Figure 3.4. The profiles of the demodulated outputs are in good sinusoidal shape but the harmonic contents can only be clearly seen in the frequency domain. Therefore, the spectrum analysis is carried out to observe the harmonic contents. It can be seen that the harmonic having about 0.26% of the fundamental amplitude is found at the order of 41. This is related to the slot harmonics due to the number of slots is equal to 40. It proves that harmonics are unavoidable but with the proper combination of stator and rotor slots, the harmonics can be minimized and the resolver outputs can be close to ideal signals. A study related to winding structure and effect of harmonics in spindle motors is carried out and reported in [56].

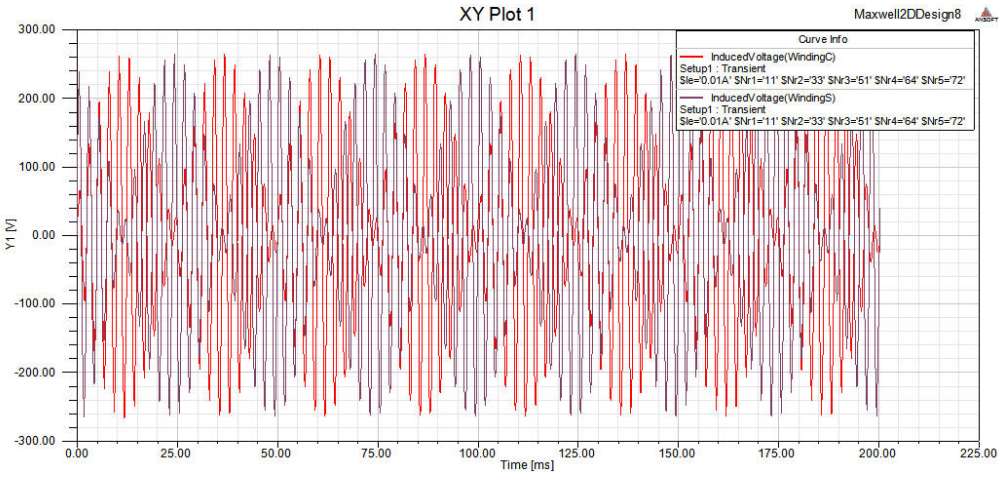

Figure 3.3. Induced emfs in stator windings

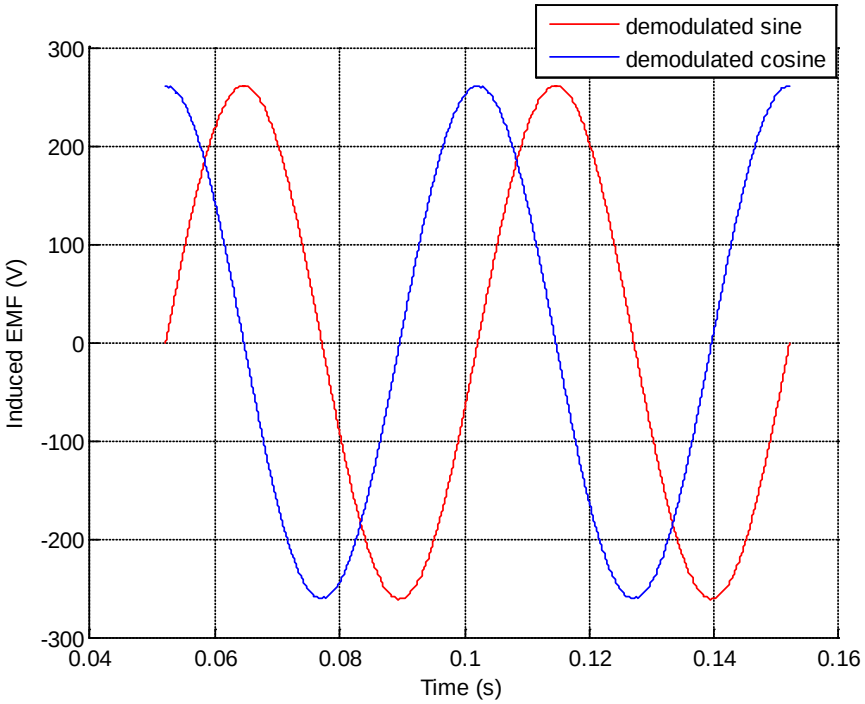

Figure 3.4. Demodulated resolver outputs

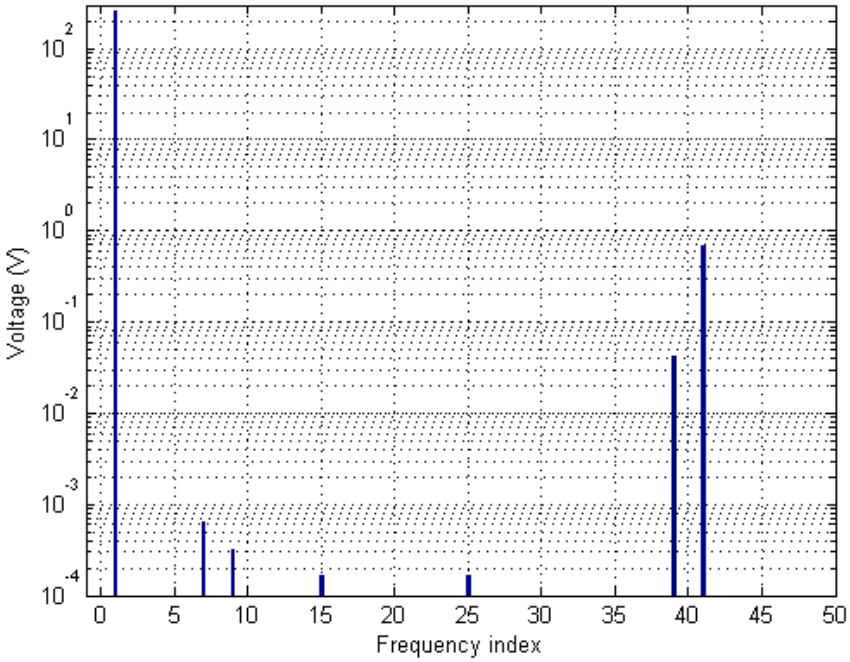

Figure 3.5. Spectrum of demodulated sine output

3.4 Resolver errors

Several assumptions are made to reach the ideal resolver equations in the deduction of resolver output voltage equations. In practice, these assumptions are valid only to a certain extent depending on the precision of manufacturing techniques used. Therefore, resolver errors are unavoidable if the manufacturing is imperfect. In addition, the principle of resolver operation itself introduces an error such as the speed voltage term in (3.11). Even if the resolvers are perfectly constructed, the resolver parameters still vary due to working conditions, and thus there are chances for a measurement system to experience errors in operation. The errors that introduce consistent and repeatable bias to a measurement system are known as systematic errors. In order to improve the accuracy of a resolver system, these systematic errors need to be identified and controlled in the design process as well as in the resolver to digital conversion scheme. The systematic errors commonly found in a resolver are (1) amplitude imbalance, (2) quadrature error, (3) inductive harmonics, (4) reference phase shift, and (5) excitation signal distortion [38]. The description of each error is explained below, considering one error at a time and neglecting the speed voltage term. And the excitation signal distortion is omitted as it is related to the RDC implementation and it can be controlled by proper signal generation technique.

Amplitude imbalance: This imperfection refers to the different amplitudes of the two output signals of the resolver. The unequal winding inductance ratios can result in different electromagnetic coupling between the rotor and stator windings which in turn cause the amplitude imbalance. In presence of this amplitude imbalance, the resolver outputs given by (3.12) is changed into

$$\begin{cases} v_s = KV_e \sin(\theta)\cos(\omega_e t) \\ v_c = (1+\alpha)KV_e \cos(\theta)\cos(\omega_e t) \end{cases}, \tag{3.14}$$

where α is the amount of amplitude imbalance. This imperfection is also referred to as gain error.

Quadrature error: This error arises when two magnetic axes of the resolver output windings are not exactly 90° apart due to winding and magnetic pole orientation. Imprecise machining and assembly can result in this type of error. The resolver outputs when quadrature error exists can thus be expressed as

$$\begin{cases} v_s = KV_e \sin(\theta)\cos(\omega_e t) \\ v_c = KV_e \cos(\theta+\beta)\sin(\omega_e t) \end{cases}, \tag{3.15}$$

where β is the phase shift that contributes to the quadrature error.

Inductance harmonics: Due to magneto-motive force (MMF) harmonics and slot harmonics, in practice, the mutual inductances expressed by (3.5) may not be in perfect sinusoidal relationship and they can have harmonics. In general, these non-sinusoidal mutual inductances can be described by Fourier series expansion with

$$\begin{cases} M_{se}(\theta) = \sum_{n=1}^{\infty} M_n \sin(n\theta) \\ M_{ce}(\theta) = \sum_{n=1}^{\infty} M_n \cos(n\theta) \end{cases}. \tag{3.16}$$

When this happens, the resolver outputs will be

$$\begin{cases} v_s = V_e \left\{ \sum_{n=1}^{\infty} L_n \sin(n\theta) \right\} \cos(\omega_e t) \\ v_c = V_e \left\{ \sum_{n=1}^{\infty} L_n \cos(n\theta) \right\} \cos(\omega_e t) \end{cases}. \tag{3.17}$$

where $L_n = M_n / L_e$. In the case of a VR resolver, all the windings are on the stator and the excitation winding and output windings are arranged in stacked layers. This

eventually causes the flux linking from the excitation winding to output windings independent of the rotor position, so the mutual inductance will have an additional DC component. On the other hand, the excitation winding is separated from output windings in a brushless resolver, and they are located on the rotor and stator respectively. According to the principle of operation, there is no constant flux linkage between the excitation winding and output windings. Therefore, the mutual inductance can be assumed to have no DC component.

Phase shift: As explained while deducing the resolver voltage equations, there exists a phase shift between the excitation input signal and the resolver output signals due to the voltage drop in rotor winding. Then the resolver output equations will be

$$\begin{cases} v_s = KV_e \sin(\theta)\cos(\omega_e t + \phi) \\ v_c = KV_e \cos(\theta)\cos(\omega_e t + \phi) \end{cases}, \tag{3.18}$$

where ϕ is the phase shift due to resistance effect. This phase shift has the scaling effect on demodulation process in RDC.

Apart from the systematic errors mentioned above, there can be other errors due to imperfect installation such as axial or radial misalignment of the resolver rotor when the resolver is coupled to the shaft of the motor.

3.5 Estimation of position error

Due to resolver imperfections, RDC designed for ideal resolver signals results in position errors. The respective error characteristics for a VR resolver when RDC employs tracking observer technique are reported in [38]. If RDC uses the direct inverse tangent method for a brushless resolver, the similar error characteristics are expected. However this has not been reported in the literature. In order to gain a full understanding of error development and to make a comparison of the results from both methods, the analysis on four systematic errors is performed in this section.

3.5.1 General form of position error

The position error, ε, generated by the inverse tangent method can be given by

$$\varepsilon = \theta - \tan^{-1}\left(\frac{v_{sd}}{v_{cd}}\right), \tag{3.19}$$

where θ is the true angle and v_{sd} and v_{cd} are the demodulated resolver outputs that may contain errors. To ease in computation, tangent operation is applied to both sides of (3.19) yielding

$$\tan(\varepsilon) = \tan\left(\theta - \tan^{-1}\left\{\frac{v_{sd}}{v_{cd}}\right\}\right). \tag{3.20}$$

Assuming the error is small, we use small-angle approximation to the left side of (3.20) and obtain

$$\varepsilon \approx \tan\left(\theta - \tan^{-1}\left\{\frac{v_{sd}}{v_{cd}}\right\}\right). \tag{3.21}$$

Based on (3.21), estimating the position errors is carried out in the following sections.

3.5.2 Imbalance amplitude

Using (3.14) and (3.21), position error incurred by imbalance amplitude in resolver outputs can be expressed by

$$\varepsilon \approx \tan\left(\theta - \tan^{-1}\left\{\frac{\sin(\theta)}{(1+\alpha)\cos(\theta)}\right\}\right). \tag{3.22}$$

With the aid of trigonometric identity,

$$\tan(A-B) = \frac{\tan(A)-\tan(B)}{1-\tan(A)\tan(B)} = \frac{\sin(A)\cos(B)-\cos(A)\sin(B)}{\cos(A)\cos(B)+\sin(A)\sin(B)}, \tag{3.23}$$

(3.22) can be reduced into

$$\varepsilon \approx \frac{\alpha \sin(2\theta)}{2+\alpha\left[1+\cos(2\theta)\right]} \tag{3.24}$$

If α is considered to be small, (3.24) can be further approximated as

$$\varepsilon \approx \frac{\alpha}{2}\sin\left(2\theta\right) \tag{3.25}$$

Thus, with the amplitude imbalance, the maximum possible position error would be about half of the amplitude difference. If the rotor is at a constant speed, the position error will have twice the frequency of the rotor.

3.5.3 Quadrature error

Similarly, the position error introduced by not having exactly 90° phase difference between the resolver outputs can be derived from (3.15) and (3.21) as

$$\varepsilon \approx \tan\left(\theta - \tan^{-1}\left\{\frac{\sin[\theta]}{\cos[\theta+\beta]}\right\}\right). \tag{3.26}$$

Perform the trigonometric expansion to (3.26), and it becomes

$$\varepsilon \approx \frac{\sin(\theta)}{\cos(\theta)+\dfrac{\sin^2(\theta)}{\cos(\beta)\cos(\theta)-\sin(\beta)\sin(\theta)}} - \frac{\cos(\theta)\sin(\theta)}{\left\{\cos(\beta)\cos(\theta)-\sin(\beta)\sin(\theta)\right\}\left\{\cos(\theta)+\dfrac{\sin^2(\theta)}{\cos(\beta)\cos(\theta)-\sin(\beta)\sin(\theta)}\right\}} \tag{3.27}$$

Using the approximation, $\cos(\beta) \simeq 1$ and $\sin(\beta) \simeq \beta,$ for small β, (3.27) can be simplified into

$$\varepsilon \approx \frac{2\beta \sin\left(\theta\right)^2}{-2+\beta\sin(2\theta)} \ . \tag{3.28}$$

If β is considered to be small, (3.28) can be reduced into

$$\varepsilon \approx -\frac{\beta}{2}\left[1-\cos\left(2\theta\right)\right] . \tag{3.29}$$

It is observed that the position error due to the quadrature error is similar to the error due to amplitude imbalance. Both have the same frequency but they are 90° out of phase to each other. The extra term found in quadrature error is the DC offset term that has the amplitude of half of the error.

3.5.4 Inductance harmonics

When resolver inductance in (3.5) contains harmonics, the resolver outputs can be expressed as (3.17). Then the position error will be

$$\varepsilon \approx \tan\left[\theta - \tan^{-1}\left\{\frac{\sum_{n=1}^{\infty} L_n \sin(n\theta)}{\sum_{n=1}^{\infty} L_n \cos(n\theta)}\right\}\right] . \tag{3.30}$$

This equation can be reduced into

$$\varepsilon \approx -\frac{\sum_{n=1}^{\infty} K_n \sin\left[(n-1)\theta\right]}{\sum_{n=1}^{\infty} K_n \cos\left[(n-1)\theta\right]} , \tag{3.31}$$

where $K_n = \frac{M_n}{M_1}$. If K_n (n=1,2,3,...) are considered to be small, (3.31) can be simplified as

$$\varepsilon \approx -\sum_{n=1}^{\infty} K_n \sin\left[(n-1)\theta\right] . \tag{3.32}$$

That is, the magnitude of the position error due to inductance harmonics is related to the sum of the ratios of magnitudes of the harmonics and the fundamental. It is

observed that the resolver behaves as a linear system to the inductance harmonics and thus the error harmonics have the same frequency with different gains.

3.5.5 Phase shift

When there is a phase shift between the resolver excitation signal and output signals, the demodulation carried out with the excitation signal will alter the amplitude of the actual position signal. It can be shown that the amplitude of the demodulated resolver outputs are reduced by a factor, and the amplitude of the factor is proportional to the phase difference. The expression of the demodulated outputs with phase shift can be described as

$$\begin{cases} v_{sd} = KV_e \cos(\phi)\sin(\theta) \\ v_{cd} = KV_e \cos(\phi)\cos(\theta) \end{cases}, \tag{3.33}$$

where ϕ is the phase difference between the excitation signal applied to the resolver unit and the output signals. It can be observed that the amplitudes of the demodulated outputs are reduced by a factor of cosine of the phase difference. For small values of phase difference, this has no impact on the computation of position angle. This also shows that the resolvers are tolerant to multiplicative disturbance effects. However, this advantage depends on the speed ratio of the rotor frequency to the excitation frequency. If there is no phase difference, the demodulation scheme can remove the speed voltages which are in quadrature to the transformer voltages. For example, in the demodulation process using the peak detection scheme, if the resolver output voltages are sampled at the peaks of the excitation signal, the speed voltage components can be safely ignored because they are at their minimum at these instants. In this case the speed ratio factor is insignificant. But when there is a phase difference, the speed voltage is no longer at its minimum at the time of sampling and it is part of the demodulated outputs that could be given by

$$\begin{cases} v_{sd} = KV_e\left[\cos(\phi)\sin(\theta) - \dfrac{\omega_m}{\omega_e}\sin(\phi)\cos(\theta)\right] \\ v_{cd} = KV_e\left[\cos(\phi)\cos(\theta) + \dfrac{\omega_m}{\omega_e}\sin(\phi)\sin(\theta)\right] \end{cases}. \tag{3.34}$$

Then the position error induced can be expressed as

$$\varepsilon \approx \tan\left[\theta - \tan^{-1}\left\{\frac{\cos(\phi)\sin(\theta) - \dfrac{\omega_m}{\omega_e}\sin(\phi)\cos(\theta)}{\cos(\phi)\cos(\theta) + \dfrac{\omega_m}{\omega_e}\sin(\phi)\sin(\theta)}\right\}\right] \tag{3.35}$$

Simplifying (3.35) results in

$$\varepsilon \approx \frac{\omega_m}{\omega_e}\tan(\phi) \tag{3.36}$$

The position error is thus dependent on the speed ratio multiplied by the tangent of the phase difference. It is a constant error which is independent of the rotor position. If the phase difference is zero, there will be no position error.

3.5.6 Summary of estimated errors

The summary of approximated systematic position errors for an imperfect brushless resolver is listed in Table 1. The approximated errors from the inverse tangent method are compared with those from the tracking observer method [38]. It is found that both methods reach to the same prediction. It is interesting to note that the first two errors have the same frequency component forming a quadrature pair with a DC offset. The amplitude of each position error is about half of the resolver error. The last is a position independent DC offset error. Apart from the position error introduced by inductance harmonics, the position errors due to resolver imperfection can be compensated using the signal processing techniques in RDCs. The inductance harmonics is normally minimized by applying skewed rotor slots and additional

windings to produce opposing electromagnetic field to cancel the fields that create the harmonics [55].

Table 1 Summary of Estimated Position Errors for an Imperfect Resolver

Error Source	Approximated Position Error
Imbalance Amplitude α is the amplitude difference	$\varepsilon \approx \frac{\alpha}{2}\sin(2\theta)$
Quadrature Error β is the angular error	$\varepsilon \approx -\frac{\beta}{2}\left[1-\cos(2\theta)\right]$
Inductance Harmonics K_n is the inductance ratio	$\varepsilon \approx -\sum_{n=1}^{\infty} K_n \sin\left[(n-1)\theta\right]$
Phase Shift	$\varepsilon \approx \frac{\omega_m}{\omega_e}\tan(\phi)$

3.5.7 Accuracy and Allowable Errors' Constraints

Position error of a resolver system determines its accuracy. Since the resolver itself provides only the modulated outputs whose envelopes are the position signals, RDCs are necessary to retrieve the position angle. Thus the accuracy of a resolver system depends on both resolver and its conversion unit. The accuracy of a digital converter output is closely related to its resolution. If no error is introduced by the converter unit, the resolver accuracy will depend on the quality of the resolver output signals or its perfect construction, and the resolution of RDC which can be in the

range of 10 to 16 bits. If one-half of the least significant bit (1/2 LSB) accuracy is considered to be an allowable position error, the maximum position error will be

$$\left|\varepsilon\right|_{\max} = \pi 2^{-n}, \tag{3.37}$$

where n is the number of bits specified in RDC. The resolver's construction then has to set the allowable margins for its systematic errors to achieve the desired accuracy. For example, an RDC with the resolution of 12 bits, the allowable maximum position error is about 7.67e-4 radians or 0.0439 degrees. The individual systematic error constraints that impose to the resolver can be derived as shown in Table 2.

Table 2. Resolver Error Constraints for 12-bit RDC

	Amplitude imbalance	Quadrature error	Inductance harmonics	Phase shift
Allowable error	0.15%	2.636 arc-min	$\frac{M_2}{M_1} = 0.08\%$	0.439 degrees

In the derivation, the speed ratio is assumed to be 0.1 and only the second order inductance harmonic is considered. This illustrates how challenging it is to achieve the desired accuracy of a resolver. The individual allowable error limit is very small; the combined constraint will make it difficult to achieve the ideal resolver. Therefore, it is necessary to identify the resolver errors and compensate them to improve the accuracy.

3.6 Conclusion

The performance of a resolver depends on precision in manufacturing technique, operating principle and nature of the signal. The full mathematical description of a brushless resolver and field simulation reveals that ideal resolver signals are difficult to achieve in practice. Regarding the non-ideal resolver signals, four common error sources are considered and their respective error contributions to the accuracy are analysed. In order to obtain high position accuracy, the design constraints are found to be relatively small. Knowledge of error characteristics is essential for minimizing them by error compensation technique and development of alternative designs.

4 Demodulation by synchronous integration

4.1 Introduction

Systematic errors generally depend on manufacturing precision and capability. On the other hand, noise and disturbance are related to working environments and system setup. Since the resolver outputs are analogue, the noise contamination is unavoidable in practice. The hardware (analogue) or software (digital) filters are commonly applied to suppress the noise before estimating the position angle. However the delay introduced by filters can affect the position angle computation and accuracy. The effect of noise on accuracy of a resolver system is determined by how the RDC is implemented. This chapter proposes a new method of demodulation by synchronous integration to suppress the noise without using filters. The theoretical development of the proposed method is based on demodulation of the resolver outputs when the rotor is at stand-still condition. It is then extended to rotating operation. Simulations and experiments are carried out to demonstrate the effectiveness of the proposed method.

4.2 Demodulation methods and effect of noise

In every signal processing applications, noise is always present and unavoidable. Unlike the systematic errors presented in previous chapter, noise is random in nature and it is unpredictable. The effect of noise to a system is usually measured by a ratio called signal-to-noise ratio (SNR). It is defined as the ratio of signal power to the noise power, often expressed in decibels. If the SNR is so low that the position error generated by a non-ideal resolver is below the noise level, then there is no chance to compensate the systematic errors even though they are predictable. Therefore, noise must be supressed or filtered out before any other operations.

Depending on resolver and RDC specifications, resolver outputs are fed into preamplifiers before processing in RDC. These preamplifiers are integrated with analogue filters to remove the high frequency noise. This setup is normally found in applications with RDC chips. When digital signal processors (DSPs) are used in place of RDC chips to reduce the size and the cost, filtering process can be moved into DSP if the resolver outputs level is matched with analog to digital converter (ADC) of DSP. In this case, noise is reduced by digital filtering or software approach.

4.2.1 Demodulation by synchronous peak detection

Brief introduction of two common demodulation methods is described in section 1.4.5.1. The first is the synchronous peak detection and the second is the product detection. In terms of sampling, the signals are under-sampled in the synchronous peak detection method. This is because the sampling rate is the same as the excitation frequency and the sampling rate is below the Nyquist rate. The availability of the position angle or resolution is thus determined by the excitation frequency. Demodulation is achieved by sampling simultaneously the resolver outputs at the positive peak of the carrier as shown in Figure 4.1. In order to sample at the right instant, an additional noise free signal which is in quadrature to the excitation signal is required. The triggering signal to sample the data can be generated by detecting the zero crossings of the additional signal. Thus the peaks of modulated outputs are synchronously detected according to the quadrature excitation signal's zero crossings. The implementation of this demodulation method is presented in [34]. If the noise signal contains frequency components around the excitation frequency, then these components are aliased down to base band and distort the demodulated position signal. Therefore the peak detection method is prone to noise. However this demodulation method with inverse tangent computation can provide instantaneous estimates of the position and does not affect the dynamics of the servo control loop where the resolver is employed as an angular position sensor. It should be noted that

when noise level is low enough to employ this demodulation technique, the phase shift between the excitation and the resolver outputs needs to be compensated to achieve the high accuracy.

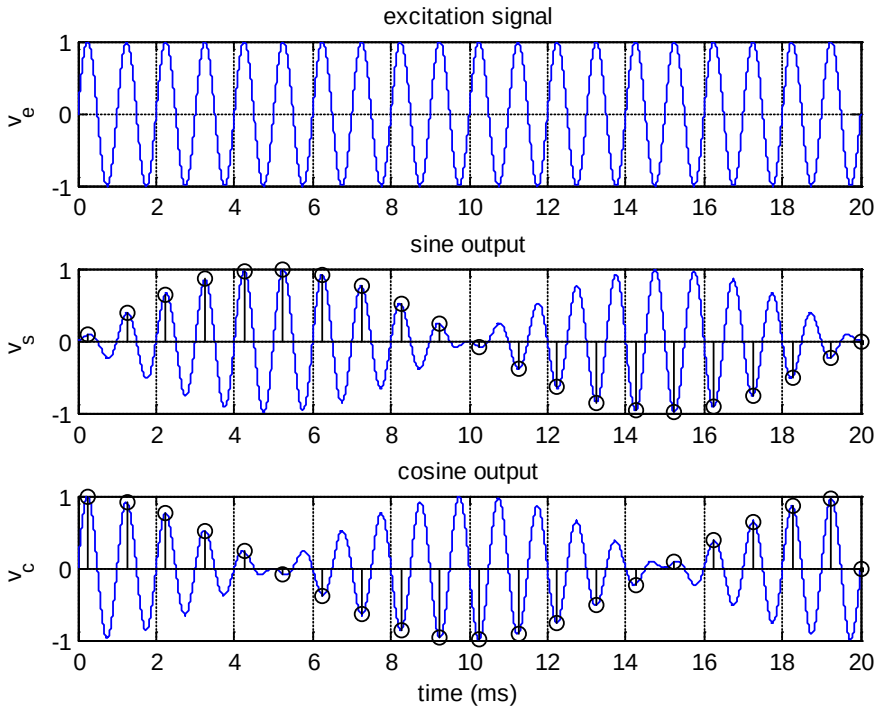

Figure 4.1. Demodulation by peak detection

4.2.2 Demodulation by product detection

Product detection method is essentially based on frequency shifting approach. For example, the sine winding output from a resolver with cosine expression of the excitation signal with angular frequency ω_e can be described by

$$v_s(t) = v_{\sin}(t)\cos(\omega_e t) \ . \tag{4.1}$$

In frequency domain, the equivalent expression using Fourier Transform can be given by

$$V_s(\omega) = \frac{1}{2} V_{\sin}(\omega - \omega_e) + \frac{1}{2} V_{\sin}(\omega + \omega_e) \ . \tag{4.2}$$

The modulation process of (4.2) is illustrated Figure 4.2.

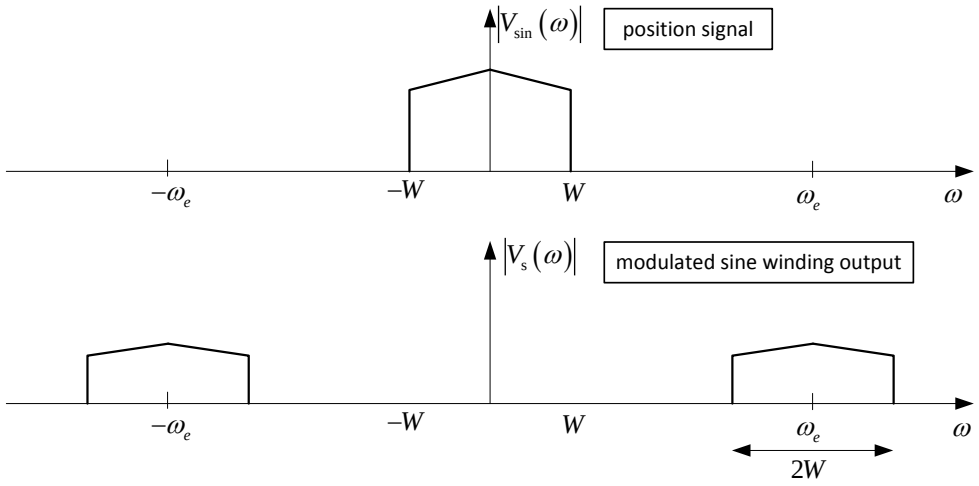

Figure 4.2. Modulation process in resolver operation

In the demodulation process, the modulated signal is multiplied by the signal which is synchronized with the excitation signal. It means that the modulated signal and the multiplying signal are assumed to have identical frequency and phase. By doing so, a multiplication factor having value of two is added to restore the original amplitude of the position signal. After multiplying, the resulting signal in frequency domain by applying Fourier Transform is

$$F\left\{2v_{\sin}(t)\cos^2(\omega_e t)\right\} = V_{\sin}(\omega) + \frac{1}{2} V_{\sin}(\omega - 2\omega_e) + \frac{1}{2} V_{\sin}(\omega + 2\omega_e) . \tag{4.3}$$

The illustration of (4.3) is shown in Figure 4.3.

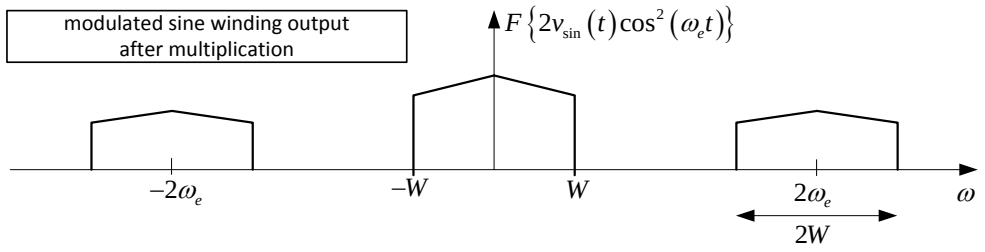

Figure 4.3. Sine winding output after multiplication

It can be seen that after multiplying with the excitation signal, a duplicate of the position signal is extracted from the modulated signal and moved back to the base band and the modulated signal is shifted to twice the original excitation signal frequency. If the noise frequency components are around the excitation frequency, they will be shifted together with excitation frequency to the higher band. When the low pass filter is applied to remove the high frequency term, the noise will be removed together. However, if the noise is spread across the frequency band the demodulated outputs will still be affected by the low frequency noise components. The resolver outputs are usually over sampled in this approach and the angular resolution is therefore higher than the peak detection method. In contrast to the peak detection technique, the dynamics of the servo control loop is affected by the time delay introduced by the filter.

4.2.3 Demodulation by band pass filtering and decimation

High resolution requirement is not as important as retrieving the accurate positon signal in demodulation. If the sparsely demodulated positions are accurate, an interpolation method can be incorporated in angle computation scheme to estimate the missing angular position values provided that the rotor is moving at constant during the estimation interval. This concept is realized in [32]. In their work, in order to reduce the computational cost in product detection method and to minimize the

noise effect, a demodulation technique by band pass filtering followed by decimation technique is implemented. The operation block diagram of demodulation is shown in Figure 4.4.

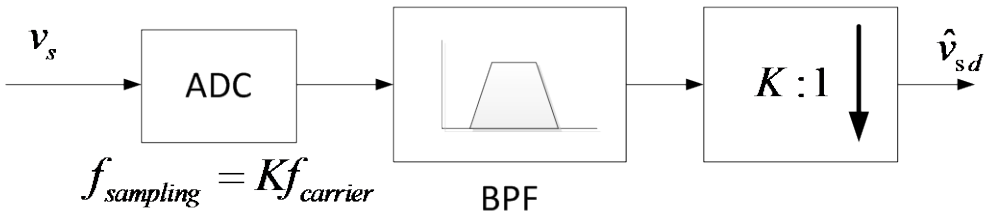

Figure 4.4. Demodulation by band-pass filtering and decimation

The implementation requires the over sampling technique. The modulated resolver outputs are sampled at K -times the excitation signal frequency. Like the sampling approach in peak detection, the resolver outputs are synchronously sampled with the excitation signal by K -times. In peak detection, they are sampled once only at the positive peak of the excitation signal. The digitized samples are then filtered through a finite impulse response (FIR) band-pass filter. After that, decimation is carried out by taking only every K^{th} sample from the filter outputs. The effective sampling rate is therefore the same as the excitation signal frequency. This demodulation method can be viewed as the combination of peak detection and product detection; instead of shifting the frequency to higher band, filtering is performed discarding both low and high frequency noise components around the excitation signal frequency, and the peak value is later resampled by taking the specific sample from the filter outputs. Due to the filter, a constant time delay is introduced. This delay can be compensated in the position angle computation process.

4.2.4 Other demodulation methods

Apart from the three methods described, there are a few other methods that can be used to demodulate the resolver outputs.

Using individual phase locked loops in product detection scheme can not only demodulate the resolver outputs but also compensate the phase shift between the excitation signal and the resolver outputs. But it is not economical.

Quadrature demodulation can also be implemented with more computational cost and complexity. The implementation requires that one of the resolver outputs to be shifted to 90° and the operations are similar to product detection method with additional mathematical manipulations of squaring, summation and taking square roots. This method can compensate the effects of noise, offset and phase shift [53].

4.3 Demodulation by synchronous integration: A robust demodulation method

Various demodulation methods are discussed in previous section. Each method has its own advantages and disadvantages. It is clear that demodulation with the single point sampling will not tolerate the noise unless analog pre-filters are applied. The demodulation methods with filtering can supress the noise, but it requires designing the filter; defining the filter order, computing filter coefficients, storing the coefficients in processor, performing the arithmetic operations of summation and addition. In order to simplify the filtering process and to retain the suppressing noise ability, a new demodulation method by synchronous integration is developed in this work, and the method will be called DBSI for short. The step by step developments of DBSI are detailed in the following sections.

4.3.1 Demodulation when the rotor is at stand-still

When the rotor is at stand-still, the resolver outputs with the sine excitation signal can be written as

$$\begin{cases} v_s(t) = V_s \sin(\omega_e t) \\ v_c(t) = V_c \sin(\omega_e t) \end{cases}, \tag{4.4}$$

where V_s and V_c represent the fixed amplitudes of the two sinusoidal waveforms. In other words, the excitation signal is scaled according to the transformation ratio and the fixed rotor position. This can be the initial condition when the resolver is energized and the rotor is at zero speed. The demodulation then implies finding the value of V_s and V_c. This is in fact an amplitude detection problem with the known frequency of a sinusoidal signal. The proposed method takes the advantage of the known frequency and chooses the integration approach to find the amplitudes as well as to average out the noise effects.

A sinusoidal signal without noise can be described by

$$y(t) = Y \sin\left(\omega t\right) = Y \sin\left[\theta\left(t\right)\right], \tag{4.5}$$

where Y is the amplitude of the waveform, ω the angular velocity in radians/sec and $\theta(t) = \omega t$. If the integration of $y(t)$ is performed over its half period, we obtain

$$I = \int_{t_0}^{t_1} y(t)dt = \frac{Y}{\omega}(\cos\theta_0 - \cos\theta_1), \tag{4.6}$$

where $\theta_0 = \omega t_0$, $\theta_1 = \omega t_1$ and $\theta_1 - \theta_0 = \pi$. When θ_0 is chosen to be such that $\cos\theta_0 = \pm 1$, the amplitude can be derived from

$$Y = \frac{\omega}{2} I. \tag{4.7}$$

Using this approach, V_s and V_c can be estimated by

$$\begin{cases} V_s = \dfrac{\omega_e}{2}\int_{t_0}^{t_1} v_s(t)d(t) \\ V_c = \dfrac{\omega_e}{2}\int_{t_0}^{t_1} v_c(t)d(t) \end{cases} . \tag{4.8}$$

The integration needs to be performed in a positive half cycle or a negative half cycle to extract the amplitude. The polarity of the amplitude can be positive or negative according to the integration period in (4.8). The recovery of the actual amplitude corresponds to the specific rotor position is therefore required. Applying the knowledge of the phase relationship between the excitation signal and resolver outputs as shown in Figure 4.5 and Table 3, we can retrieve the actual amplitude by multiplying the integrated result with the polarity of the excitation period, i.e., +1 for the positive half period and -1 for the negative half period.

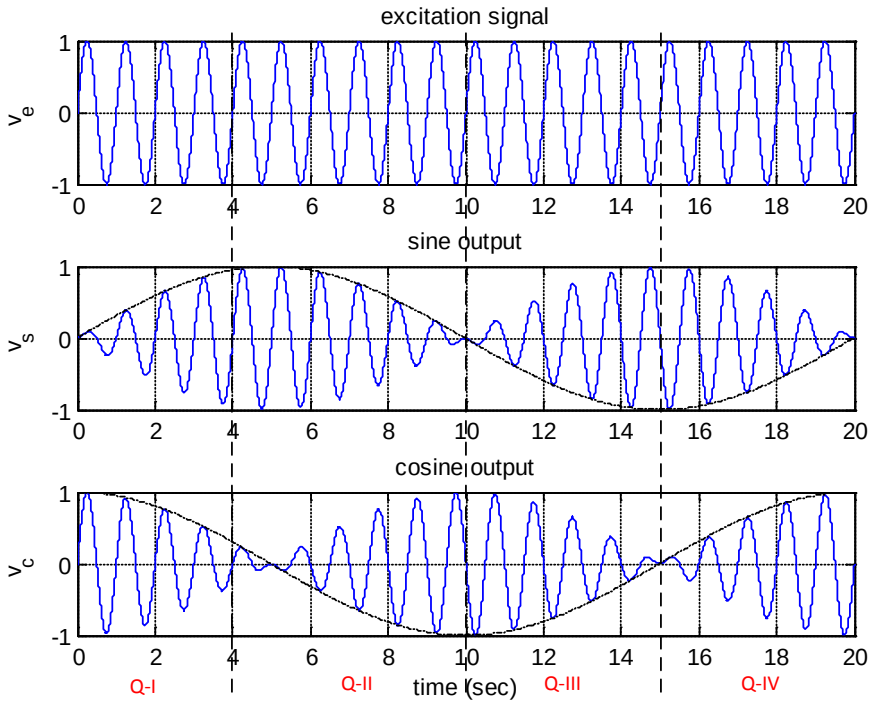

Figure 4.5. Four quadrants of the signals

Table 3. Phase Relationship

	v_e & v_s	v_e & v_c	v_s (*envelope*)	v_c (*envelope*)
Q-I	In phase	In phase	+ive	+ive
Q-II	In phase	Out phase	+ive	-ive
Q-III	Out phase	Out phase	-ive	-ive
Q-IV	Out phase	In phase	-ive	+ive

Since the amplitude is obtained at the end of the half period there is a delay of quarter period of sampling time. But it does not make any difference for the stand-still condition. This delay is a constant and it depends only on the excitation frequency. Therefore, the delay is easy to be handled. If the delay compensation is required, angle tracking observer can be used in angle estimation loop with the same delay in the feedback path. The details of the compensation will be presented in the angle computation.

4.3.2 Demodulation when the rotor is in motion

When the rotor is in motion, V_s and V_c in (4.4) are no longer constant and they vary according to the rotor position. In other words, the amplitude of the excitation signal is modified by the rotor position signal. When either one of the modulated waveforms in one excitation signal period is observed, it can be found that the sinusoid is deformed slightly. Since the integration approach is developed on the sinusoidal property of the waveform, it seems that the approach may not work for rotating conditions.

To resolve this, the position signal is assumed to be constant during the integration period, i.e. half the excitation signal period as shown in Figure 4.6. This

assumption is valid as long as the excitation frequency is reasonably higher than the rotor frequency. When the position signal amplitude is constant with the value at the midpoint of integration period, the excitation signal amplitude is just scaled by this midpoint amplitude value and the sinusoidal property is retained. Therefore, the integration method can be applied as in stand-still condition.

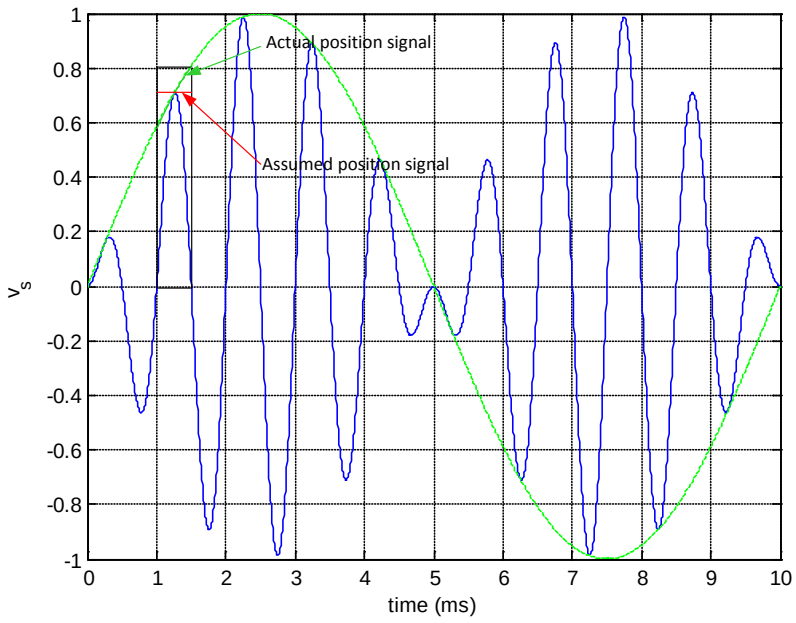

Figure 4.6. Assumption on position signal

It can be shown that this assumption can be relaxed to the condition when the rotor is moving with a certain constant speed during the integration period. Consider that the rotor is at a speed of ω rad/sec in that period. The resolver outputs can be described by

$$\begin{cases} v_s(t) = v_{\sin}(t)\sin(\omega_e t) = G_{\max}\sin(\omega t)\sin(\omega_e t) \\ v_c(t) = v_{\cos}(t)\sin(\omega_e t) = G_{\max}\cos(\omega t)\sin(\omega_e t) \end{cases}, \tag{4.9}$$

where $G_{\max}$ is the amplitude of the resolver outputs.

If the integration is carried out as before, we obtain

$$\begin{cases} I_1 = \int_{t_0}^{t_n} G_{\max} \sin(\omega t)\sin(\omega_e t)dt \\ I_2 = \int_{t_0}^{t_n} G_{\max} \cos(\omega t)\sin(\omega_e t)dt \end{cases}, \tag{4.10}$$

where the integration period is defined as $\theta_0 = \omega_e t_0$, $\theta_n = \omega_e t_n$ and $\theta_n - \theta_0 = \pi$ with $\theta_0 = k\pi$ for $k = 0,1,2,.....$. If we consider for even k 's , i.e., the positive half periods, (4.10) can be derived as

$$\begin{cases} I_1 = \dfrac{2\omega_e G_{\max}}{\omega_e^2 - \omega^2}\left[\sin\left\{\dfrac{\omega(t_n + t_0)}{2}\right\}\cos\left\{\dfrac{\omega(t_n - t_0)}{2}\right\}\right] \\ I_2 = \dfrac{2\omega_e G_{\max}}{\omega_e^2 - \omega^2}\left[\cos\left\{\dfrac{\omega(t_n + t_0)}{2}\right\}\cos\left\{\dfrac{\omega(t_n - t_0)}{2}\right\}\right] \end{cases}. \tag{4.11}$$

When $\omega_e \gg \omega$, (4.11) can be further simplified into

$$\begin{cases} I_1 \approx \dfrac{2G_{\max}}{\omega_e}\left[\sin\left\{\dfrac{\omega(t_n + t_0)}{2}\right\}\cos\left\{\dfrac{\omega(t_n - t_0)}{2}\right\}\right] \\ I_2 \approx \dfrac{2G_{\max}}{\omega_e}\left[\cos\left\{\dfrac{\omega(t_n + t_0)}{2}\right\}\cos\left\{\dfrac{\omega(t_n - t_0)}{2}\right\}\right] \end{cases}. \tag{4.12}$$

Thus, the amplitudes of position signals at time $\dfrac{t_n + t_0}{2}$ can be retrieved as

$$\begin{cases} V_{\sin}\left|_{\left(\frac{t_n+t_0}{2}\right)} = \dfrac{\omega_e}{2} I_1 = G_{\max}\left[\sin\left\{\dfrac{\omega(t_n + t_0)}{2}\right\}\cos\left(\dfrac{\omega}{\omega_e}\dfrac{\pi}{2}\right)\right] \right. \\ V_{\cos}\left|_{\left(\frac{t_n+t_0}{2}\right)} = \dfrac{\omega_e}{2} I_2 = G_{\max}\left[\sin\left\{\dfrac{\omega(t_n + t_0)}{2}\right\}\cos\left(\dfrac{\omega}{\omega_e}\dfrac{\pi}{2}\right)\right] \right. \end{cases}. \tag{4.13}$$

In contrast to the rotor at stand-still condition, the demodulated outputs when rotor is in motion are slightly scaled down by a factor. However this factor is common to both signals and so it does not affect the computation. Therefore, it can be concluded that the integration method is valid for the rotor at both stand-still and constant speed operating conditions.

4.3.3 Implementation issues of DBSI

To apply the proposed method, the fundamental requirement is oversampling. The accuracy of demodulation depends on how small the integration step or the sampling rate. Besides, the sampling rate must be the integer multiple of the excitation frequency so that the integration period exactly covers the positive or negative half cycle. Among the numerical integration methods, trapezoidal integration method is well suited for estimating the amplitude. The method can be implemented using the formula

$$\int_{t_0}^{t_0+T} f(t)dt = \frac{T}{n}\left[\sum_{k=0}^{n-1} f\left(t_0 + k\frac{T}{n}\right)\right], \tag{4.14}$$

where T is the integration interval. Unlike the digital filtering approach, it does not require to keep the filter coefficients and multiplications. The operation sums up the inputs and the result is multiplied once at the end of integration.

Another requirement of this method is the synchronous integration. It means that the start and the stop of the integration must be synchronized with the excitation signal's zero crossing points (ZCPs). In practice, there is usually a phase shift between the excitation signal and resolver outputs, and the available excitation signal cannot be used directly without compensation. A method to recover the carrier signal's ZCPs from the sensor outputs is therefore devised in the proposed solution.

The proposed method requires performing the integration for successive half-cycles. At the end of integration for one half-cycle, it is required to reset it to zero before starting integration for next half-cycle. Therefore, a triggering signal for integration reset (TSIR) is needed. By detecting the zero crossings of two sensor outputs as shown in Figure 4.7 , the TSIR can be generated. Since both outputs are modulated with the same carrier signal, either one of the outputs can be used by detecting its ZCPs. However due to the noise effect, some of the ZCPs from either

output are not reliable; especially the ZCPs around the region where the envelope amplitude is getting smaller. Both sensor outputs are therefore employed in TSIR generation in conjunction with switching logic to produce the accurate triggering signal by comparing the amplitudes of the modulated signals.

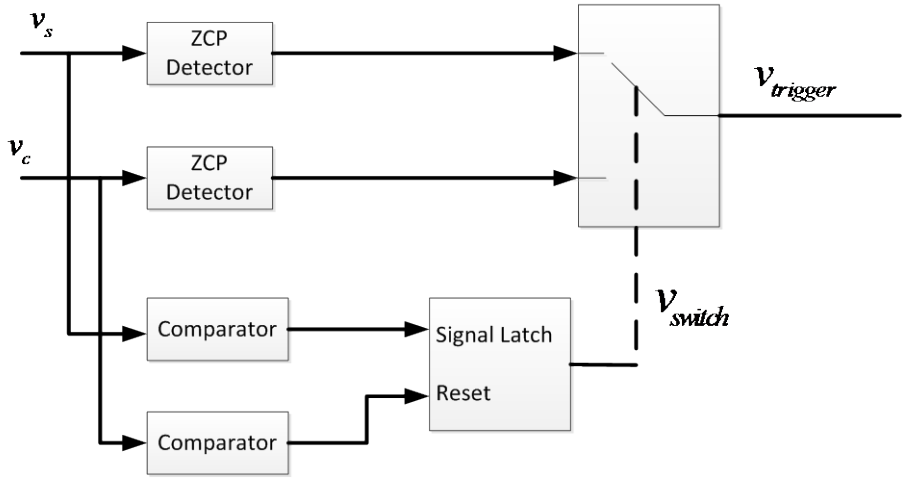

Figure 4.7. Trigger signal generation to reset integration

When making comparison, each comparator's reference value is set to be amplitudes of the position signal when the rotor is at π/4 radian. If one of the signal amplitude is greater than the reference value, the comparison result from this signal is latched until the other signal resets it. The switch waveform and its respective inputs are shown in Figure 4.8.

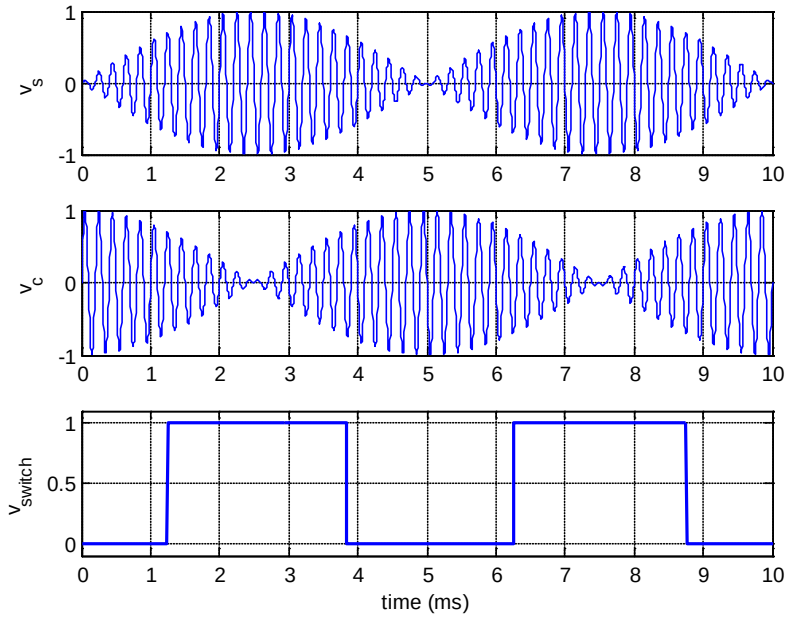

Figure 4.8. Resolver outputs and switching waveform

The switching logic operates as follows: when v_{switch} is high, the triggering signal is chosen from ZCPs of v_s, otherwise the triggering signal is selected from ZCPs of v_c. Thus the synchronous integration is carried out depending on the triggering signal input.

According to (4.12), the integration will yield positive and negative values. To restore the actual envelope as described in section 4.3, the polarity of excitation signal during the integration needs to be identified. Since the integration is completed at the end of the half excitation signal period, taking the amplitude of excitation signal as its polarity at this instant is not appropriate. Therefore the excitation signal is delayed for approximately π/4 period before polarity extraction. In this way, the correct envelope is retrieved making the demodulation process reasonably immune to the noise effect.

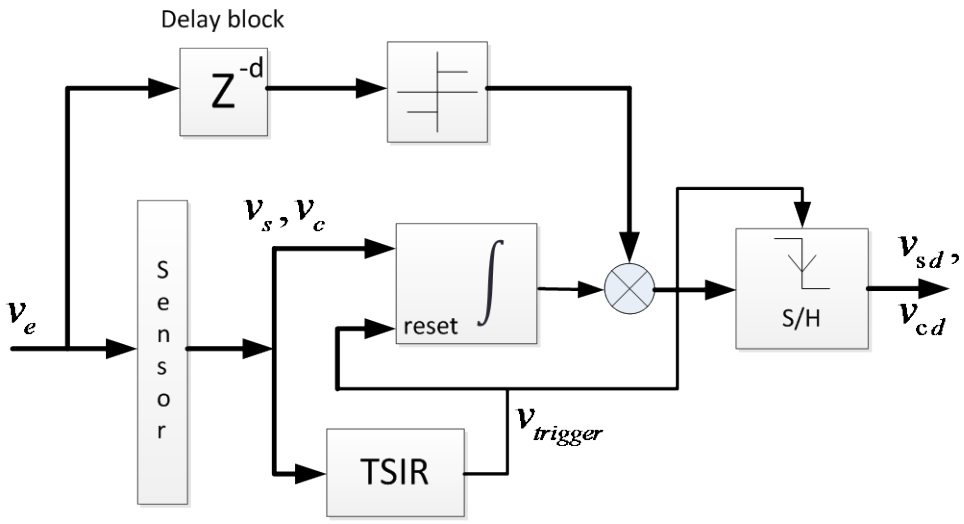

Figure 4.9. Demodulation by integration

The complete block diagram of the proposed method is shown in Figure 4.9. The operation can be summarized as follow: The sensor is energized by the excitation signal. The sensor outputs are integrated continuously and the integration is reset by the trigger signal at the end of each half-cycle. The integrator output is multiplied by the sign or the amplitude polarity of the delayed excitation signal to restore the correct envelope. The multiplied results are delivered to the sample and hold block which is controlled by the triggering signal. The final outputs are the demodulated signals which contain the rotor position information.

4.4 Simulation results of DBSI

In order to verify the effectiveness of the proposed DBSI method, ideal resolver model together with the demodulation by integration scheme is implemented in MATLAB SIMULINK environment. The setup for SIMULINK blocks diagram is provided in Appendix A. In addition, comparisons are made with three other demodulation methods, which are synchronous peak detection, band-pass filter with decimation method and product detection method.

4.4.1 Demonstration of the DBSI

Before the comparisons are made, the first simulation is carried out to illustrate the principle of operation in DBSI with the following parameters: rotor speed, 6000 rpm, excitation frequency, 5 kHz with unit amplitude, sampling frequency, 250 kHz and the transformation ratio, 1. Figure 4.10 shows the results from simulation. It can be seen that the algorithm performs well and the results are in good agreement with the theoretical predictions. It should be noted that noise is not considered in this simulation. The capability of noise suppression will be demonstrated by means of determining the position angle errors while comparing with other demodulation methods.

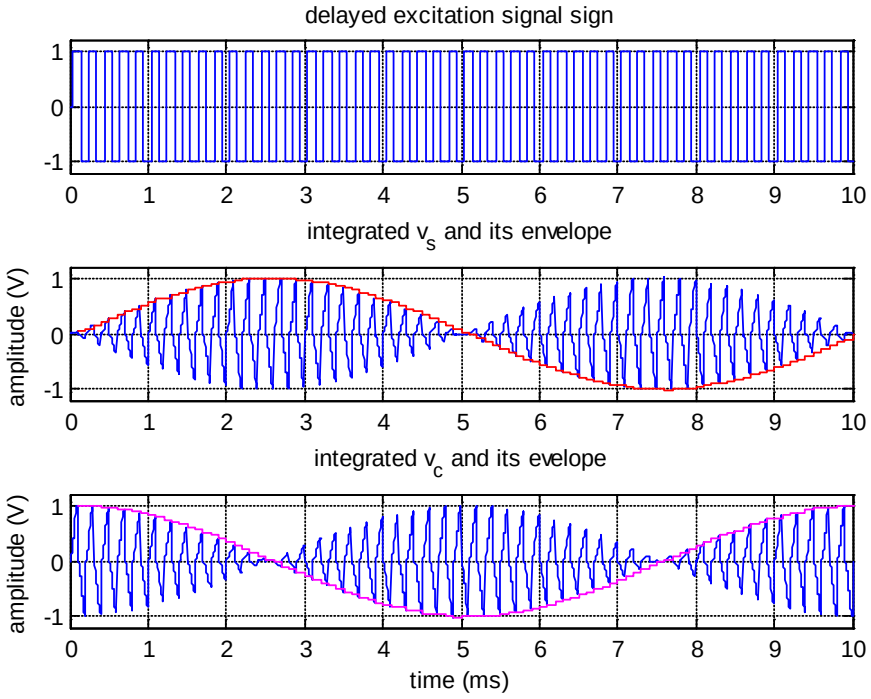

Figure 4.10. Demodulation by synchronous integration method

4.4.2 Evaluation of DBSI

The objective of the proposed DBSI is to demodulate the resolver outputs and to reduce the noise so that the accuracy of estimated angular positions can be improved. We compare the performance of the proposed method with three other methods in terms of accuracy or position error. The emphasis is set to demodulation with noise suppression and the angle computation is carried out using the MATLAB function *atan2( )* for all methods. To evaluate the performance of the demodulation methods, we consider the two operating conditions with different noise levels; SNR-40dB and SNR-30dB. The noise is generated from the additive white Gaussian noise process with zero mean and standard deviation, σ . The value of σ is chosen to obtain the require SNR given in decibels by

$$SNR = 10\log\frac{A^2}{2\sigma^2} \tag{4.15}$$

where A represents the amplitude of the position signal.

The estimated angular positions from all methods are compared with the result from noise free sensor outputs. The position errors are derived from the difference between the noise free position signals and the noise contaminated ones. By this way, the effect of noise on angular position estimation and the noise suppression ability of each method can be observed.

4.4.2.1 Simulation parameters

The simulation parameters for the resolver signals are same as before, i.e. rotor speed of 6000 rpm, excitation frequency of 5 kHz with unit amplitude, and the transformation ratio of 1. The resolver signals are assumed to be ideal except with the noise. In the parameters, the over sampling ratio is defined as

$$OSR = \frac{f_{sampling}}{f_{Nyquist}} \tag{4.16}$$

where $f_{sampling}$ is the sampling rate and $f_{Nyquist}$ the Nyquist rate which is twice the excitation frequency. The proposed method's OSR is set to be 25 in simulations.

The three other demodulation methods used to compare with the proposed method have the following simulation parameters.

The peak detection method: The sampling rate is equal to the excitation frequency.

The product detection method: The OSR is 2 and the order of the low-pass FIR filter is 24, which causes the 12 samples group delay. The filter response is shown in Figure 4.11.

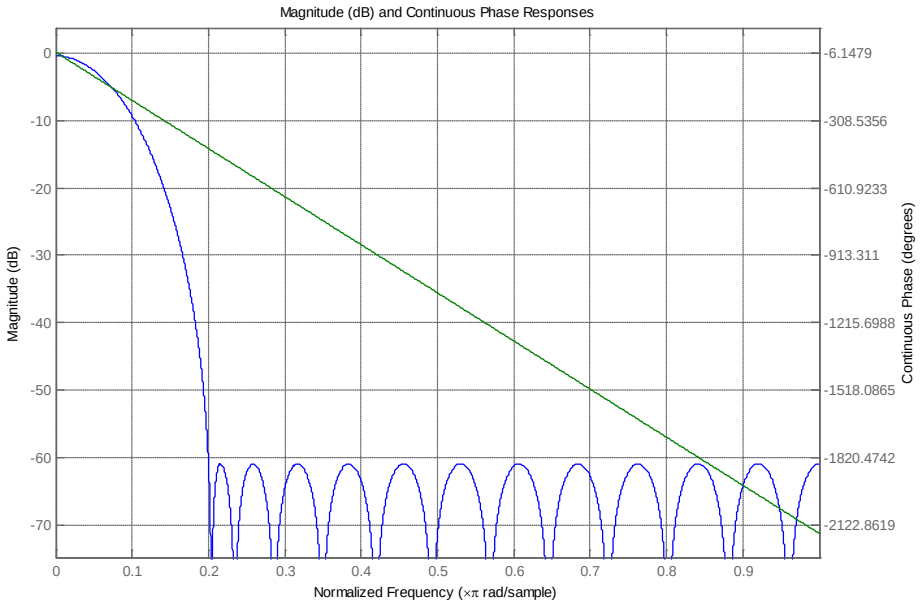

Figure 4.11. Low-pass filter response

Band pass filter and decimation method: The OSR is 4 and the order of the band pass FIR filter is 16. The filter response is shown in Fig. The filter output is decimated by

taking every 8th sample. This yields the effective sampling rate same as the excitation signal frequency.

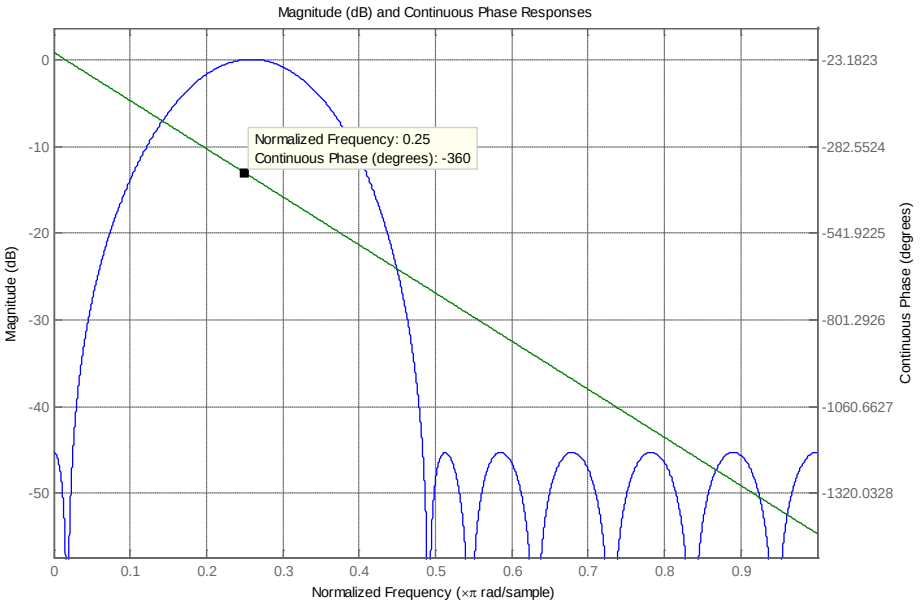

Figure 4.12. Band-pass filter response

4.4.2.2 Simulation results

The simulation result for the four demodulation methods with SNR 40dB is shown in Figure 4.13. The result shows that the peak position error is about 15 arc-min for the integration and product detection methods. However the other two methods have the peak error about 40 arc-min. By means of averaging effect, the proposed method effectively filters the noise and the performance is comparable to the filtering methods. It can be estimated that if a higher sampling rate is used for band-pass filtering followed by decimation method, position error due to noise can be further reduced. However, a higher sampling rate requires more filter taps and it in turn increases the computational load because more multiplications are involved.

Compared to the peak detection and band-pass filtering methods, the proposed DBSI has the position resolution two times higher since both positive and negative amplitudes in one excitation signal period are captured. The former two methods can also achieve the same resolution if the effective sampling rate is increased twice by sampling both positive and negative peaks, and the phase relationship is applied.

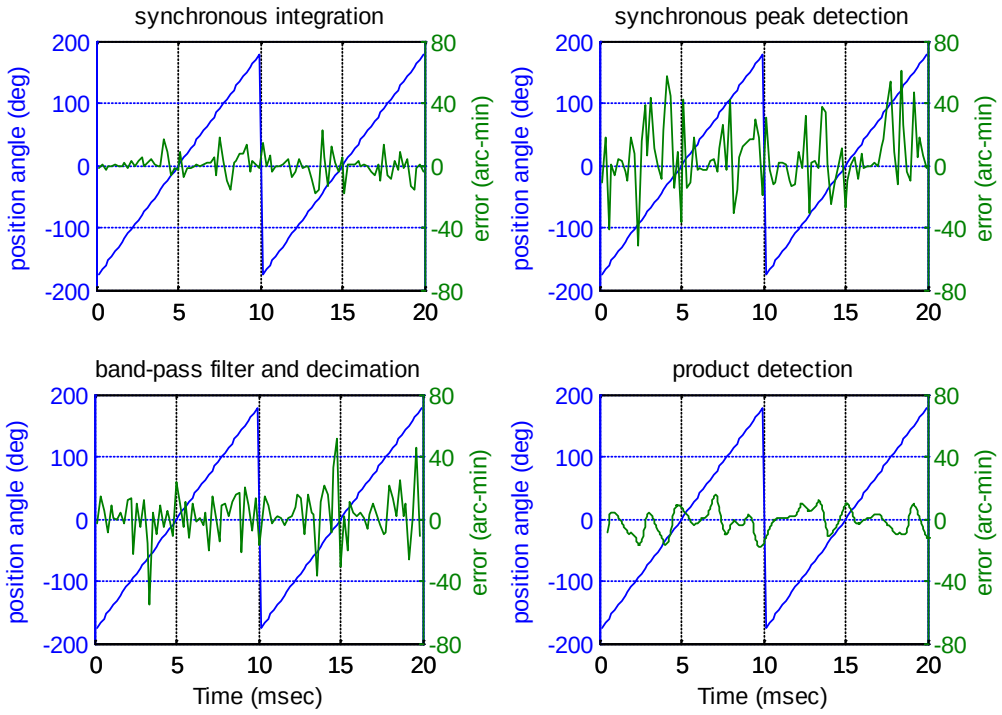

Figure 4.13. Estimated position angle and error at SNR 40dB

In order to investigate the performance of the proposed method with higher noise level, the identical simulation setup is used with SNR 30dB. The result shown in Figure 4.14 proves that the synchronous integration method is still able to supress the noise but the effectiveness is not as good as with low noise. This holds true for other methods as well.

In the proposed method, the integration period is determined by ZCPs of the modulated signals. Therefore the phase shift between the excitation signal and the

modulated signals does not affect the demodulation process. Among these four methods, the synchronous peak detection method and band-pass filtering followed by decimation method are associated with the excitation signal phase shift and the accuracy varies with the phase shift. The simulation result with the phase shift of 10° is shown in Figure 4.15. The results verify the effect of phase shift on four demodulation methods.

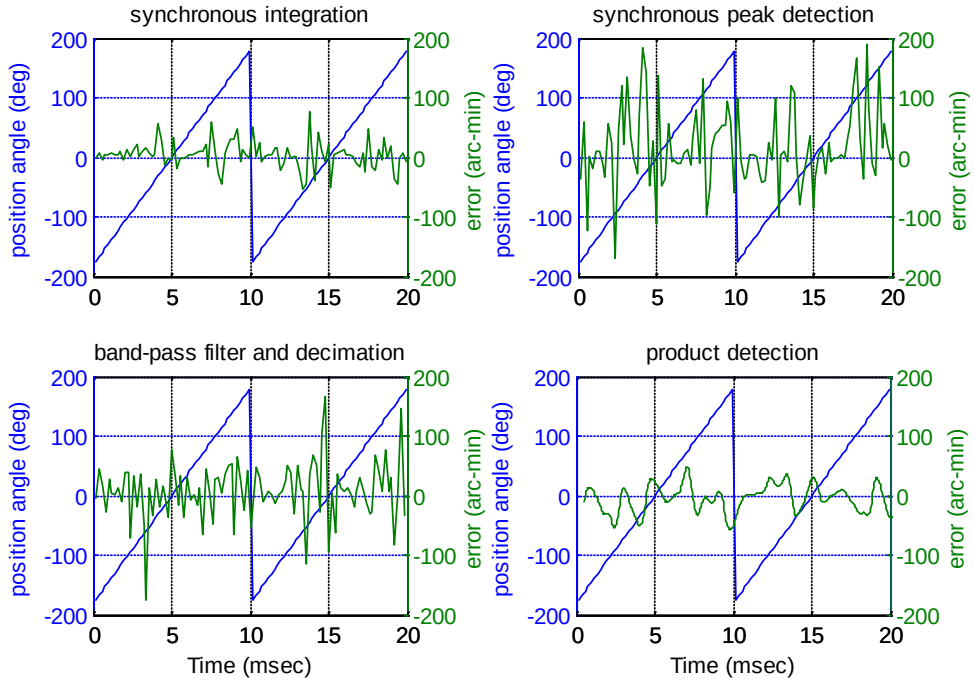

Figure 4.14. Estimated position angle and error at SNR 30dB

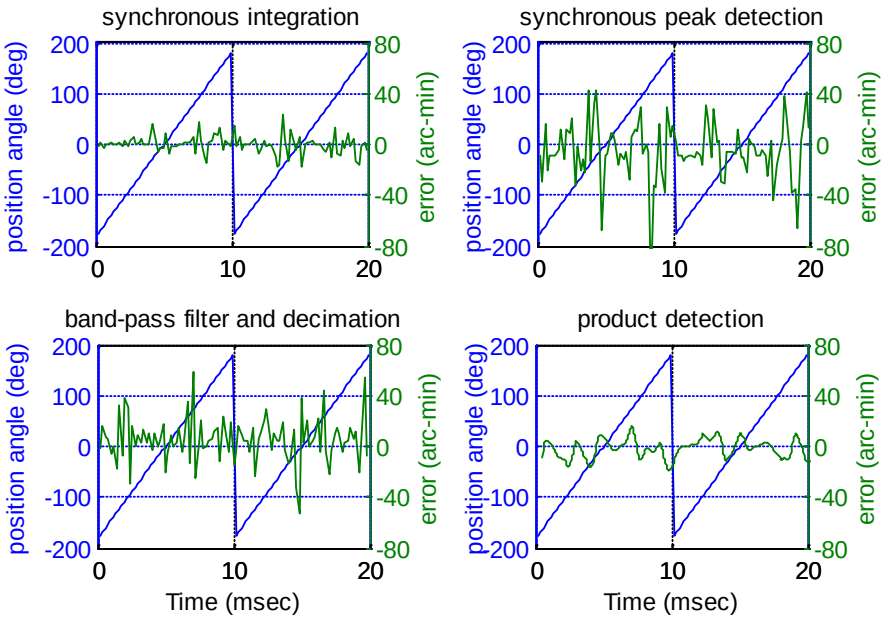

Figure 4.15. Estimated position angle and error at SNR 40 dB with excitation signal phase shift of 10 degrees

The performance of the four demodulation methods in terms of root mean square error (RMSE) is provided in Table 4. It shows that the proposed method can efficiently suppress the noise effect yielding more accurate position results. In addition, the proposed method is tolerant to the excitation phase shift as long as the phase shift does not affect the quadrant determination. RMSE is computed by

$$RMSE = \sqrt{\frac{1}{T}\int_0^T \left[\theta(t) - \hat{\theta}(t)\right]^2 dt} \ , \tag{4.17}$$

where T is the simulation time, θ the true angle, and $\hat{\theta}$ the estimated angle.

Table 4. RMSE comparison for different demodulation methods

	synchronous integration	peak detection	band-pass filter and decimation	product detection
SNR 40 dB	7.0878	21.423	15.0175	7.4293
SNR 30 dB	22.7522	67.6101	47.7434	23.4178
SNR 40 dB and phase shift 10 degrees	7.0878	22.7606	17.8699	7.5434

When these methods are to be realized in a DSP, their implementation cost should be considered. The general cost of each method is summarized in Table 5. The peak detection method is the simplest and least expensive method. However, its performance is sensitive to noise. The proposed method requires high oversampling but computational cost is lower than the filtering methods.

Table 5. Implementation cost of different demodulation methods

	synchronous integration	peak detection	band-pass filter and decimation	product detection
Number of multipliers	1	0	17	25
Number of adders	1	0	16	24
Number of states	2	1	16	24
MultPerInputSample	0	0	17	25
AddPerInputSample	1	0	16	24
Over Sampling Ratio	25	Under Sampling	4	2

4.5 Experimental results

The performance of the proposed method is also evaluated with the experimental data obtained from a single speed resolver mounted to the shaft of a spin-stand, which is a head positioning system used in hard disk drive magnetic recording. The specifications of the resolver are given in Table B. 1. The evaluation objective is to

demonstrate that the proposed algorithm can work well with the real resolver signals when the rotor rotates.

The experimental setup is shown in Figure 4.16. The excitation signal at 5 kHz is generated by National Instruments (NI) PXI-5406 and resolver outputs are simultaneously acquired by NI PXI-6133. Following the settings in simulation, the sampling frequency is set to 250 kHz. The rotor position detection is performed when the spindle motor is at the speeds of 300 rpm and 4200 rpm, respectively. The acquired data are processed using the proposed method on the SIMULINK platform to demodulate the resolver outputs. The rotor position is computed directly with the inverse tangent approach. It can be observed that the proposed method works well in demodulation to detect the rotor position.

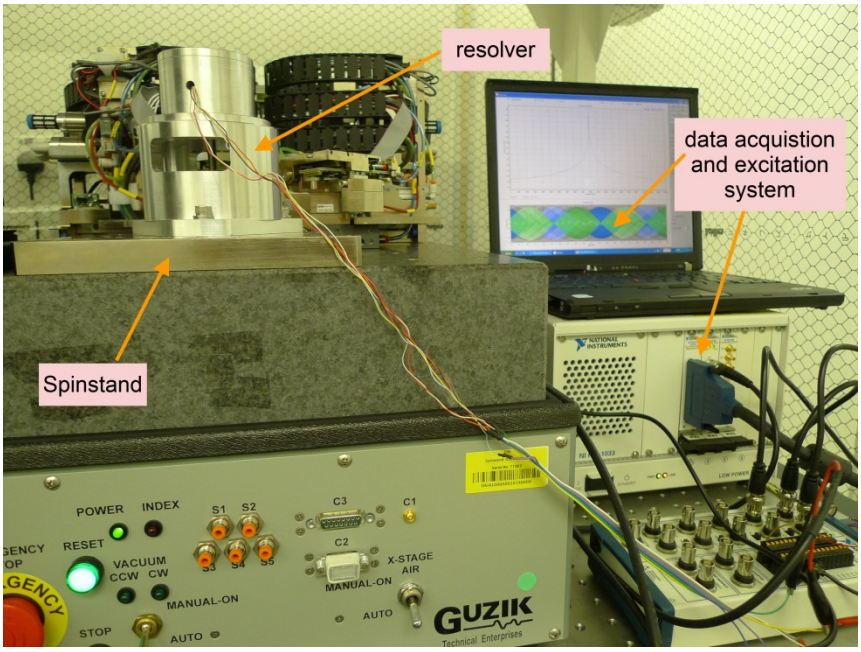

Figure 4.16. Experimental setup

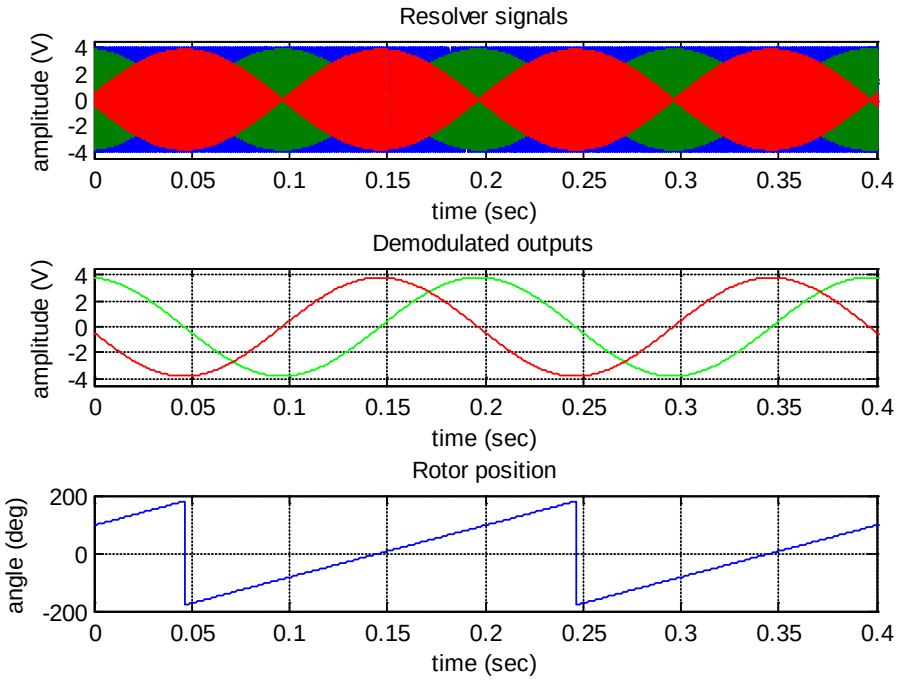

Figure 4.17. Rotor position detection at 300 rpm

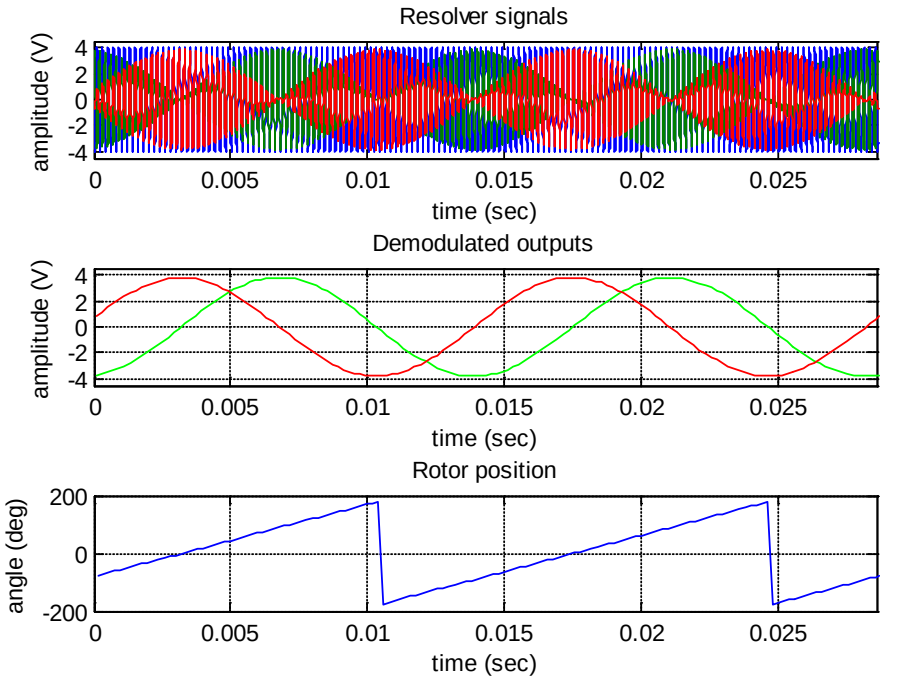

Figure 4.18. Rotor position detection at 4200 rpm

In order to compare the noise suppression capability of the proposed method with the other methods in terms of shaft position accuracy, we need an accurate position reference signal to compute the position errors. Since the position reference signal was not available, we derived it from the rotor speed which can safely be assumed constant. This assumption is valid because spin-stands are especially designed for running at the highly accurate constant speeds for writing/reading servo tracks to hard disk drive media. Using the position signal derived from the speed, the estimated RMSE for each method is obtained as shown in Table 6. It is found that the SNR for the experiment seems to be higher than the cases in simulation, and the experimental results are in good agreement with the simulation results. Noise suppression ability of DBSI is comparable to that of the filtering methods.

Table 6. Estimated RMSE comparison for different demodulation methods

	synchronous integration	peak detection	band-pass filter and decimation	product detection
RMSE at 300 rpm	0.1455	0.1913	0.1539	0.1435
RMSE at 4200 rpm	0.1561	0.2280	0.1593	0.1333

4.6 Conclusion

This chapter focuses on demodulation of the noise contaminated resolver outputs, which is the first step in resolver to digital conversion. Common methods in demodulation are first discussed in both theoretical and implementation aspects. Each method has its own advantages and disadvantages.

It is clear that single point sampling used in peak detection to demodulate the resolver outputs cannot reduce the noise. The accuracy of the position angles obtained from the peak detection method is prone to noise unless the analog pre-filters are employed.

The product detection method is well known to demodulate the amplitude modulated signal like resolver outputs, and it requires a considerable resources for arithmetic operations and filtering high frequency components. In addition, a time delay is introduced due to the filtering process and it can affect the dynamics of the servo control loop.

A more efficient demodulation method is the band-pass filtering followed by decimation. It does not require to perform the multiplication of the resolver outputs with the excitation signal and can filter the noise having both low and high frequency components. The effective sampling rate is the same as the excitation signal frequency. Because of the filter, a time delay is introduced but it is a constant and can be conveniently compensated in the angle computation scheme.

In order to supress the noise, an alternative demodulation approach without using filter is proposed in this chapter. It is based on the oversampling of the resolver outputs. Although it does not use the filters, the suppression of noise operation is similar to the operation of a running average filter. It exploits the sinusoidal property of the modulated signals and performs the synchronous integration for demodulation. The proposed method uses only the available signals to operate the resolver and requires less computational effort compared to the common filtering methods. The noise suppression ability of the proposed method is comparable to that of filtering approaches. The effectiveness of the noise suppression is proved with both simulations and experiments.

5 Initial calibration and error compensation

5.1 Introduction

In most measurement systems, calibration of a sensor is an essential routine to align the sensor to a known standard of accuracy, thereby ensuring that the measurement is making accurate and repeatable readings. Sensor calibration is required to improve the sensor performance by removing systematic errors in the sensor outputs. As presented in Chapter 3, the imperfect construction of a resolver can generate the systematic errors such as imbalanced amplitudes, quadrature error and inductance harmonics. If precision manufacturing process with stringent tolerance limits is employed, the accuracy can be better but with the increased cost. On the other hand, the systematic errors can be compensated in the calibration stage since they are predictable. The calibration parameters can be fed into conversion process to minimize the errors. However, the error parameters can vary with the age of resolver and sometimes they can vary with the working environment. In these cases, the online error compensation is needed in resolver to digital conversion stage to eliminate the errors adaptively and maintain the achievable accuracy. Various compensation techniques have been proposed in the literature focusing on the particular applications and working environments. This chapter proposes a general systematic approach applicable to both brushless and variable reluctance resolvers for initial calibration followed by the online error compensation scheme considering the specific systematic errors.

5.2 Systematic errors and their significance

Non-ideal resolver signals are resulted from imperfect resolver construction and the principle of resolver operation. As presented in Chapter 3, a resolver's structure itself is the error source for the systematic errors like imbalance amplitude,

quadrature error and inductance harmonics. On the other hand, application of transformer principle in operation can introduce the phase shift between the excitation signal and the resolver outputs due to winding resistance. The effect of phase shift depends on the frequency ratio of the excitation signal and the shaft speed. In general, the excitation signal's frequency is reasonably high so that the phase shift effect can be ignored. Moreover, the phase shift effect needs to be considered based on the choice of demodulation technique. It should be noted that the direct use of the excitation signal in demodulation process will be affected by the phase shift.

In systematic errors originated from the resolver's construction, the inductance harmonics can be minimized by adding complementary phases producing the opposite magnetic field to cancel out the even harmonics [37]. By skewing the rotor slots can also suppress the inductance harmonics. This skewing method is well employed in most of the commercial brushless resolvers. Hence, the calibration procedure and compensation method proposed in this chapter is confined to the systematic errors due to imbalance amplitude and quadrature error. The winding arrangement in brushless resolver construction avoids the generation of inductance offset. However, variable reluctance resolvers have all windings wound on the stator core and this generates the inductance offset resulting in a DC offset in the resolver outputs. Therefore, the DC offset is taken into account in the proposed method. Since noise is unavoidable in signal processing, its effect is also considered in the study.

5.3 Resolver error compensation

For an ideal resolver, when an excitation signal, $v_e(t) = V_e \cos(\omega_e t)$, is supplied to the input winding, the simplified resolver outputs can be given by

$$\begin{cases} v_s = KV_e \sin(\theta)\cos(\omega_e t) \\ v_c = KV_e \cos(\theta)\cos(\omega_e t) \end{cases}, \tag{5.1}$$

where K is the transformation ratio, and ω_e is angular frequency of the excitation signal. Equation (5.1) assumes that the rotor frequency is much lower than the carrier frequency in order to neglect the effect of speed voltage. Considering the amplitude imbalance, imperfect quadrature, DC offset and noise, one may describe the non-ideal resolver outputs as

$$\begin{cases} v_s = A_{\sin} \sin\left[\theta(t)\right]\cos(\omega_e t) + B_{\sin} + w_{\sin}(t) \\ v_c = A_{\cos} \cos\left[\theta(t) + \alpha\right]\cos(\omega_e t) + B_{\cos} + w_{\cos}(t) \end{cases}, \tag{5.2}$$

where $A_{\sin}$ and $A_{\cos}$ are the amplitudes of the resolver outputs, α is the phase difference accounting for the imperfect quadrature, $B_{\sin}$ and $B_{\cos}$ are DC offsets, and $w_{\sin}$ and $w_{\cos}$ represent the random noises. The estimated position angle from the signals in (5.2) without noise can be evaluated as

$$\hat{\theta} \approx \theta + \frac{1}{A_{\sin}}\left\{\frac{\eta}{2}\sin(2\theta) + \left(-B_{\sin}\cos\theta + B_{\cos}\sin\theta\right) + \frac{A_{\cos}\alpha}{2}\left[\cos(2\theta) - 1\right]\right\}, \tag{5.3}$$

where $\eta = A_{cos} - A_{sin}$. Thus the estimated angle will compose of true angular position and additional error terms.

In order to minimize the errors, there are basically two places to identify the existence of errors in a resolver system as shown in Figure 5.1. The two locations correspond to the two equations, (5.2) and (5.3), respectively. The first place is the direct outputs from the resolver sensor and the second place is the RDC output. As RDC normally will not contribute additional errors except digitization errors, the errors identification at the first place is chosen for the proposed initial calibration method. In this case, the compensation scheme will correct the distorted resolver outputs in (5.2) before computing the position angle in RDC. On the other hand, if the

compensation scheme is to be carried out at the second place the position angle is already computed and error terms should be suppressed or filtered out.

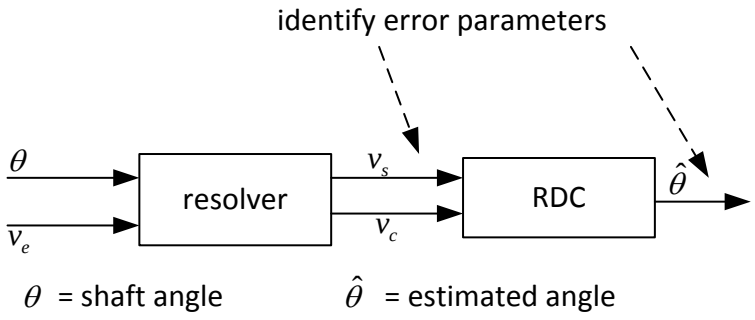

Figure 5.1. Identification of error parameters

As discussed in Introduction, initial calibration is sometimes not enough to maintain the accuracy of a resolver system. Therefore, online error compensation is also necessary to adaptively correct the signals in case there are any changes in the error parameters. The online error compensation is devised in such a way that it can utilize the initial calibration parameters. The developmental details of the method will be presented later.

5.4 Sinusoidal parameters estimation based initial calibration method

Based on (5.2), the proposed calibration procedure needs to determine the following parameters: A_{sin}, A_{cos}, B_{sin}, B_{cos} and α, to correct the non-ideal resolver signals. When these parameters are obtained, the demodulated resolver outputs can be compensated as below:

$$\begin{cases} \sin\left[\theta(t)\right] = \dfrac{v_s - B_{\sin}}{A_{\sin}} \\ \cos\left[\theta(t)\right] = \dfrac{\dfrac{v_c - B_{\cos}}{A_{\cos}} + \sin\alpha \sin\left[\theta(t)\right]}{\cos\alpha} \end{cases} \tag{5.4}$$

In order to estimate these parameters, the proposed method depends on the availability of a high precision rotary stage, which can provide the accurate angular position reference. Figure 5.2 shows how the calibration method works. The shaft angular position input is fed to the resolver via a high precision rotary stage and the resolver is excited by a sinusoidal signal with known amplitude and frequency. The resolver outputs are sampled and the estimation is carried out by the three-step calibration method. In the estimation process, the known parameters are θ, v_s, v_c and ω_e.

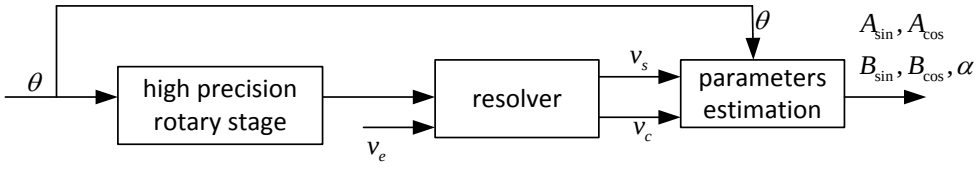

Figure 5.2. Calibration procedure

To develop the proposed calibration method, a more general form of (5.2) is expressed by

$$\begin{cases} v_s = A_{\sin} \sin\left[\theta(t) + \phi_{\sin}\right] \cos\omega_e t + B_{\sin} + w_{\sin} \\ v_c = A_{\cos} \cos\left[\theta(t) + \phi_{\cos}\right] \cos\omega_e t + B_{\cos} + w_{\cos} \end{cases}. \tag{5.5}$$

The alternative form of (5.5) with concealing the phase information is

$$\begin{cases} v_s = Y_s\left[\beta_s(t)\right] \cos\omega_e t + B_{\sin} + w_{\sin} \\ v_c = Y_c\left[\beta_c(t)\right] \cos\omega_e t + B_{\cos} + w_{\cos} \end{cases}, \tag{5.6}$$

where,

$$\begin{cases} Y_s\left[\beta_s(t)\right] = A_{\sin}\sin\left[\theta(t)+\phi_{\sin}\right] \\ Y_c\left[\beta_c(t)\right] = A_{\cos}\cos\left[\theta(t)+\phi_{\cos}\right] \end{cases}. \tag{5.7}$$

With the information of known parameters, the required calibration parameters can be estimated by acquiring the resolver output signals at a few stationary rotor positions by following the three steps described below:

Step 1. $B_{\sin}$ and $B_{\cos}$ are estimated by determining the means of the acquired data,

$$\begin{cases} \hat{B}_{\sin} = \dfrac{1}{M}\sum_{n=1}^{M} v_s[n] \\ \hat{B}_{\cos} = \dfrac{1}{M}\sum_{n=1}^{M} v_c[n] \end{cases}, \tag{5.8}$$

where M is the total number of samples.

Step 2. Since the excitation frequency is known, amplitudes of the resolver outputs at the specific positions described in (5.6) can be estimated by the Discrete Fourier Transform (DFT),

$$\begin{cases} \hat{Y}_s\left[k_{\omega_e}\right] = \dfrac{2}{M}\sum_{n=0}^{M-1} v_s[n] e^{-j\frac{k_{\omega_e}}{M}n} \\ \hat{Y}_c\left[k_{\omega_e}\right] = \dfrac{2}{M}\sum_{n=0}^{M-1} v_c[n] e^{-j\frac{k_{\omega_e}}{M}n} \end{cases}. \tag{5.9}$$

Using the DFT to estimate the amplitudes inherently removes the random noises w_{sin} and w_{cos}.

Step 3. A_{sin}, A_{cos} and α are estimated applying Linear Least Square Estimation (LLSE) to (5.7) with the results from Step 2. LLSE can be used considering a general real sinusoid of the form

$$x\left[\theta(n)\right] = A_0 + A\cos\left[\theta(n)+\phi\right] + w[n] \qquad , n = 1,...,N \ , \qquad (5.10)$$

where $x[\theta(n)]$ and $\theta(n)$ are known and A_0, A and ϕ the parameters to be estimated. The nonlinearity in the phase parameter can be overcome by using the trigonometric expansion

$$A\cos\left[\theta(n)+\phi\right] = A\cos\left[\theta(n)\right]\cos\phi - A\sin\left[\theta(n)\right]\sin\phi \qquad (5.11)$$

The system of equations obtained from the different rotor positions can be expressed in matrix form as

$$\mathbf{x} = \mathbf{H}\boldsymbol{\alpha} + \mathbf{w} \ , \qquad (5.12)$$

where,

$$\mathbf{x} = \begin{bmatrix} x_1 & x_2 & \dots & x_M \end{bmatrix}^T , \quad \mathrm{w} = \begin{bmatrix} w_1 & w_2 & \dots & w_M \end{bmatrix}$$

$$\mathbf{H} = \begin{bmatrix} 1 & \cos\left[\theta(1)\right] & \sin\left[\theta(1)\right] \\ \vdots & \vdots & \vdots \\ 1 & \cos\left[\theta(M)\right] & \sin\left[\theta(M)\right] \end{bmatrix} \ , \ \boldsymbol{\alpha} = \begin{bmatrix} A_0 \\ A\cos(\phi) \\ A\sin(\phi) \end{bmatrix} = \begin{bmatrix} \alpha_1 \\ \alpha_2 \\ \alpha_3 \end{bmatrix} \qquad . \ (5.13)$$

Then, Linear Least Square Estimate for $\boldsymbol{\alpha}$ is

$$\boldsymbol{\alpha} = \left(\mathbf{H}^T\mathbf{H}\right)^{-1}\mathbf{H}^T\mathbf{x} \ . \qquad (5.14)$$

Once the $\boldsymbol{\alpha}$ is known, the required parameters can be retrieved by

$$\hat{A} = \sqrt{\hat{\alpha}_2^2 + \hat{\alpha}_3^2} \quad , \ \hat{\phi} = \tan^{-1}\left(\frac{-\hat{\alpha}_3}{\hat{\alpha}_2}\right) . \qquad (5.15)$$

5.4.1 Quantitative analysis on amplitude estimation with DFT

DFT is chosen to determine the amplitudes of the sinusoids in (5.6) so that random noises will not affect the estimated results. Since the calibration is carried out at the stationary rotor positions with the known frequency, DFT is generally a logical choice to estimate the amplitude. The accuracy of DFT is decisive in the calibration process because LLSE uses the results from DFT and produces the final estimated parameters.

The performance of DFT depends on the sampling rate, F_s, total number of samples, M, severity of the noise level which can be described by signal-to-noise ratio, SNR and the frequency of the sinusoid, f_e. Although it is generally known that more number of samples, and higher SNR would yield the better estimation results, the quantitative analysis to choose the right values of the parameters, for example, the suitable sampling rate for a specific SNR and a specific number of samples, is not available. Therefore, a quantitative analysis is carried out before the calibration process to identify the suitable sampling rate and the number of samples for a certain SNR.

Analysis is performed on MATLAB computing platform. Since random noise is considered in operation, a series of simulations is carried out to analyse the results statistically. In order to neglect the effect of phase in the sinusoid, the whole cycles are acquired by setting the oversampling ratio, OSR, to be integer values. It means that there is no DFT leakage effect exists in estimation. The number of samples is then described in terms of number of cycles of the sinusoid whose amplitude is to be estimated. To observe the possible error distribution, the estimation error which is the difference between the true value and estimated value is shown using the probability density function (pdf).

Figures 5.3 ~ 5.4 show the simulated results to highlight the effect of number of samples and the sampling rate while the SNR is assumed to be 40dB.

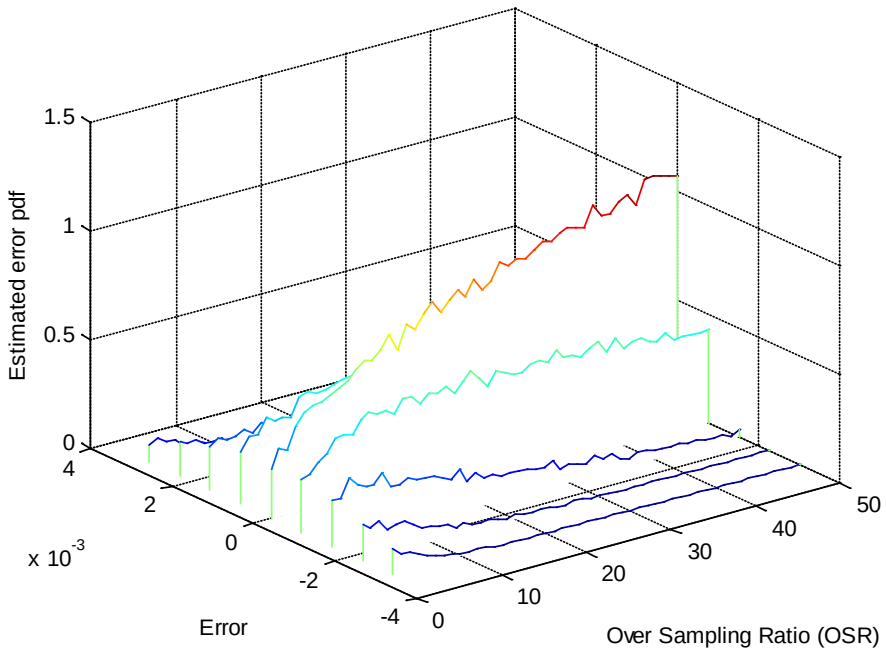

Figure 5.3. Estimated error pdf (number of cycles = 4, SNR = 40 dB)

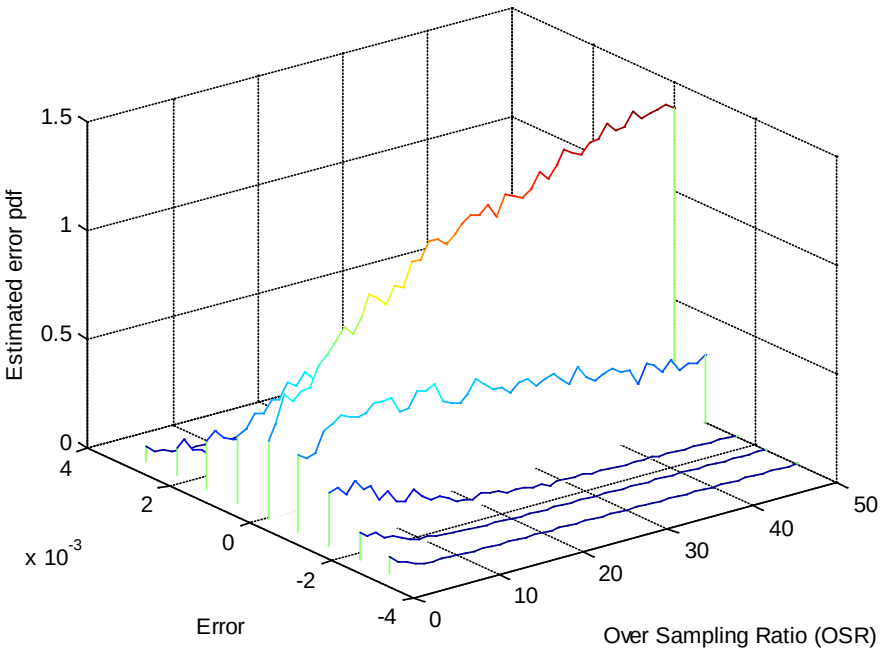

Figure 5.4. Estimated error pdf (number of cycles = 8, SNR = 40 dB)

In general, increasing OSR and the number of samples can reduce the error and exponential like reduction is observed. The quantitative analysis indicates that the suitable oversampling ratio (or) sampling rate can be chosen for a given number of samples and SNR, depending on the desired error limits. For example, as can be seen in Figure 5.3, with four cycles of data, OSR =25 is good enough to restrict the error to be in the range of $\pm 2\times 10^{-3}$. Increasing OSR to a higher value is not much beneficial to reduce the error.

5.4.2 Simulation results

An evaluation of the parameter estimation in the proposed calibration method is performed by setting the parameters as the following: A_{sin} = 1.1, A_{cos} = 0.95, ϕ_{sin} = 0 deg, ϕ_{cos} = 0.5 deg, B_{sin} = 0.2, B_{cos} = 0.1, ω_e = 10000π rad/s, and SRN = 40 dB. For data sampling, OSR is set to be 25 and DFT is performed for four cycles. The data is acquired at three rotor positions: 10 deg, 20 deg and 30 deg. The estimated values and errors are listed in Table 7.

Table 7. Parameters estimation in resolver outputs

	Actual value	Estimated value	Estimation error
$A_{\sin}$	1.1	$1.09999989E+00$	$1.12E-07$
$A_{\cos}$	0.95	$9.49999996E-01$	$4.49E-09$
$B_{\sin}$	0.2	$1.99756674E-01$	$2.43E-04$
$B_{\cos}$	0.1	$9.97898545E-02$	$2.10E-04$
$\phi_{\sin}(\deg)$	0	$1.02296158E-05$	$-1.02E-05$
$\phi_{\cos}(\deg)$	0.5	$5.00000019E-01$	$-1.89E-08$

5.4.3 Experimental setup

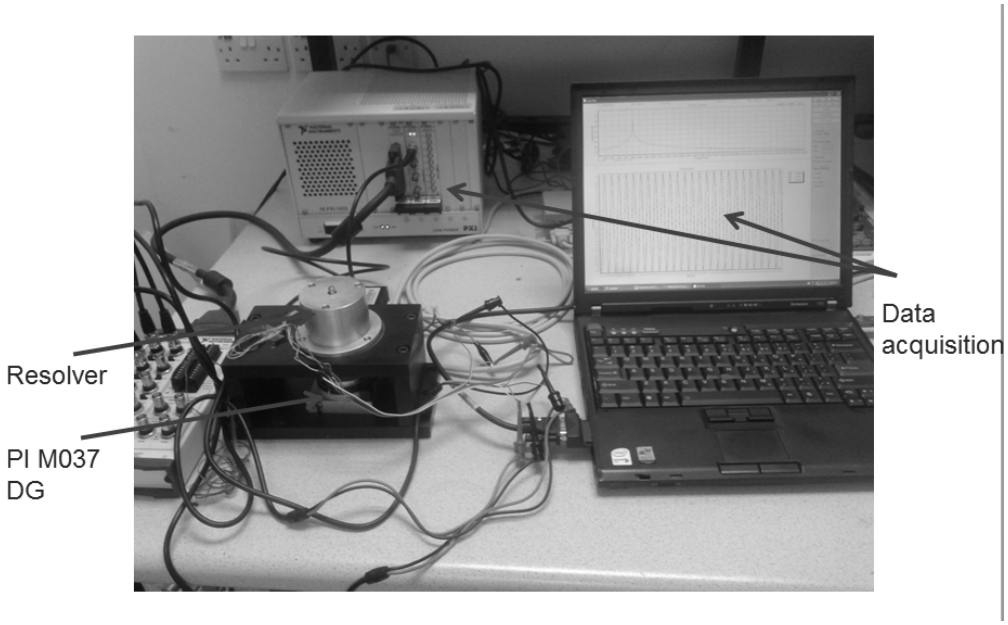

Figure 5.5. Experimental setup

To validate the proposed calibration method with a commercial resolver, experiments are performed using the setup shown in Figure 5.5. In the setup, the resolver is rotated by the high precision rotary stage, PI M037 DG. The rotation of the stage is controlled by PI C-863 DC Motor Controller. The specifications of the resolver and the rotation stage are described in Appendix B. The excitation signal is supplied to the resolver using NI PXI-5406 and the resolver outputs are simultaneously sampled using NI PXI-6133. Data are acquired and stored in the computer by a software module which is developed using Visual C++ programming language.

5.4.4 Experimental results

Using the setup shown above, a carrier signal having the amplitude of 5V and frequency of 5 kHz is supplied to the resolver. The resolver outputs are sampled at the rate of 250 kS/s. Data acquisition is performed at five rotor positions. The effect of number of cycles in parameters estimation is shown in Figures 5.6 ~ 5.8. It can be

seen that the increased number of cycles results in a steady value of the estimated parameters. However the difference between the initial value and the final steady state value is not much different and they are in the order of 10^{-3}.

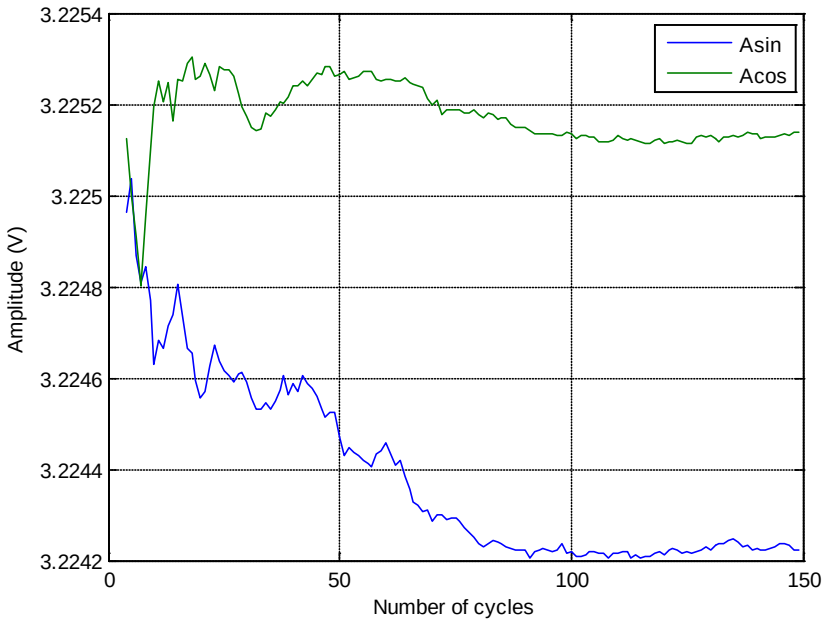

Figure 5.6. Estimation of amplitudes of resolver outputs

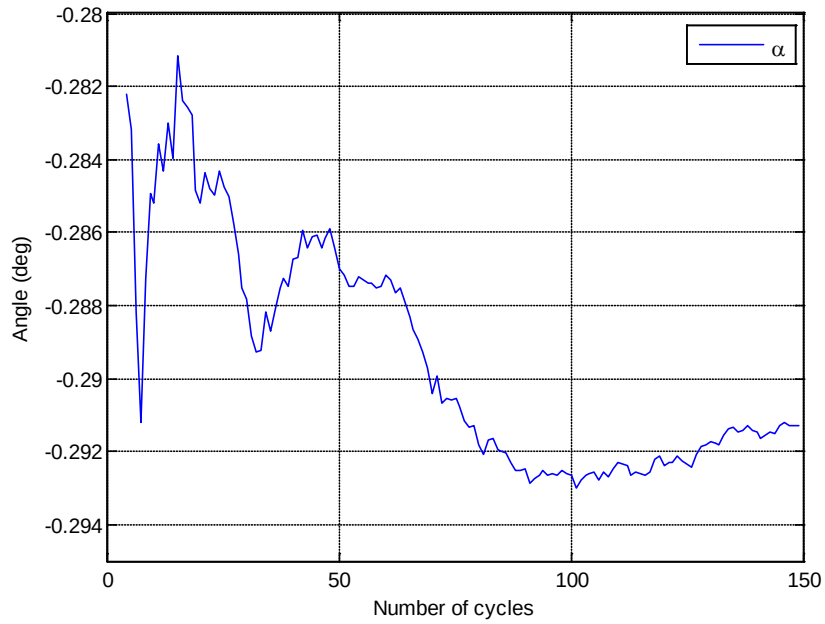

Figure 5.7. Estimation of quadrature error in resolver outputs

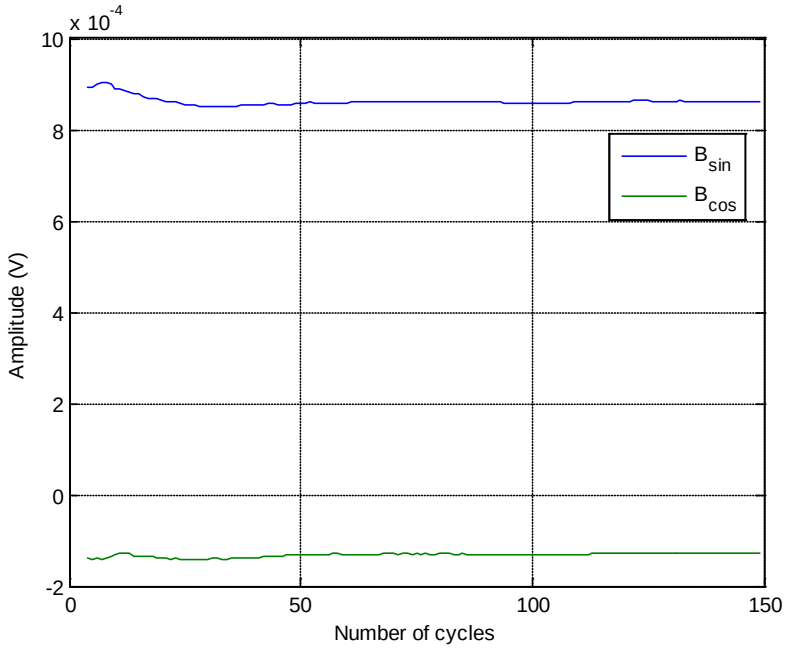

Figure 5.8. Estimation of DC offset in resolver outputs

Following the parameter estimation in the proposed calibration method, it is found that the resolver under test has an estimated amplitude imbalance of 0.09%, the quadrature error of 17.5 arc-min, DC offsets of 0.09mV and 0.013 mV. Comparison is made between the actual measurement and curve fitting of the calibration data obtained from LLSE. Figure 5.9 shows the comparison results. It is observed that the calibration data using the proposed method is in good agreement with the measurement data for the first half of the revolution. However there is a significant difference in the second half of the revolution. The reason for this difference could be the imperfect installation which is not considered in the error model. Some possible contributions to the imperfection are shaft eccentricity, assembly eccentricity, axial misalignment and radial misalignment.

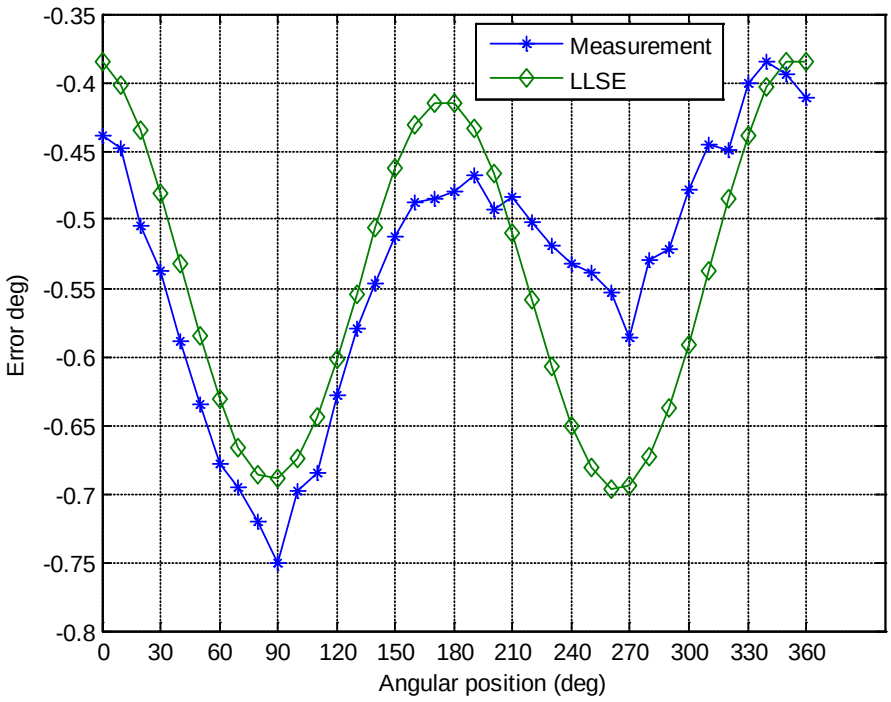

Figure 5.9. Comparison of error profiles obtained from measurement and estimation

5.5 Complex Fourier expression of demodulated non-ideal resolver outputs

The proposed online error compensation method is based on the complex exponential expression of the demodulated resolver outputs. Therefore, this section presents the mathematical development to express the demodulated non-ideal resolver outputs in complex Fourier series. A general complex exponential signal may be defined as

$$\overline{x}(t) = Ae^{j(\omega_0 t+\phi)} , \tag{5.16}$$

where $A = |\overline{x}(t)|$, is the magnitude of $\overline{x}(t)$ and the angle of $\overline{x}(t)$ is $(\omega_0 t+\phi)$. The complex exponential signal can be expressed in the Cartesian form as

$$\overline{x}(t) = Ae^{j(\omega_0 t+\phi)} = A\cos(\omega_0 t+\phi) + jA\sin(\omega_0 t+\phi). \tag{5.17}$$

Thus, the real and imaginary parts of the complex exponential signal are two orthogonal signals analogous to the demodulated ideal resolver outputs, which can be given by

$$\overline{z}_{ideal}(\theta) = Ge^{j\theta} = G\cos(\theta) + jG\sin(\theta) = v_c + jv_s \ . \tag{5.18}$$

When the non-ideal resolver outputs with imbalance amplitude and quadrature error are considered, the expression is changed into

$$\overline{z}_{non-ideal}(\theta) = A_{\cos}\cos(\theta) + jA_{\sin}\sin(\theta+\alpha) \ . \tag{5.19}$$

The equivalent expression of (5.19) with random noise is described by (5.2). In complex exponential form, these errors will appear as the negative frequency component as below:

$$\overline{z}_{non-ideal}(\theta) = \frac{1}{2}\left[\left(A_{\cos} + A_{\sin}e^{j\alpha}\right)e^{j\theta} + \left(A_{\cos} - A_{\sin}e^{-j\alpha}\right)e^{-j\theta}\right] . \tag{5.20}$$

Based on the fact that the imbalance amplitude and quadrature error would generate the negative frequency component in complex expression and the DC offsets would not vary with the angular position, the demodulated resolver outputs with imbalance amplitude, quadrature error and DC offsets in complex Fourier series expansion is introduced by Bunte [42]. The complex series expression of the demodulated non-ideal resolver outputs considering these three systematic errors is defined by

$$\overline{z}(\theta) = \left[\left(A_{\cos} - A_{\sin}\right) + j\alpha\right]e^{-j\theta} + \left[B_{\cos} + jB_{\sin}\right] + Ge^{j\theta} \ , \tag{5.21}$$

where G is the amplitude of ideal resolver output. Assuming that the values of

$\left(A_{\cos}-A_{\sin}\right)$, α, $B_{\cos}$ and $B_{\sin}$ are so small that the squared and product terms of the errors are negligible, the absolute squared of the complex expression, $\overline{z}\left(\theta\right)$ can be estimated by

$$\left|\overline{z}\left(\theta\right)\right|^2 \approx G^2 + 2G\left[B_{\cos}\cos\left(\theta\right)+B_{\sin}\sin\left(\theta\right)+\left(A_{\cos}-A_{\sin}\right)\cos\left(2\theta\right)+\alpha\sin\left(2\theta\right)\right]. \tag{5.22}$$

5.6 Online error compensation method developed in the research

In my research, a new online error compensation method was developed. This adopts the same correction approach as in the initial calibration method. The compensation is achieved by correcting the demodulated non-ideal resolver signals as described in (5.4). Therefore, it requires the same calibration parameters: $A_{\sin}$, $A_{\cos}$, $B_{\sin}$, $B_{\cos}$ and α. However the parameters estimation approach in initial calibration method is not suitable for online application because it is computationally expensive and requires modifications.

The simple and efficient approach to estimate the calibration parameters can be developed analysing the absolute squared complex expression of the non-ideal resolver outputs given by (5.22). This approach has already been reported in [42]. The proposed compensation method is an extension of the work in [42]. Without this extended work, the original approach may not work when amplitude parameters vary from their original values.

The parameters to be used in the online compensation method can be derived by expressing (5.22) in an alternative form:

$$\left|\bar{z}(\theta)\right|^2 - G^2 \approx 2G\left[B_{\cos}\cos(\theta) + B_{\sin}\sin(\theta) + (A_{\cos} - A_{\sin})\cos(2\theta) + \alpha\sin(2\theta)\right] \tag{5.23}$$

The right side of (5.23) resembles a Fourier series expansion with first and second order harmonics. Without losing generality, the term $2G$ is absorbed in the parameters to be determined: $B_{\cos}$, $B_{\sin}$, $(A_{\cos} - A_{\sin})$ and α . These parameters are in fact Fourier coefficients and they can be obtained by using the orthogonality property of the Fourier series. Therefore, the parameters can be found by taking the respective integrals. For example, $B_{\cos}$ can be obtained by the following integral,

$$B_{\cos} = \frac{1}{\pi}\int_0^{2\pi}\left(\left|\bar{z}(\theta)\right|^2 - G^2\right)\cos\theta d\theta \ . \tag{5.24}$$

In digital implementation, this would be similar to summation of the products over the period of one cycle of revolution. This is inconvenient for the online compensation since it has to wait for one cycle period and the computation is inefficient. Therefore, the approach of using feedback loop with integral controllers in place of integration is introduced in [42]. Since the actual values of the changed calibration parameters cannot be determined at the exact time interval, the integration time constant would be large to process sufficient number of periods. However this is not a problem because the proposed compensation method is intended to correct the slow drift effects of calibration parameters. The block diagram showing the online compensation approach with the integral loops [42] is provided in Figure 5.10 .

However, among the coefficients expressed in (5.23), the amplitude difference cannot be directly used in the error compensation. The amplitude of one of the demodulated resolver outputs is needed to make correction according to (5.4) which is illustrated in Figure 5.11. To fulfil this requirement, sinusoidal amplitude tracking to estimate the amplitude is proposed to integrate the existing compensation scheme shown in

Figure 5.10. The tracking technique employs the method of extraction of non-stationary sinusoids [54]. For a given general time varying sinusoidal signal,

$$z(t) = A(t)\sin\left(\theta(t)\right) , \tag{5.25}$$

the estimated amplitude derivative using a gradient algorithm to minimize the instantaneous squared error can be given by

$$\frac{d\hat{A}(t)}{dt} = \mu e(t)\sin\hat{\theta}(t) , \tag{5.26}$$

where $e(t) = z(t) - \hat{z}(t)$ and μ is the gain. The online compensation scheme with proposed modification is shown in Figure 5.12.

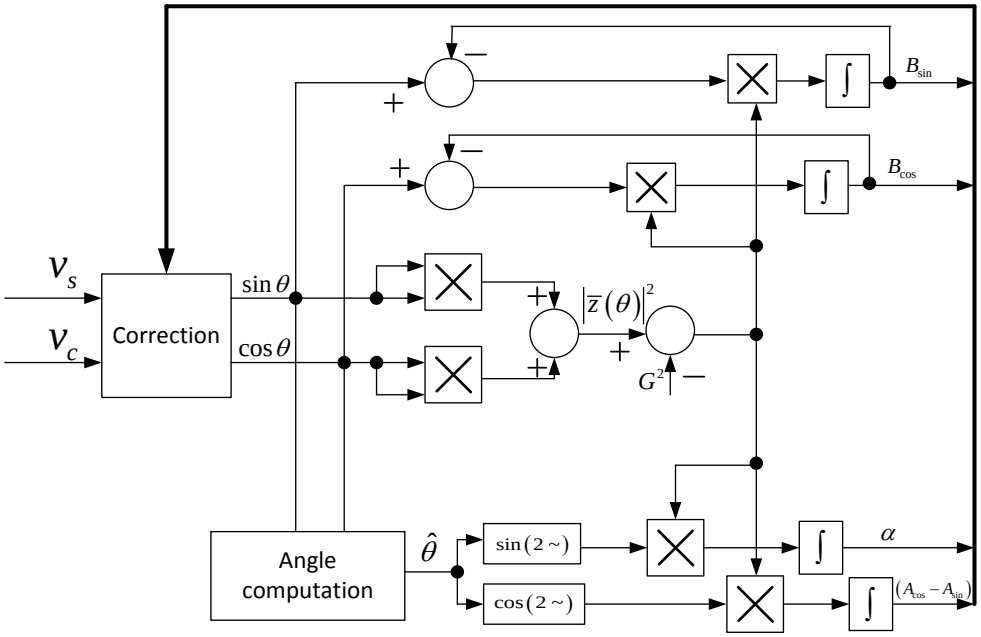

Figure 5.10. Online compensation block diagram

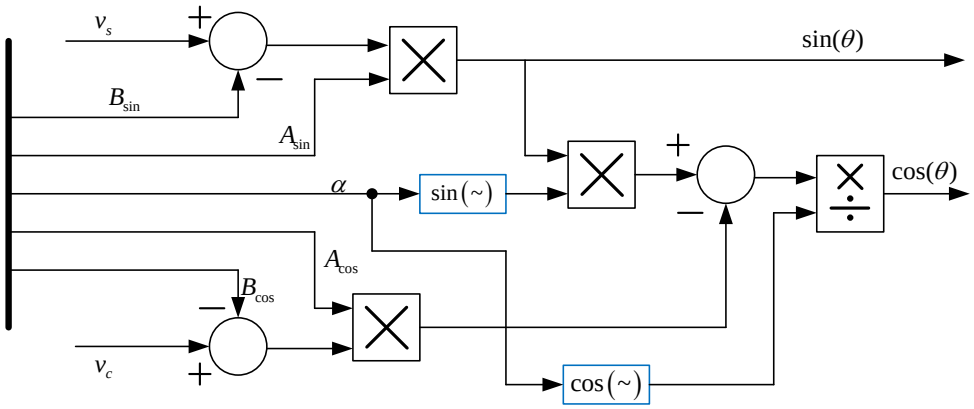

Figure 5.11. Correction block diagram

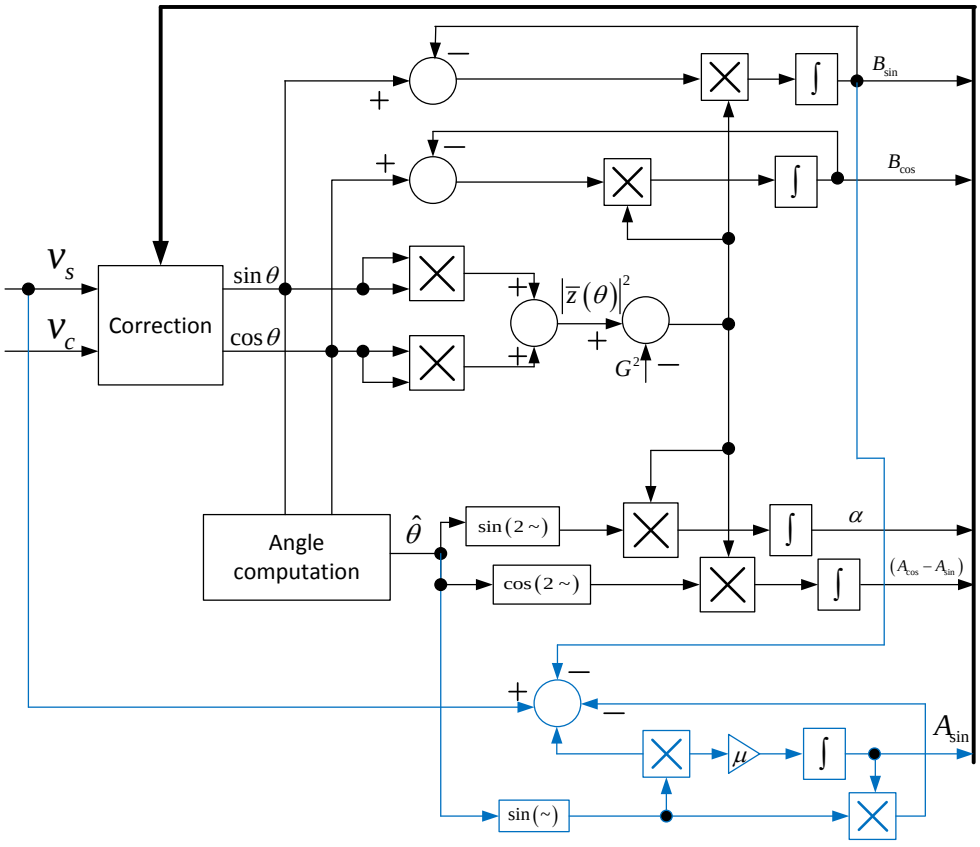

Figure 5.12. Proposed online error compensation block diagram

5.7 Simulation results

Simulation is carried out on MATLAB SIMULINK platform to verify the effectiveness of the proposed online error compensation method. The simulation model for resolver is based on (5.2) and the error compensation is constructed following the block diagram shown in Figure 5.12. The angle computation is performed by inverse tangent method. The simulation results based on the parameters: A_{sin} = 1.05, A_{cos} = 0.99, B_{sin} = 0.02, B_{cos} = -0.03, α = 0.04 and rotor frequency, ω_r = 100π rad/s (3000 rpm), is shown in Figure 5.13. It is evident that the proposed online error compensation scheme can accurately estimate the error parameters and hence the position error is minimized yielding the accuracy improvement in computing the position angle as shown in Figure 5.14.

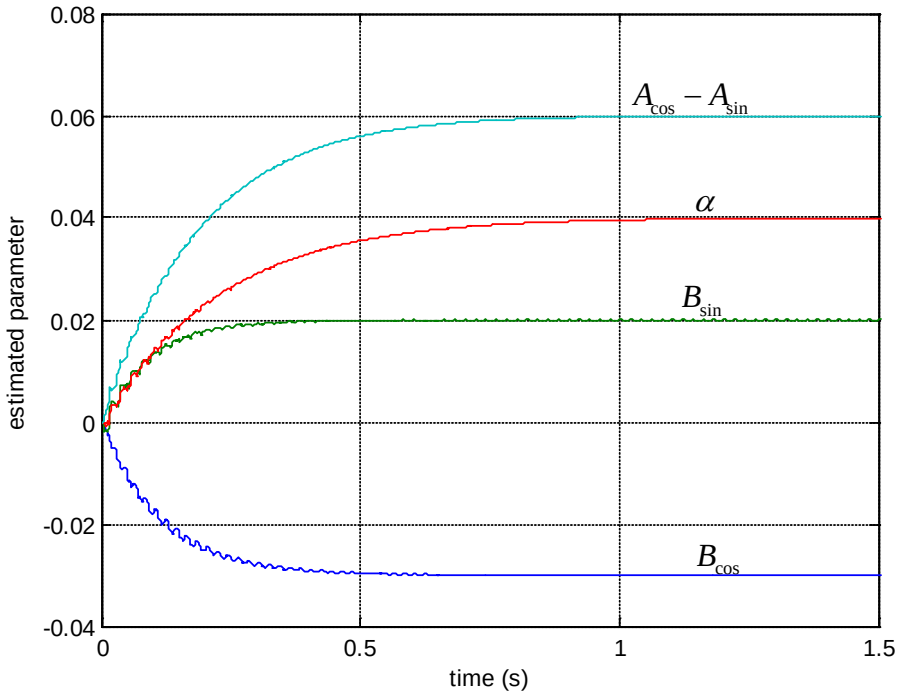

Figure 5.13. Simulation results from the proposed compensation scheme

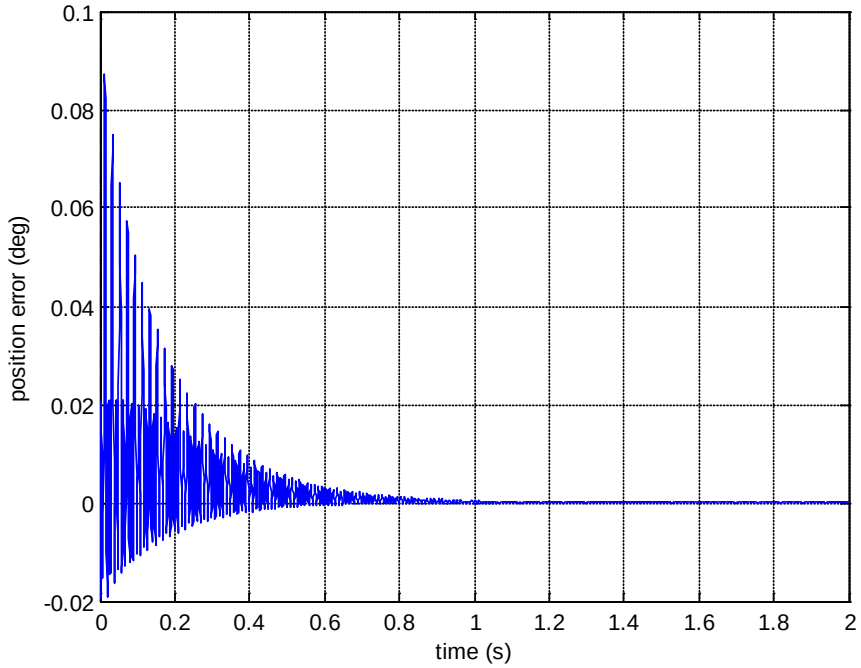

Figure 5.14. Position error with proposed compensation scheme

5.8 Experiment results

The validity of the proposed method is further verified using the acquired data from the experiments carried out in Chapter 4. Because the same resolver is used for verifying the proposed demodulation method, the validation process can directly use the demodulated outputs obtained from the proposed method. There are two sets of experimental data; one is for the shaft at the speed of 300 rpm and the other is at the speed of 4200 rpm. The verification is carried out on MATLAB SIMULINK platform by loading the demodulated data from the workspace instead of using predefined simulation parameters. And the same SIMULINK model built for simulation is used for verification. The additional step here is that the demodulated signals are normalized before feeding them into correction blocks. Normalization is performed by dividing the signals with the absolute peak value of the cosine channel at the position where cosine channel is at its maximum coupling position.

By doing so, the demodulated resolver outputs extracted from the experimental data are available and the objective is to determine the calibration parameters with the proposed online calibration approach.

The results of estimating the calibration parameters from experimental data are shown in Figures 5.15 ~ 5.16. It can be seen that calibration parameters reach to their respective steady state values after some periods depending on the rotor speed. For the low speed operation, large integration time constant and high sampling rate cause ripples in parameters in steady state condition. When the speed becomes higher, this effect is less pronounced. This suggests that compensation process should start only when the operating speed is reached so that the tuned integration time constants will produce the stable calibration parameters. Comparison with the calibration parameters from the initial calibration is provided in Table 8. It is observed that there are changes in parameters compared to the initial values.

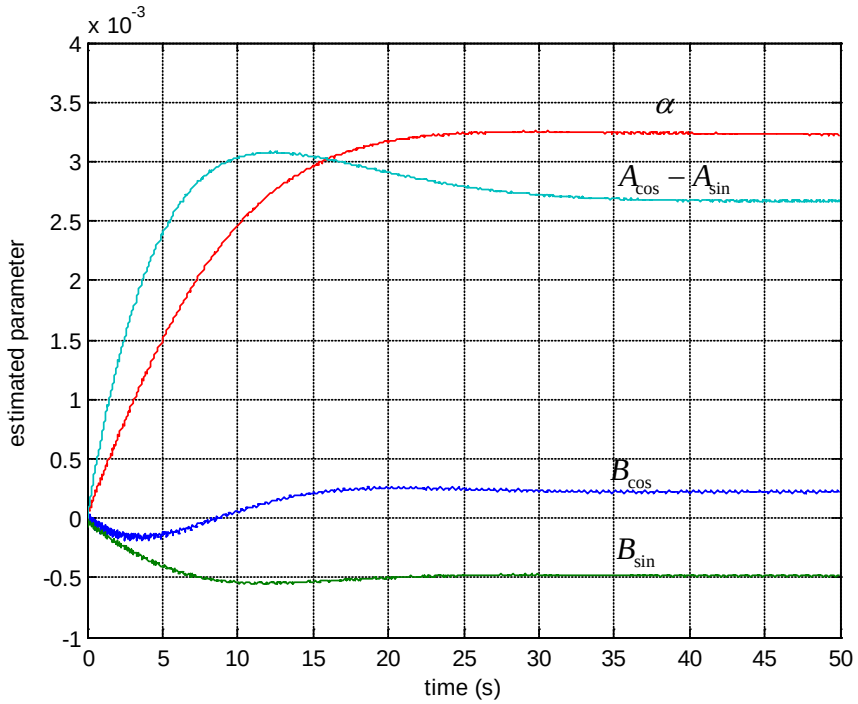

Figure 5.15. Online calibration parameters estimation at the speed of 300 rpm

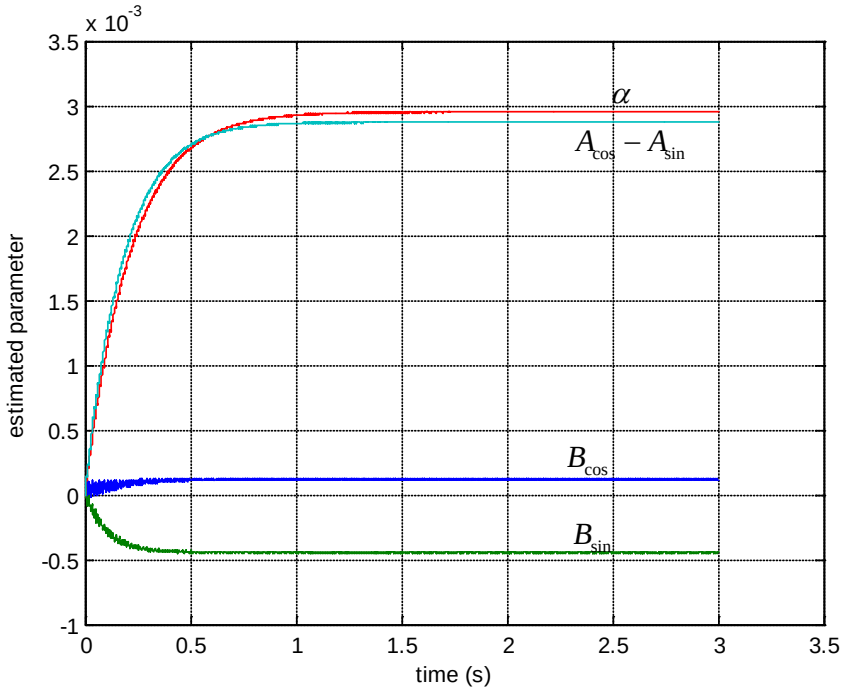

Figure 5.16. Online calibration parameters estimation at the speed of 4200 rpm

Table 8. Comparison of calibration parameters for compensation

	A_{cos}-A_{sin}	α (arc-min)	B_{cos}(mV)	B_{sin}(mV)
Initial calibration	0.09%	17.5	0.09	0.013
Online compensation (at 300 rpm) [average values]	0.26%	11.12	0.21	0.48
Online compensation (at 4200 rpm)	0.28%	10.14	0.12	0.45

The changes in parameters could be due to slight different assembly and different experimental setups. For the initial calibration experimental setup, the whole assembly is done as one complete unit. However, the experimental setup for on-line

calibration requires a different mechanical interface to integrate the same resolver with existing equipment, the spin-stand. Hence, the coupling and alignment in the two setups cannot be identical. On the other hand the operating modes for two setups are also different; one setup is for the stationary mode and the other is for the rotating mode. In initial calibration experimental setup, the coupling of the resolver and rotation stage cannot affect the operation as the data acquisition is done at the stationary positions. While in the experimental setup with the Spin-stand, the coupling can affect the operation with the rotor is in motion. These could result in slight change of electromagnetic couplings and calibration parameters. However, with the same experimental setup, the different speeds have no significant impact on parameters and they yield the similar results.

5.9 Conclusion

This chapter presents our research results of an efficient and time saving method of initial calibration procedure for resolvers with three common systematic errors. The method is mainly based on LLSE approach to identify the calibration parameters. Before LLSE approach is employed, the amplitudes of the resolver outputs are determined by DFT. Once the amplitudes are known, the calibration parameters identification in the proposed method is the same as the sinusoidal parameters estimation with known frequency. The non-ideal demodulated resolver signals are then to be corrected with the obtained calibration parameters before angle computation. The functionality and performance of the proposed technique is verified with simulations as well as with the experimental data.

Based on the compensation approach of initial calibration, the online error compensation method is proposed provided that there are slow drifts in calibrated parameters. In order to suit with the online approach, the distorted signals are modelled in complex Fourier domain and then the calibration parameters can be

estimated as Fourier coefficients. Tracking the calibration parameters are performed in the feedback loops with integral controllers and the initial values for the controllers can be set using the values from initial calibration. The proposed online error compensation scheme can track the change in parameters and hence calibration parameters are updated adaptively. The simulation and experiment results have proved the effectiveness of the proposed scheme.

6 Synthesis of a new type of linear resolver

6.1 Introduction

The accuracy of a resolver depends on its operational principle, working environments, and the precise construction of the magnetic core and windings. Among them, the errors introduced by working environments cannot be controlled. But the errors introduced by the other factors could be minimized in various ways. The reference phase shift and the nonlinear outputs of the resolver are related to the operational principle. On the other hand, the precise construction of the electromagnetic parts is required so that

1. mutual inductance between the primary and the secondary excitation windings must be constant to all rotor positions;

2. mutual inductance between the sensor primary winding and the sensor secondary winding (two orthogonal output windings) must have a required relationship with respect to rotor position; and

3. the secondary sensor windings must be orthogonal in electromagnetic field to each other. This is necessary to avoid the influence of the output windings to each other.

These requirements with wound windings and the cascaded two different structures make the conventional brushless resolvers expensive due to labour intensive work in making and assembling the precise windings, stator and rotor cores, and low production yield.

For a normal resolver, its output signals are sinusoidal function of rotor position, and the research around this kind of resolver has been done many years. However, even for this kind of resolver, one of the challenging problems is the inductance harmonics due to non-ideal sinusoidal winding distribution. In order to minimize the

harmonics, for the linear resolver introduced in section 1.47, an additional windings and skewed slots are employed. These also attribute to the higher cost in production. When considering linear resolvers, another restriction is that they can only operate in ±60°. If the output of the resolver is required to be the other functions of rotor position with high accuracy, it can be imagined that the stator core and winding structure will be more complicated, and may even be unrealizable in mass production. In order to reduce the size of those resolvers and simplify the manufacturing process that can make resolvers inexpensive, it demands the exploration in alternative designs. In addition to these issues mentioned, another major concern to the linear resolver introduced in 1.47 is that, its rotor windings must be connected with stator winding. This connection may impose limitation to many applications.

Variable Reluctance (VR) resolvers have been playing an important role in brushless resolvers for many years to reduce both size and cost. VR resolvers are comparatively easy to be manufactured because they don't require the separate excitation transformer and they don't have winding on the rotor. However, sinusoidal winding distribution is still restricted by the stator slots and inductance harmonics are observed in these resolvers. The outputs of VR resolvers are the same as those of conventional brushless resolvers and they are nonlinear.

The nonlinearity of the resolver outputs has an effect on the resolution of the angular position and this requires further computational works to retrieve the position angle. The most affected intervals in the demodulated resolver outputs are around their maximums. Since the two signals are orthogonal, when one is at the maximum the other is at the minimum. While the signal at maximum position is at its high nonlinear region, the other signal is at its minimum where it can easily be affected by noise. Therefore, even though position angle is changed to a significant value, the changes in the demodulated outputs may not be reflected correctly. Since the sensitivity at these quadrature positions are very low, the resolution as well as the

accuracy are expected to be low. Linearization of the two sinusoidal signals is therefore applied to improve accuracy and to reduce the computational load [58].

The Printed Circuit Board (PCB) technology has been widely used in electronic systems, and even as the armature windings in electrical machines. There is however a relatively few patents that introduce the potential of using PCB technology in resolver [59-60]. For low profile structures with axial type machines, PCB windings are always of interest. When the slot-less designs are considered, the PCB windings are much more flexible compared to the common wire wound windings. Actually, it can realize any 2D winding patterns which can be generated by PC software (If the dimensions of line interval, width and connection holes comply with PCB production capability). For the mass production, PCB windings can be cost effective due to its simplicity in design and hence, the assembly process would be more straightforward. Using the multilayer PCB, several windings with different winding pattern can even be realized in one board. As PCB technology is developing very fast [62], for the resolver whose windings are formed by PCB technology should possess better and better performance in future. This motivates the consideration of synthesis of a PCB resolver with an axial EM field structure. This chapter presents the detailed synthesis of our research on an axial EM field absolute brushless resolver with PCB winding structure.

6.2 Design approach of the new type of resolver

The new resolver adopts the same working principle of a conventional brushless resolver. Therefore it comprises two transformers cascaded in series and the design procedure involves two areas: the design of the excitation transformer and the design of the sensing transformer or sensor. As the flexibility in the winding pattern design and making, we decided to use PCB technology to realize the resolver windings. As PCB can only form the 2D winding, the resolver EM structure should be an axial

field one. The new type of resolver utilizing the PCB windings will be called “PCB resolver” for short.

In the design process of a general power transformer, the usual design objective is to achieve the optimal efficiency. Therefore, it is based on finding the optimal EM structure that will minimize both winding loss and copper loss.

However, resolver is not used for power or voltage conversion. The design objectives of a resolver are of two folds: one is to obtain the output signals that have minimal systematic errors and the other is to achieve the high transformation ratio. To achieve the first objective is the main focus in this work. By doing so, the simplicity in structure is paid special attention so that it could reduce the cost. The quality of output signals is determined by how the flux links from sensor primary to secondary winding. The transformation ratio depends on the EM structure, number of winding turns and the operating frequency. Operating flux density is one of the key design parameters in resolver construction. It must be ensured that the operating point of the resolver lies in the linear region of the B-H curve of the core material.

Unlike a power transformer, the design of a resolver needs to consider two transformers with different functions at the same time. The arrangement of the two transformers can result in different design approaches. For a traditional brushless resolver, a decoupled design approach can be used since one transformer operation does not affect the other. The excitation transformer can be designed following the design procedures of rotational transformer and the sensing transformer can be designed as rotational inductor. How to avoid the interaction of the fields of these two transformers is very challenging in the design.

In order to design the resolver, the core structure and general winding arrangements of two transformers needs to be first determined. After that, it is to select the proper core material of the resolver and to determine the detailed

parameters for the winding layout of both excitation transformer and sensing transformer.

6.3 Core structure and windings arrangement of the PCB resolver

As it was introduced, for a resolver with PCB winnings, the axial field winding arrangement is usually a common choice. The core structure of the resolver in this case will be the same as that of a pot core rotational transformer. Then the two types of winding arrangement can be considered as shown in Figure 6.1. The first winding arrangement follows that of a conventional brushless resolver, but windings are displaced in radial direction. The other is axially distributed type which is similar to the winding arrangement in stator of VR resolver where the sensing winding is stacked over the excitation winding.

Since the flux linkage or magneto-motive force distribution is directly related to the area defined by the winding, it requires a reasonable number of winding turns. This implies that the winding structure distributed axially will result in a more compact structure. However, this arrangement could introduce a constant magnetic field coupling from excitation winding to sensing winding. The details of this flux linkage effect need to be investigated in calculation of mutual inductance of the windings.

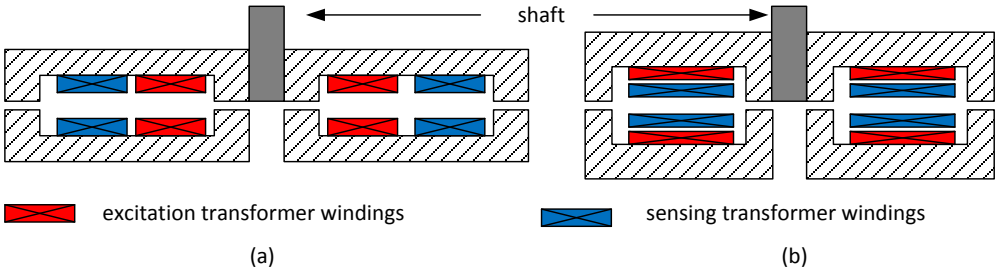

Figure 6.1. Two different winding arrangements

In this research, the second type of winding arrangement is adopted to yield a compact resolver structure similar to that of a variable resolver, where both excitation and sensing windings share the same core. Core size is defined as one of the design constraints as the resolver will be built using the available core material from the laboratory. Therefore, it should be noted that the optimal core size is not taken into account in the synthesis of the PCB resolver.

6.4 Equivalent circuit of PCB resolver

The equivalent circuit of the PCB resolver is shown in Figure 6.2, where, the subscript ‘e’ means the exciting winding of the transformer, ‘sp’ means the primary side of the sensor winding, ‘ss’ means the secondary side of the sinusoidal sensor winding, and ‘sc’ means the secondary side of the cosine sensor winding. The circuit parameter $Z_{e\sigma 1}$ means the impedance of the primary exciting winding induced by the leakage field and winding resistance, R_{em1} represents the iron loss induced by the exciting current of the primary winding, X_{em1} means the exciting inductance of the primary winding, $Z_{e\sigma 2}$ means the impedance of the secondary exciting winding induced by the leakage field and winding resistance, R_{em2} represents the iron loss induced by the current of the secondary exciting winding, X_{em2} means the exciting inductance of the secondary winding, $Z_{sp\sigma}$ means the impedance of the sensor winding induced by the leakage field and winding resistance, R_{spm} represents the iron

loss induced by the current of the primary sensor exciting winding, X_{spm} means the exciting inductance of the sensor primary winding, $Z_{ss\sigma}$ means the impedance of the sinusoidal sensor winding induced by the leakage field and winding resistance, R_{ssm} represents the iron loss induced by the current of the sinusoidal sensor exciting winding, X_{ssm} means the exciting inductance of the sinusoidal sensor winding, $Z_{sc\sigma}$ means the impedance of the cosine sensor winding induced by the leakage field and winding resistance, R_{scm} represents the iron loss induced by the current of the cosine sensor exciting winding, X_{scm} means the exciting inductance of the cosine sensor winding.

In the design, the primary exciting winding and secondary sensor windings are located on the stator PCB; the secondary exciting winding and the primary sensor winding are located on the rotor PCB; see Figure 6.2.

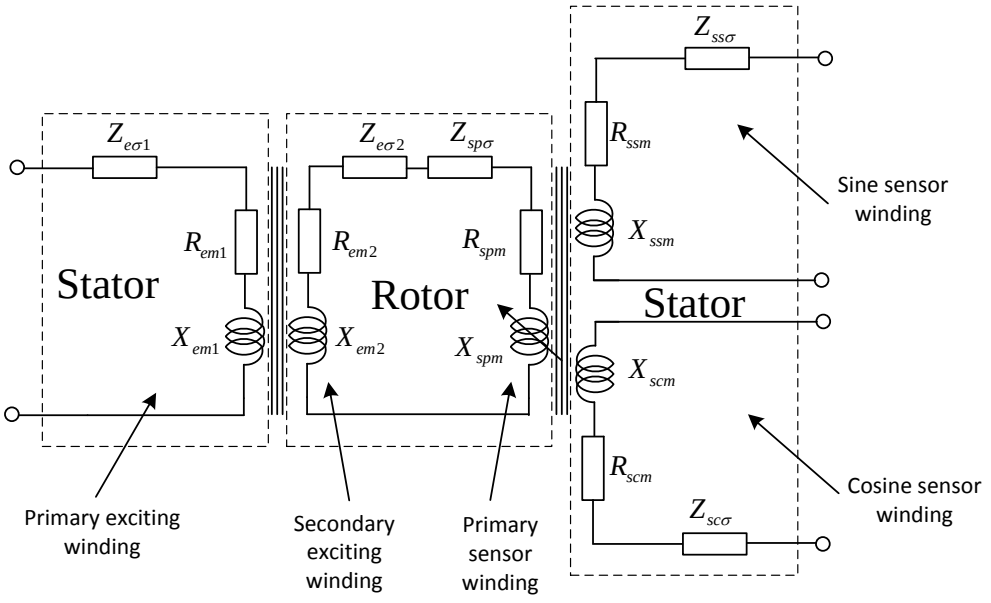

Figure 6.2. Equivalent circuit of 2-phase resolver

6.5 Core material

For realizing a compact resolver structure and shielding the resolver from external fields, the core of resolver should be made from ferromagnetic materials. However, for this kind of material, losses happen in alternating field application. The losses can be categorised as hysteresis loss and eddy current loss. The former is generated by the hysteresis characteristic of the material, and the latter is generated by the eddy current induced by the alternating field in the material [63]. The core loss is a factor to be considered in resolver design as the operating frequency of the excitation signal in a resolver is quite high. For an axial field oriented resolver like the flat PCB resolver, if the laminated steel sheets are to be used to reduce the core loss, this would require a single thin laminated steel sheet which is rolled in a spiral form. In addition, if the slots are to be formed, this would require more cost in manufacturing because punching the steel roll is not as simple as punching the stacked laminated sheets.

In our research, soft magnetic composite (SMC) material is found to be interesting to replace the laminated steel. SMC is an isotropic material consisting of small insulating iron particles. Because of this property, it can be shaped into any 3D design using cost effective compaction process [57]. Compared to the laminated steel, eddy current losses in SMC are significantly lower due to the smaller size of the particles. On the other hand, SMCs have lower permeability due to distributed air-gap among particles and they have higher hysteresis losses because of the plastic deformation of the particles that takes during the compaction step. However, due to the continuous effort to improve the performance of SMCs, the hysteresis losses are significantly reduced in recent developments [61]. Because of this, the SMCs are finding more and more applications in low and mid frequency operated electrical devices.

Considering the axial structure of the PCB resolver, and minimization of cost and losses, the PCB resolver core is constructed using the SMC material, Somaloy 700 3P and its B-H curve is shown in Figure 6.3. The core size is specified based on available SMC material in the laboratory and winding parameters.

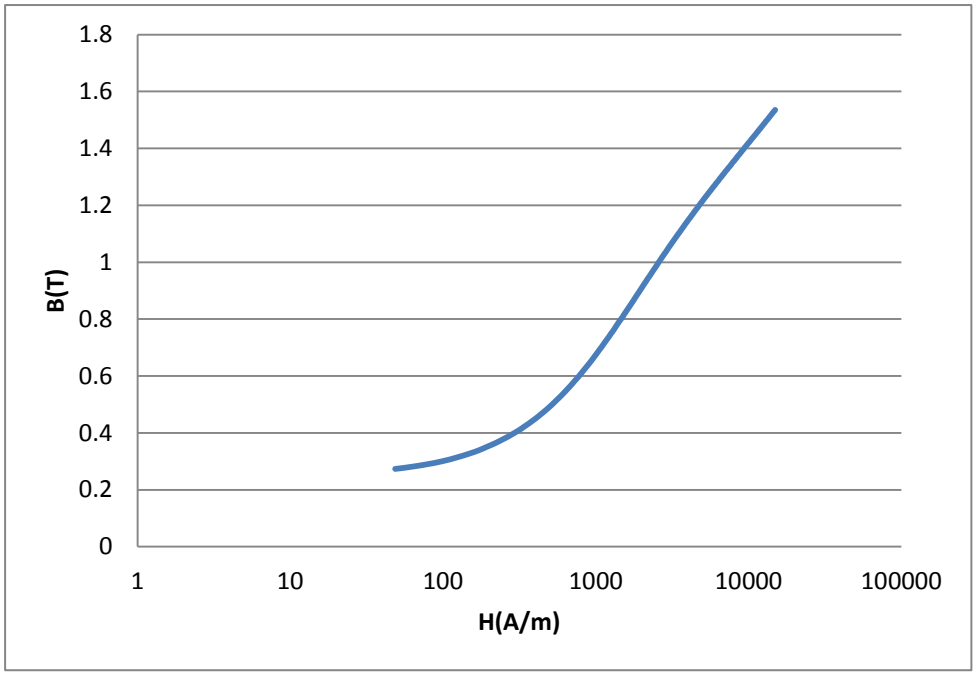

Figure 6.3. B-H curve of Somaloy 700 3P

6.6 Excitation transformer

After selecting the core material, it is to synthesize the excitation transformer which takes the structure of a flat planar rotary transformer. In both primary and secondary sides of the transformer, the windings are to be wound in a spiral form. Each winding occupies two layers which are connected through a via hole. In each layer, the winding is wound in the same direction. This makes the resulting magnetic fields additive and produces the stronger field. The first layer starts from its inner radius and grows outwards to its outermost radius. It is then continued to the second layer where the winding turns shrink towards its innermost radius. Each track in both

layers is aligned axially to ensure the maximum coupling of flux linkages. The concept of winding patterns is shown in Figure 6.4. This kind of arrangement can yield the mutual inductance between the primary winding on stator and secondary winding on rotor, which varies very little for different rotor position. The mutual inductance can thus be considered to be independent to the rotor position. Therefore, when the excitation voltage on the terminals of the primary winding is constant, the electromotive force (emf) induced on the secondary winding is constant, i.e., the emf does not change while the rotor is rotating.

Both primary and secondary excitation windings are allocated close to their respective core so that the field produced by the current in the winding is enhanced by high permeability property of the core.

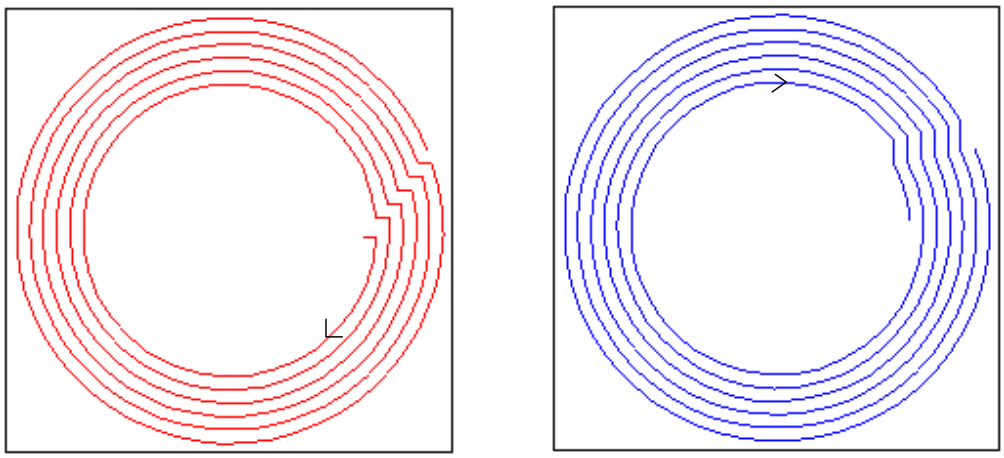

Figure 6.4. Concept of excitation transformer primary winding

As the $e_{e2}(t)$, back-emf of the secondary winding, is determined by

$$e_{e2}(t) = M_{21}\frac{di_1}{dt} = k_{21}w_2w_1\frac{di_1}{dt} \quad . \tag{6.1}$$

where M_{21} is the mutual inductance between the primary and secondary windings, k_{21} is the coupling coefficient, and w_1 , w_2 are the effective winding turns of the primary and secondary side, respectively.

From above description, for the exciting windings, one fundamental requirement is that, k_{21} must be independent to the rotor position, i.e., it must be constant when the secondary of the resolver locates at different angle positions, From Figure 6.4, it can be known that, increasing the winding turn density is helpful to reduce the variation of the coupling coefficient. Therefore, in the PCB design, winding turn density should be designed as high as possible. In our prototype, the line interval of the PCB is 0.1mm, and line width is also 0.1mm. This is the limitation of the PCB supplier in the winding turn density.

6.6.1 Parameters of the excitation transformer winding

The following winding parameters are required to be determined in the design process of the excitation transformer: 1. PCB track thickness and track width, 2. Spacing between PCB tracks, and 3. Inner radius and outer radius. The turn ratio is specified to be 1:1 and both primary and secondary have the same winding parameters.

PCB track thickness and track width

The maximum current in resolver winding is restricted to be 200 mA and the thickness of the track is set to be 1.0mil. Based on IPC-221 [66], the required trace width is found to be 0.117mm. Considering the higher safe limit, the trace width is specified to be 0.2 mm.

Spacing between PCB tracks

According to IPC-9592 [67] for power conversion circuits, the recommended spacing for the operating peak voltage of less than 15V is 0.13mm. The resolver exciting voltage intended to supply is in the range of 5V to 10V. Therefore, 0.1mm is chosen as the spacing between PCB tracks. This spacing is applied to all interlayers as well.

Inner radius and outer radius

By specifying the inner diameter of PCB to be 26.4mm, two-layer winding with each layer having 80 PCB tracks are specified to form the winding. The excitation transformer parameters are listed in Table 9.

Table 9. Geometrical parameters of the resolver: excitation transformer

No. of primary/secondary turns	**80/80**
Spacing between tracks [mm]	0.1
Track width [mm]	0.2
Track thickness [mil]	1
Outer diameter [mm]	75
Inner diameter [mm]	26.4
Separation between layers [mm]	0.1
Air gap length [mm]	0.4

6.7 Design evaluation of PCB excitation transformer by simulation

The task of the excitation transformer is to deliver the power to the primary winding of the sensing transformer which is located on the rotor. Because of the

rotary transformer structure, there exists air gap in the flux path. These indicate that there can be leakage flux. Therefore, it is estimated that the secondary voltage will be less than the primary impressed voltage. Using the analytical approach, it can be estimated the voltage at the secondary side. However, the more accurate result can be obtained by using the numerical approach, the finite element method (FEM).

In order to investigate the performance of the excitation transformer with the specified parameters, the electromagnetic model of the excitation transformer is built using a commercial finite element analysis package, ANSYS MAXWELL, and the simulations are carried out. Since the excitation transformer windings and core are symmetric around the vertical z-axis, the axisymmetric 2D model is used in the analysis. The distribution of the flux lines and flux density are plotted in Figures 6.5 ~ 6.6. It can be observed that most of the flux is contained in the core and guided by the core structure but there are some fluxes which directly link crossing the large air gap. There exists negligible flux leakage according to the flow of flux lines. The flux density plot shows that the average flux density in the core is around 2mT and this ensures that the device will be operating in the linear range. This indicates that core loss would not significantly affect the performance. The flux density profile in the middle of the air gap is shown in Figure 6.7. It is found that the flux density increases linearly while approaching from outer radius to inner radius.

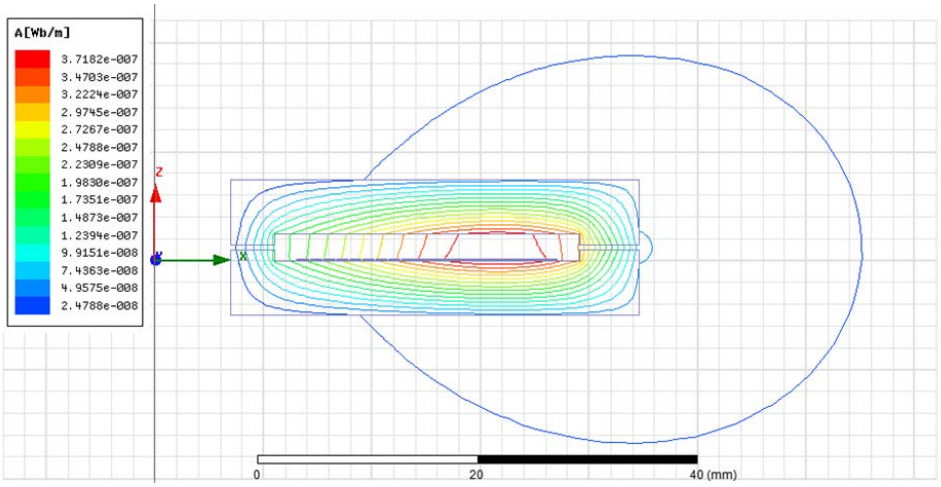

Figure 6.5. Excitation transformer: flux lines distribution

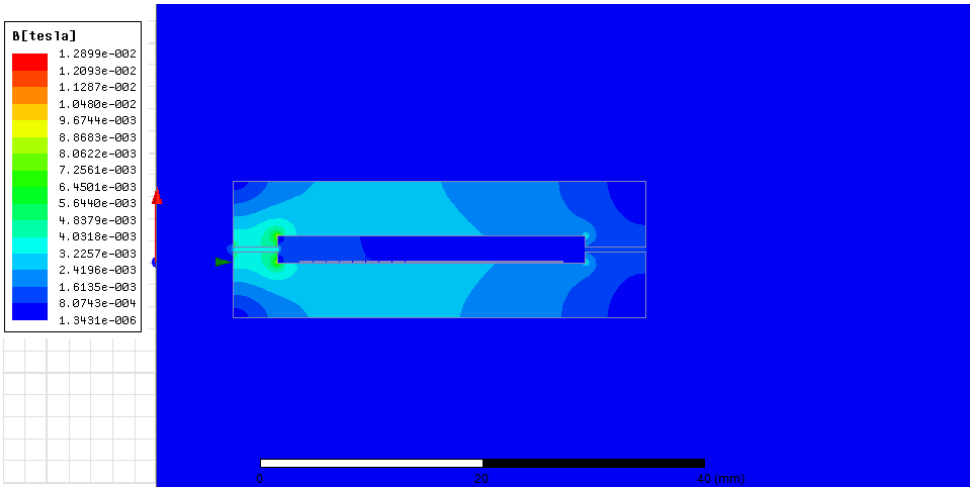

Figure 6.6. Excitation transformer: flux density distribution

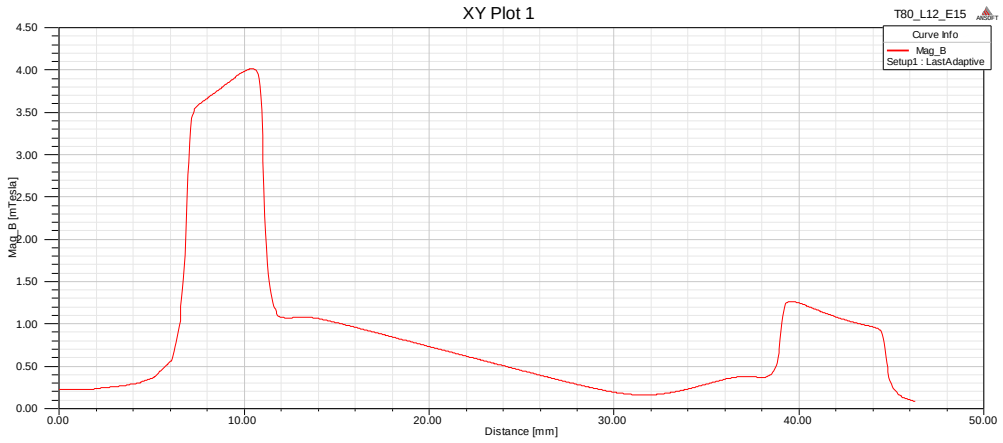

Figure 6.7. Excitation transformer: air gap field distribution

3D finite element analysis is also carried out to have a more comprehensive view of the flux distribution in the whole model. In the analysis, only 40 turns are used to save the computing time. The flux density vector plot is shown in Figure 6.8. It can be observed that the 3D results are in good agreement with 2D results and most of the flux lines link the winding and leakage flux can be considered negligible.

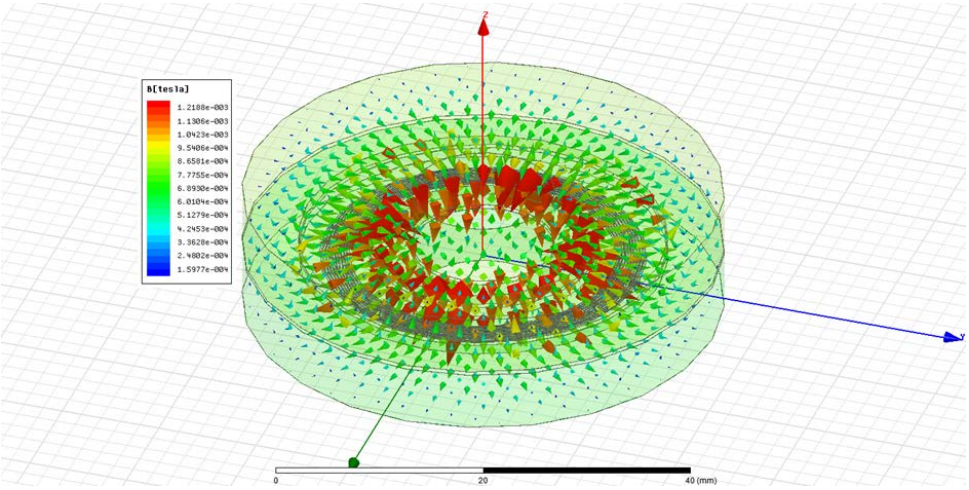

Figure 6.8. Excitation transformer: flux density vectors in 3D

6.8 Sensing transformer

Unlike the excitation transformer, the sensing transformer works as a coupled inductor whose coupling varies with the rotor position. This is due to the fact that the secondary side of the sensing transformer would be connected to the high input impedance signal processing interface and the transformer operates as a secondary open circuited condition. The operation does not transfer power from primary to secondary but the secondary terminal voltage would vary with the changing position of the primary side. Therefore the sensing transformer works as a variable coupled inductor.

If the resolver is to be a nonlinear type like the traditional resolver, there would be two main design objectives for the sensing transformer. First is to achieve sinusoidal mutual inductance variation between primary winding and secondary windings with respect to rotor position and the amplitude of the sinusoids must be same. Second is to achieve the orthogonal relationship between the envelopes of the sensor output voltages.

However, for exploring the unique performance of the PCB resolver, and utilizing the flexibility in the winding pattern design, in our research, the target in designing the resolver was aimed on more complicated one: linear resolver. For a linear resolver, the first design objective is changed to have a linear variation of mutual inductance between primary winding and secondary windings with respect to rotor position. The second objective will be remained unchanged to have the decoupling effect between two secondary windings.

6.8.1 Sensor primary winding

Sensor primary winding is arranged to produce one pole pair of magnetic field. Therefore, winding area is divided equally into two parts for producing different magnetic poles as shown in Figure 6.9 .

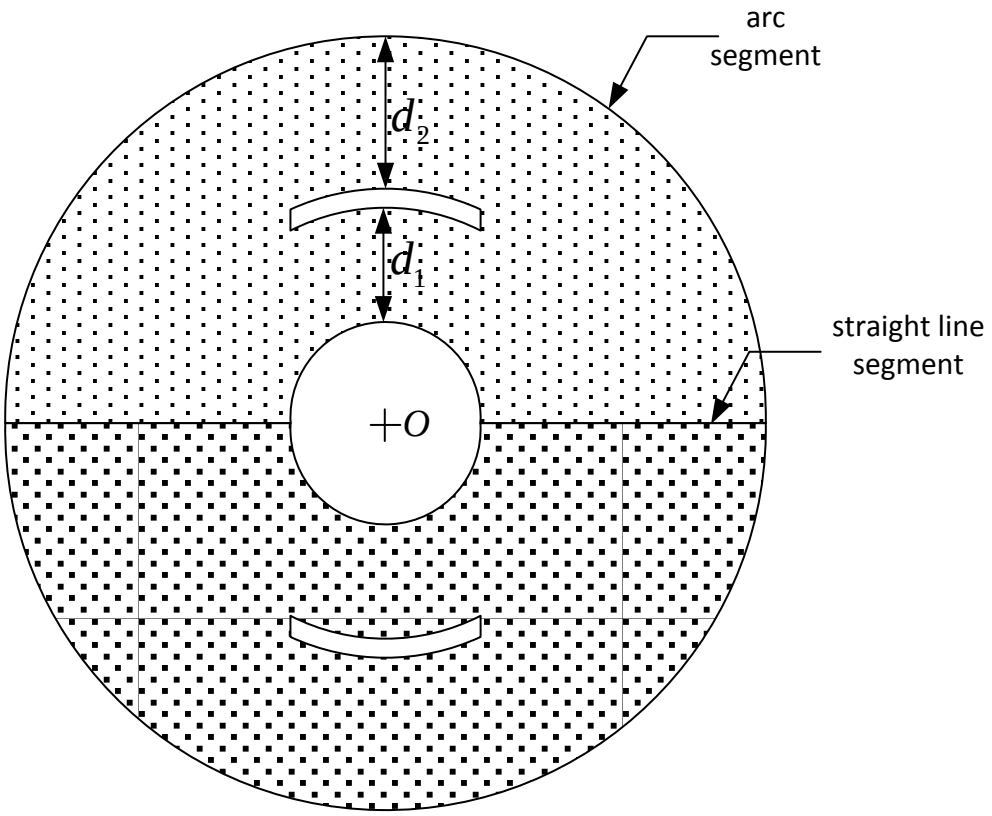

Figure 6.9. Available winding area

The winding direction of one part shall therefore be opposite to the other part. To reinforce the magnetic fields, multilayer structure is considered to compose the rotor winding. Another objective of making a multilayer type is to make the winding balance so that the net field would be symmetric around the air gap.

From Figure 6.9, it can be observed that the maximum number of winding turns is determined by the shorter distance of the two radial measurements, d_1 or d_2. In the design, to utilize the space effectively, and realize high magnetic coupling effect, the line interval should be as small as possible. This implies a constraint; d_1 shall be equal to d_2. With the available winding area and the radial distance constraint, there can be many variations of winding distribution or pattern. How to determine the appropriate winding pattern to obtain the desired flux linkage is crucial in designing the sensor transformer. We restrict our winding patterns to be made up of two types of segment;

1. Arc segments centered at the same origin, and

2. Straight line segments which connect the arc segments.

Even with these restrictions, there are still several winding patterns to investigate. We will investigate several winding distributions later. Regardless of the variations in winding patterns, the winding interconnections among the different winding layers can be fixed. A general winding pattern with arc segments and equal angular spaced radial straight line segments is shown in Figure 6.10 and the interconnection of each layer is shown in Figure 6.11. All the windings are connected directly in the PCB.

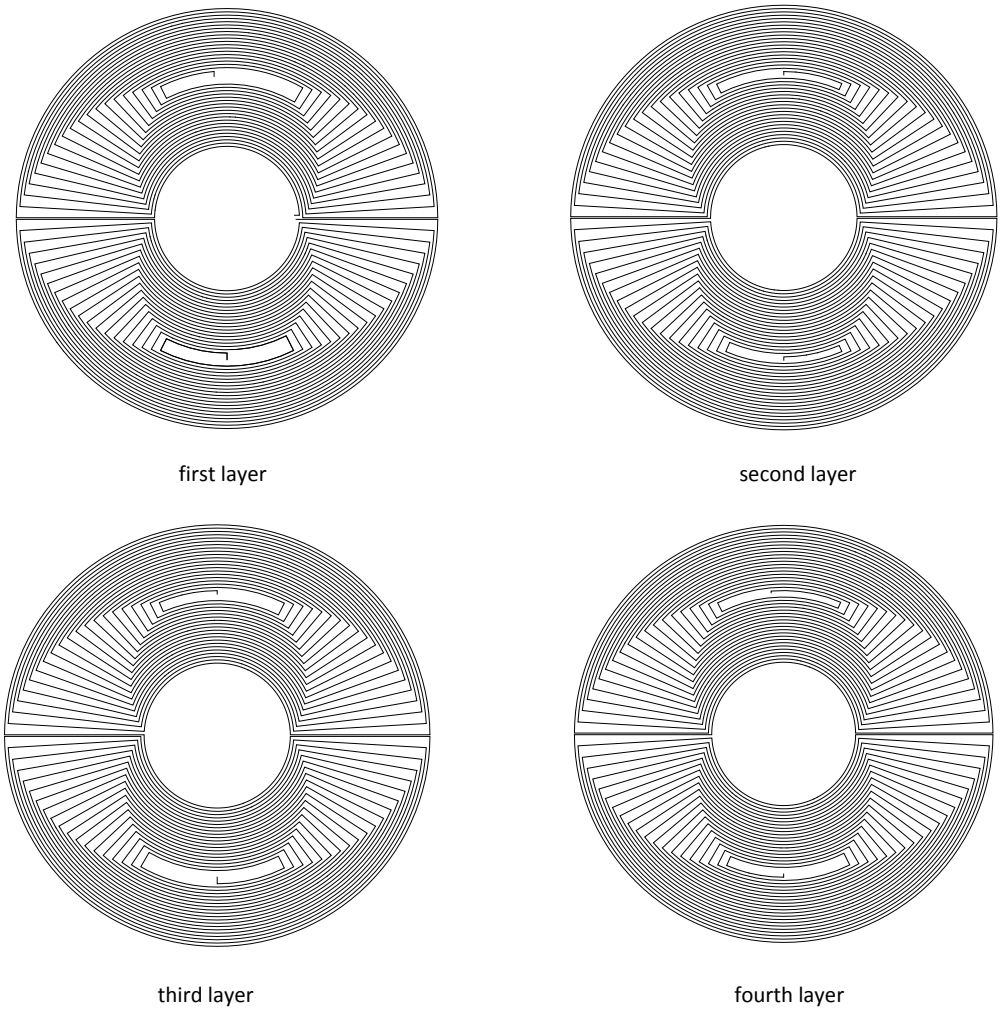

Figure 6.10. General winding distribution of sensor primary winding

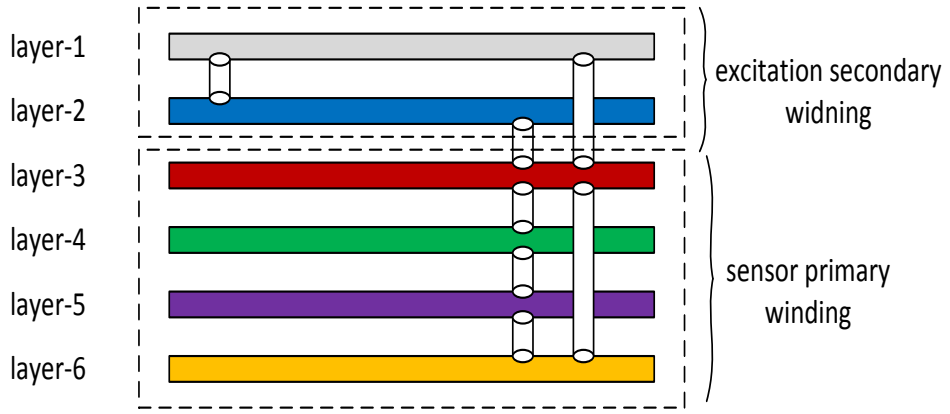

Figure 6.11. Primary side: winding layers interconnection

6.8.2 Sensor secondary winding

Secondary winding of the sensing transformer is to be allocated in the stator of the resolver for realizing brushless linear output. To realize the linear output, together with the sensor primary winding pattern design, after several turns simulation and test, the winding pattern of sensor secondary winding is designed the same as the sensor primary winding. However, a pair of quadrature output is required and there are two sensor secondary windings. To simplify the description of the output windings, it should be noted that the terms of “sine output winding” and “cosine output winding” are continued to use for the linear PCB resolver even though they are designed to produce a linear output with respect to rotor position. Similar to the winding development in the primary winding, each output winding is wound to produce a two pole magnetic field. Since both sine and cosine winding would be made up of two layers, the sensing transformer will have the turn ration of 2:1. Following the same concept in primary winding, each layer supplements the other to produce the stronger magnetic field in the same direction. The two output windings are displaced 90 degrees in space. Special attention has to be paid at the transition of first semicircle to

second semicircle where the winding is wound from inside to outside and vice versa. The general winding layouts are shown in Figures 6.12 ~ 6.13. From the figures, it can be found that the sine and cosine output windings are orthogonal to each other. Therefore, the field produced by current in one winding cannot affect the other. This is the required decoupled field orientation of the resolver windings.

In order to average out the flux linkage from primary to secondary output windings, the cosine winding is sandwiched into the sine winding as shown in Figure 6.14.

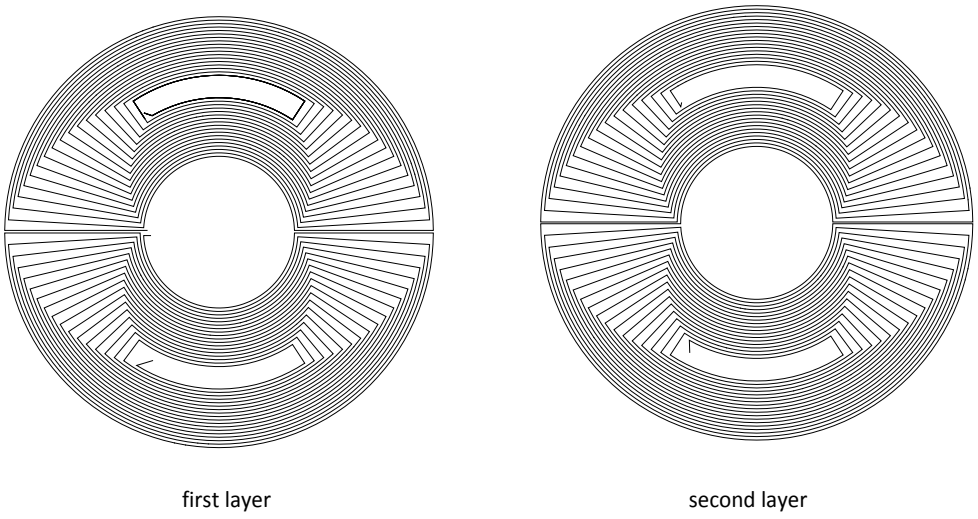

Figure 6.12. Secondary side: sine output winding

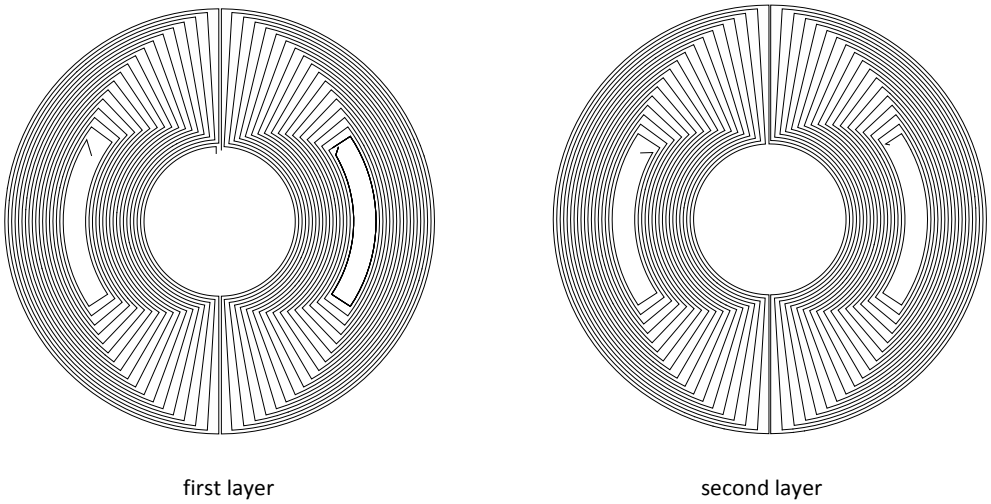

Figure 6.13. Secondary side: cosine output winding

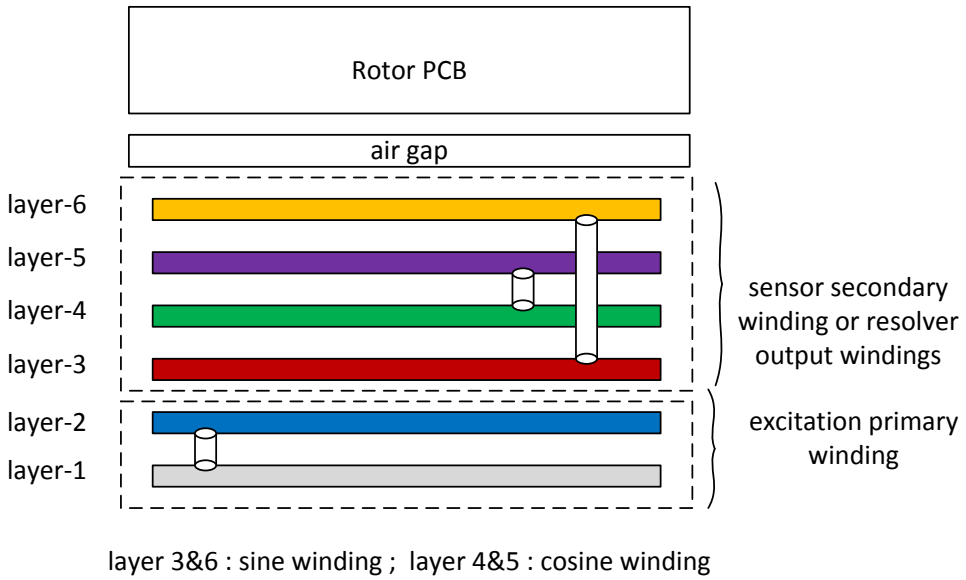

Figure 6.14. Secondary side: winding layers interconnection

6.8.3 Winding distribution of PCB linear resolver

For a conventional brushless resolver, the windings should be distributed to produce a required coupling between the primary and secondary windings of the sensing transformer while the rotor is in motion. However this requirement is

restricted by the slot number and slot shape. Applying PCB winding with slot-less resolver structure gains more freedom in winding distribution. In general, while aiming the size reduction in radial direction, the number of PCB winding turns is restricted in the planar orientation; however it can grow conveniently in the axial direction.

When the resolver output is requested to be different functions of rotor position, for example, sinusoidal or linear, the sensor winding pattern is different. It is clear that PCB winding is more flexible in generating different winding patterns, and PCB resolvers can thus realize more functions than traditional resolvers. For demonstrating the advantage of PCB winding, our research was focused to the PCB linear resolver, i.e., the output of the resolver is a linear function of rotor position. This kind of resolver is difficult to be realized with the traditional resolver structure, especially when the brushless mode and 360 degree operation range are required.

For a traditional brushless resolver having the outputs varying in a sinusoidal function with respect to the rotor position, and it requires that the winding distribution to be sinusoidal. This can be achieved by distributing the different ampere turns in the respective slots to generate a sinusoidal flux density distribution in the air gap. Due to the uniformity of magnetic field distribution along the axis, the field solution can be estimated accurately with a two dimensional analysis approach and the shape of back emf can be predicted. Degrees of freedom mainly involved are slot shape, slot numbers and different number of turns for different slots.

But in axial type electromagnetic structure, the electromagnetic field in air gap is three dimensional and prediction of the shape of back emf is not straightforward. There is no standard procedure in designing the PCB winding distribution to yield a desired induced voltage waveform. In this research, we investigated three types of

winding patterns and selected the most suitable winding pattern for the sensing transformer. The three winding patterns are:

a) Winding pattern I: the winding is illustrated in Figure 6.15(a), which is made up of arc segments and equal angular displaced radial straight line segments. The angle of the innermost radial straight line in the spiral coil determines the spacing angle.

$$\theta = \frac{\pi - \beta}{N} \ , \tag{6.2}$$

where N is the number of PCB tracks and β is the angle of the innermost radial straight line in the spiral coil.

b) Winding pattern II: the winding is illustrated in Figure 6.15(b), which is made up of arc segments and equal linear displaced radial straight line segments. The linear displacement between the successive segments is defined by

$$dy = k \times ts \ , \tag{6.3}$$

where ts is the tracks separation distance and k is the scaling factor which is greater than or equal to one. The angular position of the segment is determined by

$$\theta = \sin^{-1} \frac{dy}{R_{is}} \ , \tag{6.4}$$

where R_{is} is the radius of the inner arc segment connected to the straight line segment. Although winding pattern II is similar to wining pattern I, the angular displacement between adjacent straight line segments in winding pattern II is not equal and it varies in a parabolic form; the angle value is increased at the starting, after the maximum value is passed the

angle value is decreased. This is more pronounced when k becomes larger.

c) Winding pattern III: the winding is illustrated in Figure 6.15(c), which is made up of arc segments and equal linear displaced parallel straight line segments. The linear displacement between the successive segment is obtained from (6.3).

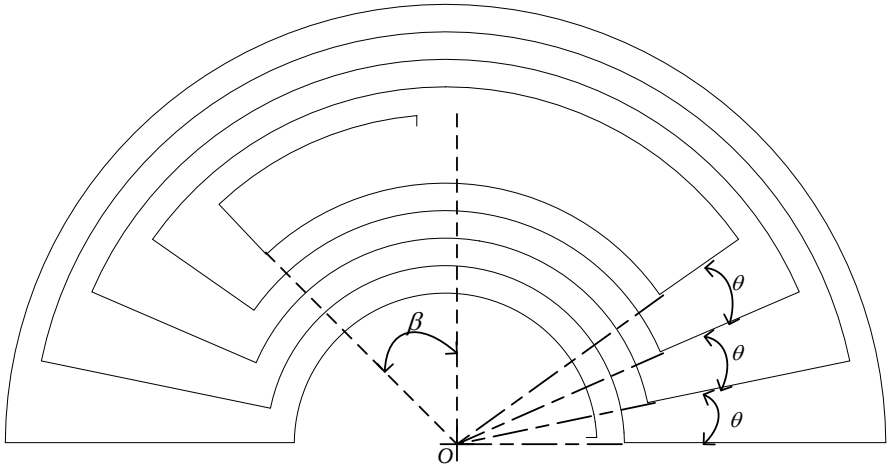

(a) winding pattern I

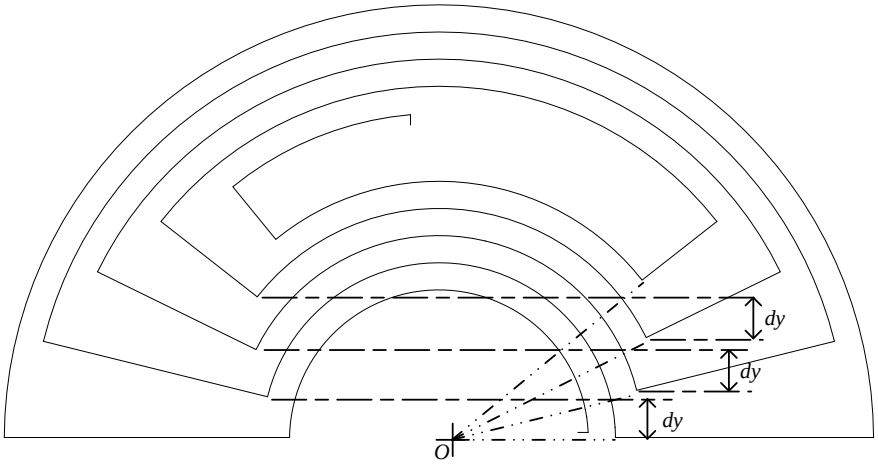

(b) winding pattern II

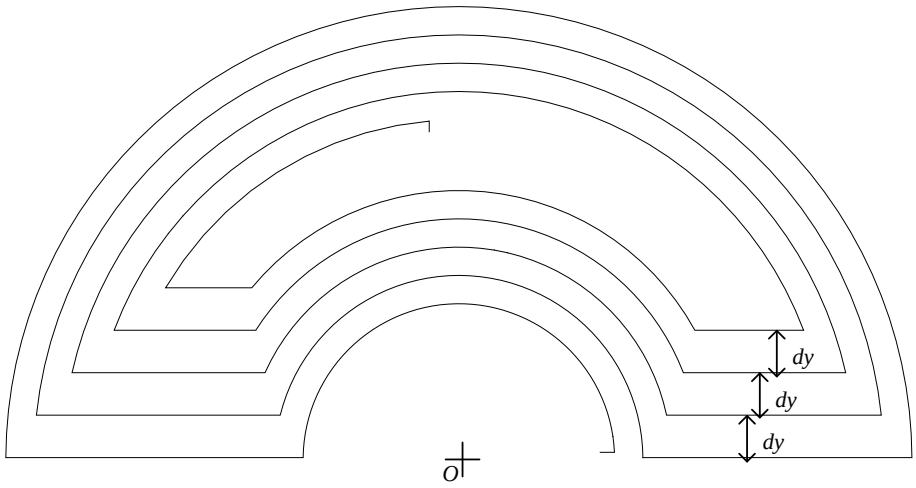

(c) winding pattern III

Figure 6.15. Three winding patterns sensing transformer

The induced voltage in a coil due to the change of magnetic flux can be derived from the flux linkage, which can be expressed by the mutual inductance. In synthesizing the sensing transformer, the mutual inductance shaping approach is used to obtain the resolver outputs which vary linearly with respect to the rotor position. Since mutual inductance is the main parameter to represent the coupling, calculation of mutual inductance would be sufficient to determine the proper winding distribution as well as to predict the shape of the sensing transformer output voltages.

6.8.4 Calculation of inductance

Due to the field orientation and winding pattern configurations, electromagnetic field distribution of the PCB resolver is a typical 3D field. Therefore, its inductance analysis is very time consuming and computationally extensive if nonlinear property of the core is taken into account. As the resolver is a signal converter, which does not need to use strong current, or strong magnetic field, in the operation, the saturation and nonlinear effect of cores can be neglected. This has been proven in the simulation of excitation transformer. Therefore, the analysis will assume the sensing transformer as an air core coupled inductor.

For determining the inductance, empirical formulae cannot be applied as the winding cannot match with the standard circular, rectangular, hexagonal spirals. Moreover, multilayer coupling demands more complex computing.

The semicircular winding pattern is not cylindrical around z-axis. Therefore, the model cannot be deuced to 2D x-z model and the inductance cannot be computed like in excitation transformer winding using 2D finite element simulator, ANSYS MAXWELL. The 3D field simulator could be used for such geometry but the

computation is very time consuming and it is impractical when the winding pattern becomes complicated with multiple layers.

For the inductance calculation in radio frequency (RF) applications, FastHenry from MIT is well known for its accurate and reasonably fast performance. Though it is designed for high frequency (GHz) applications, it can compute inductance and resistance starting from 0Hz (i.e., DC). Therefore, FastHenry is used in determining the inductance and resistance of the winding.

In order to use FastHenry, the winding geometry needs to be described in the proprietary file format. MATLAB script is developed to generate the required geometry input files. FastHenry [64] used the fast multipole method (FMM) for accelerating the dense matrix-vector products required by an iterative solver. FMM was originally developed for particle simulation problems [64]. FastHenry is based on circuit parameter extraction using the partial element equivalent circuit (PEEC) method. The PEEC method can be applied to objects with non-orthogonal geometries [65], i.e., where edges of bodies lie not along the axes of the underlying coordinate system. Therefore, it is the right tool to compute the inductance of the multi-layer PCB winding layouts of the PCB resolver.

6.9 Design evaluation of PCB linear resolver

Simulations are carried out to obtain the inductance profiles of the PCB resolver with three winding patterns, while rotating the rotor for one revolution. The inductance values are calculated at every five degree step. For each winding pattern two cases are studied to observe the changes. In order to save the computation time, the separation distance between tracks is doubled and half of the total number of tracks is used in simulation.

With the winding patter I, two cases are simulated using the parameters:

(1) β = 5 degrees, and

(2) β = 20 degrees.

The simulated results are shown in Figure 6.16. To be consistent with the description in the analysis of a normal sinusoidal resolver, the two orthogonal sensor secondary windings are still called as sine and cosine windings, respectively.

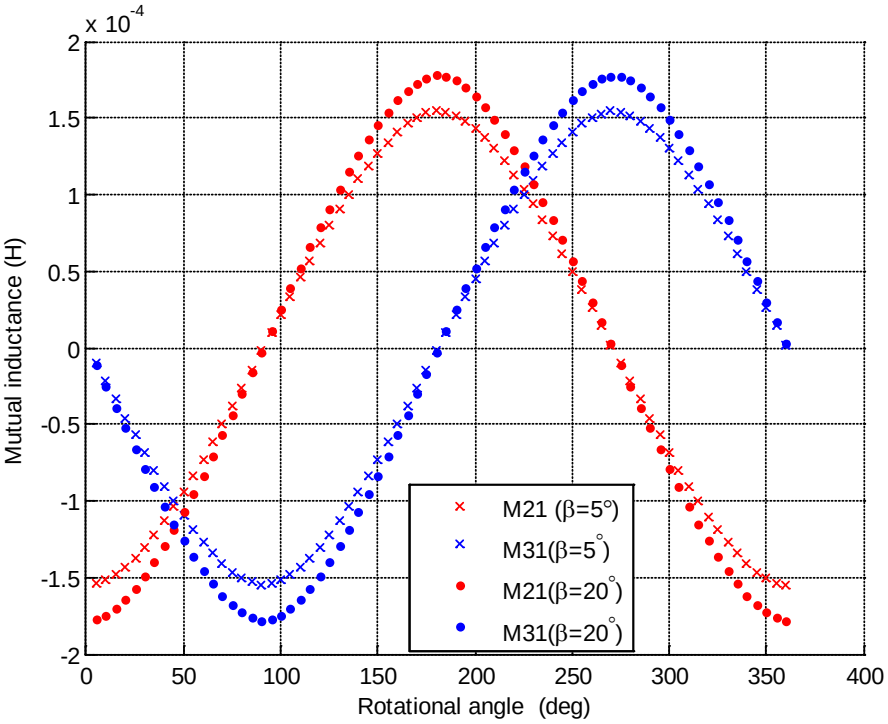

M21: mutual inductance between rotor winding and sensor sine winding
M31: mutual inductance between rotor winding and sensor cosine winding

Figure 6.16. Winding pattern I: mutual inductance profiles

Similarly, with the winding patter II and III, two cases are simulated for each pattern using the parameters (1) k=1 and (2) k = 1.5. The simulated results are shown in Figures 6.17 ~ 6.18.

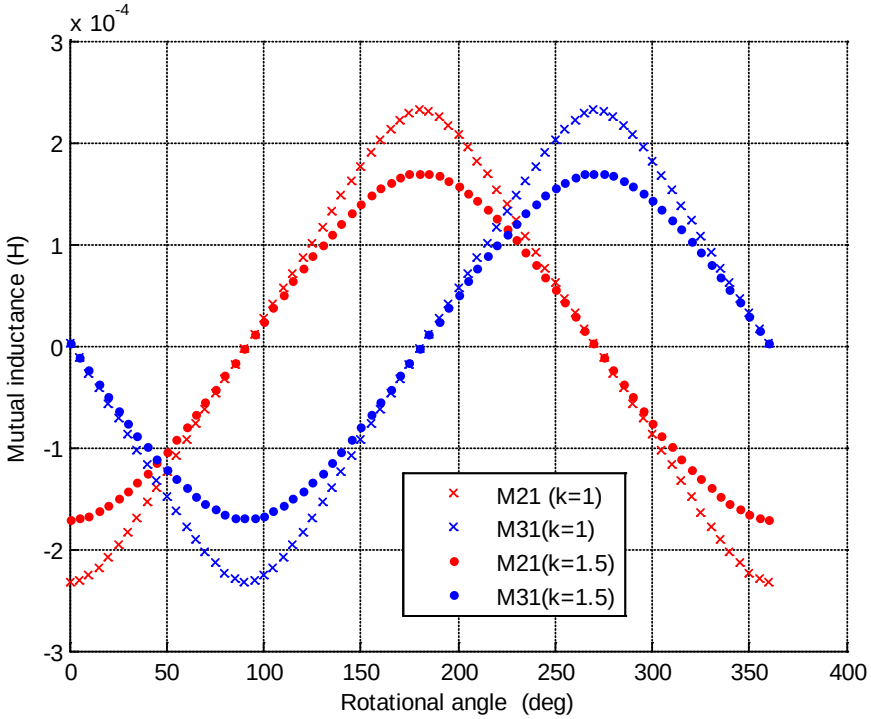

M21: mutual inductance between rotor winding and sensor sine winding
M31: mutual inductance between rotor winding and sensor cosine winding

Figure 6.17. Winding pattern II: mutual inductance profiles

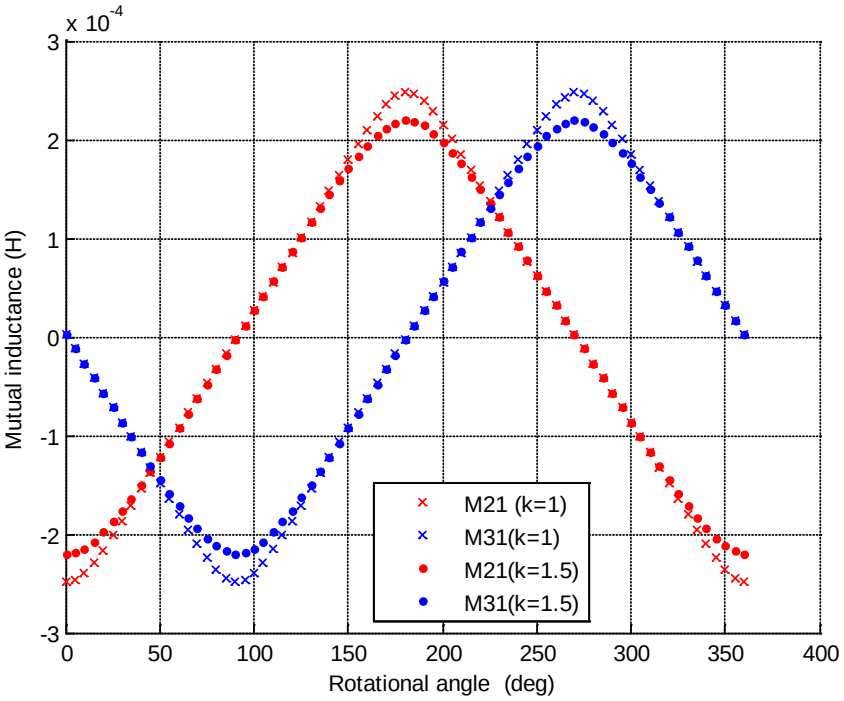

M21: mutual inductance between rotor winding and sensor sine winding
M31: mutual inductance between rotor winding and sensor cosine winding

Figure 6.18. Winding pattern III: mutual inductance profiles

From the simulation results, winding pattern I is found to generate the coupling which is close to a sinusoidal function. Winding pattern II also generates a sinusoidal like function when k is 1.5. But when k is 1, the coupling pattern is more close to a triangular function. In other words, when the total area occupied by the winding turns is smaller, the coupling in winding pattern II is more like a sinusoidal. The triangular coupling pattern is obvious in coupling of the winding pattern III. Linearity is therefore significant for the winding pattern III.

Using the piecewise linear segments fitting using Least Squares (LS) method, the best linearity is verified to choose the right winding pattern for sensing transformer of the PCB resolver. In verification, only cosine mutual inductance profile with higher coupling, (i.e. for winding pattern I, the profile for β=20 degrees is used, for winding pattern II and III, the profile for k=1 are used), is adopted to test the linearity. The LS fit used 6 segments for one complete cycle of mutual inductance profile. The results are shown in Figures 6.19 ~ 6.21.

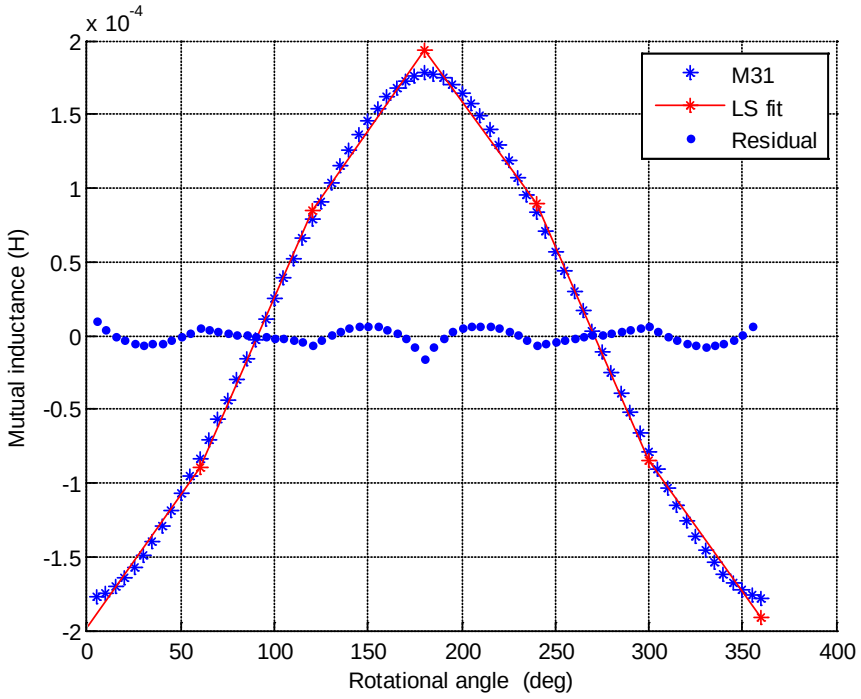

Figure 6.19. Winding pattern I: piecewise linear segments fit

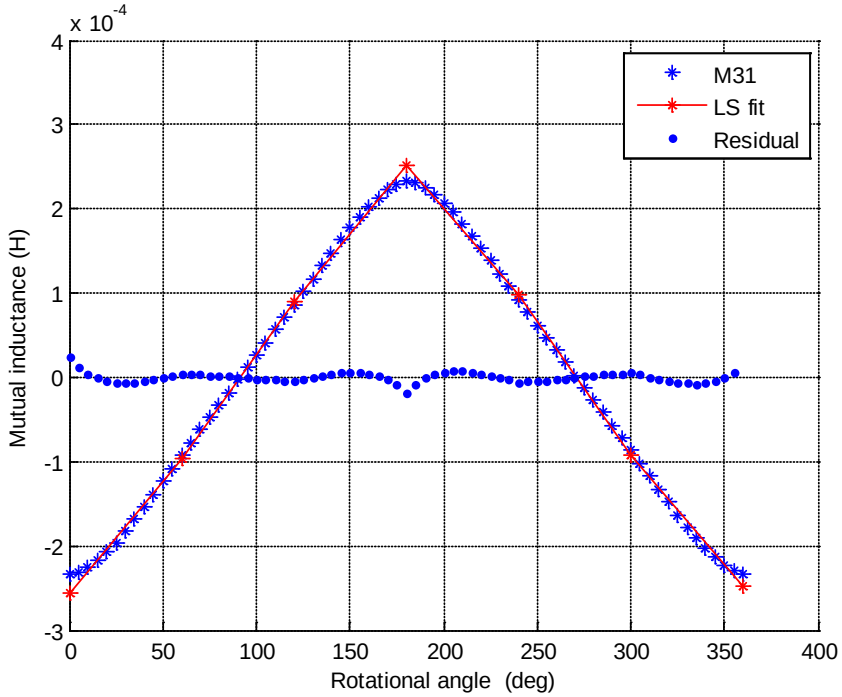

Figure 6.20. Winding pattern II: piecewise linear segments fit

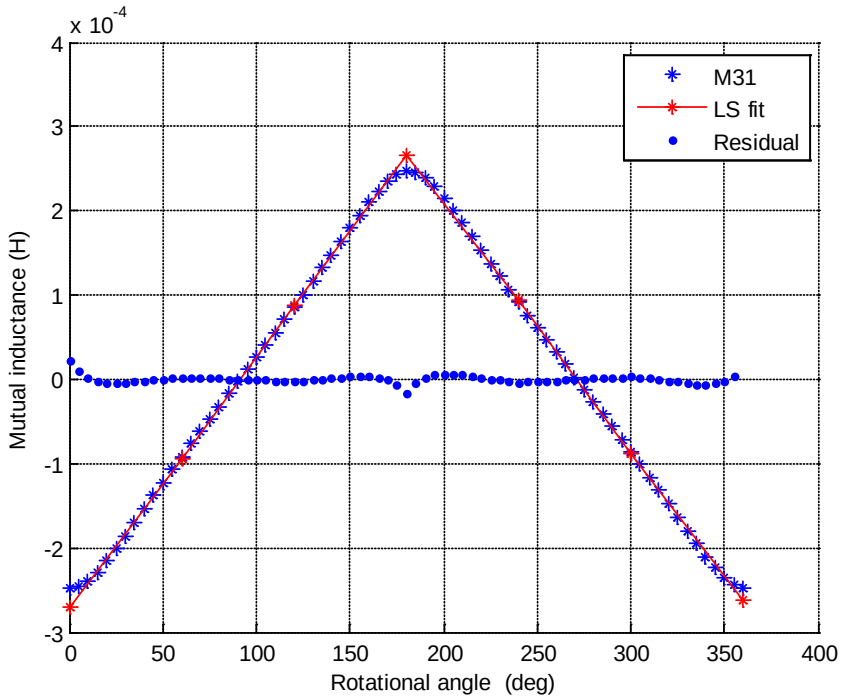

Figure 6.21. Winding pattern III: piecewise linear segments fit

Based on the residual level from the piecewise linear segments fit by the LS method, for the linear coupling function, winding pattern III is selected. Using the designed number of tracks and PCB tracks specification, simulation is carried out to determine the mutual inductances of PCB resolver. The result is shown in Figure 6.22.

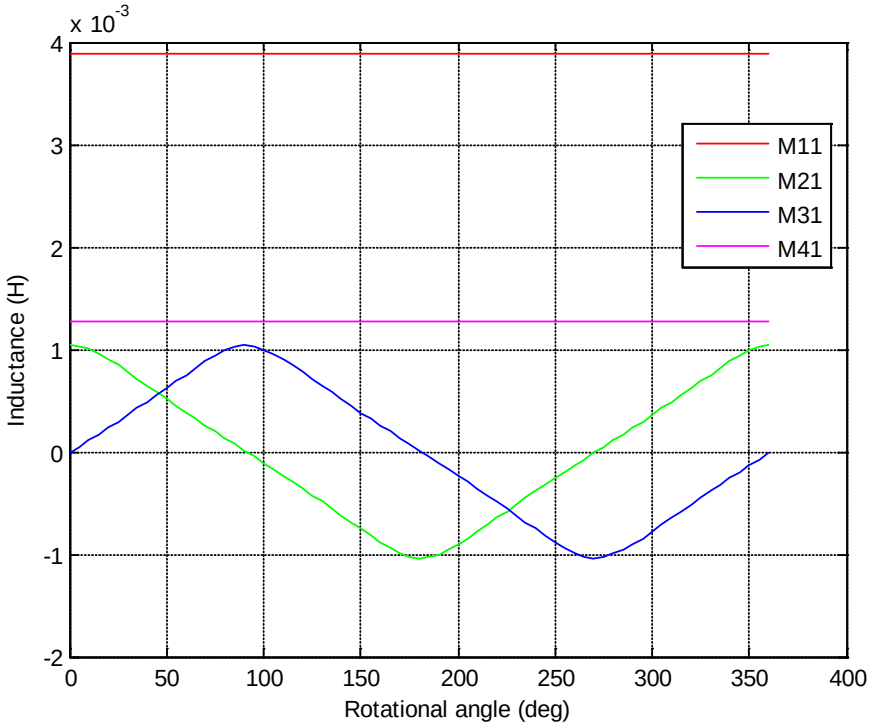

M11: self inductance of rotor winding
M21: mutual inductance between rotor winding and sensor sine winding
M31: mutual inductance between rotor winding and sensor cosine winding
M41: mutual inductance between rotor winding and sensor primary winding

Figure 6.22. Mutual inductance profiles of PCB resolver

It is observed that mutual inductance between rotor winding and excitation primary winding is constant for the whole revolution. It means that sensing primary would be provided with constant power independent of rotor position and therefore the synthesis of exaction transformer windings meets the design objective. The mutual inductance between the two output windings also proves that the output voltages are 90 degrees displaced, and thus the requirement of outputs being in

quadrature is satisfied. The only exception is the sinusoidal property of the output voltages. As expected, the flux linkage varies linearly in the whole revolution except around the peaks. From Figure 6.22, it can be found that, for the final winding pattern determined, mutual inductances, M21 and M31vary linearly with rotor position in the disconnected ranges. (i.e., for M21, piecewise linearity can be found in the ranges from 45 degrees to 135 degrees and from 225 degrees to 315 degrees, and for M31, piecewise linearity can be found in the ranges complement to that of M21.) This result agrees with what we expected, and it assures that the winding pattern is designed correctly.

6.10 Development of linear PCB resolver with two outputs

After evaluating the winding pattern for sensing transformer winding by simulation, the winding layouts of the PCB linear resolver for fabrication are designed following the PCB design rules and specified core dimensions. The layouts for the prototypes are shown in Figures 6.23 ~ 6.25. It should be noted that the winding layouts for excitation transformer primary and secondary sides are exactly the same.

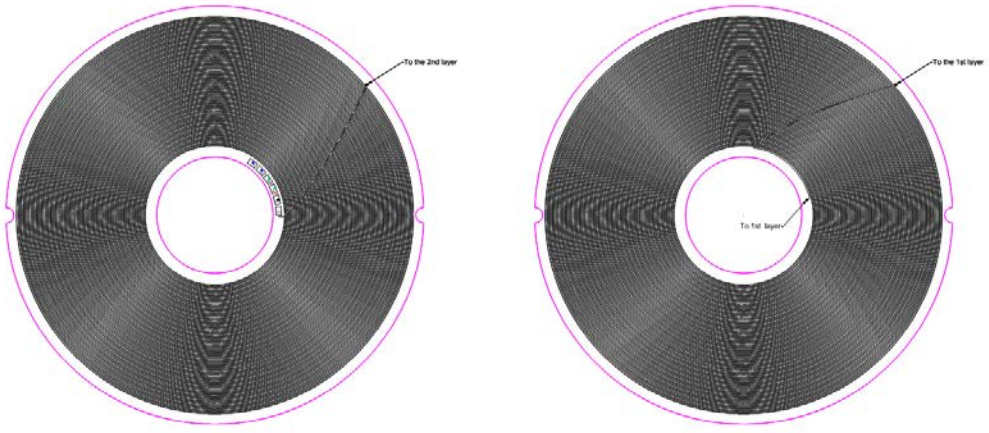

Figure 6.23. Excitation transformer windings for fabrication

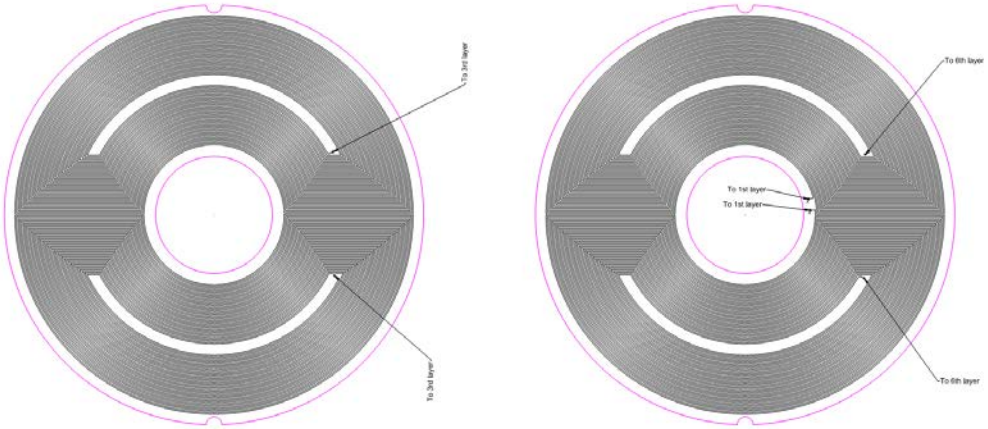

Figure 6.24. Sensing transformer primary winding for fabrication

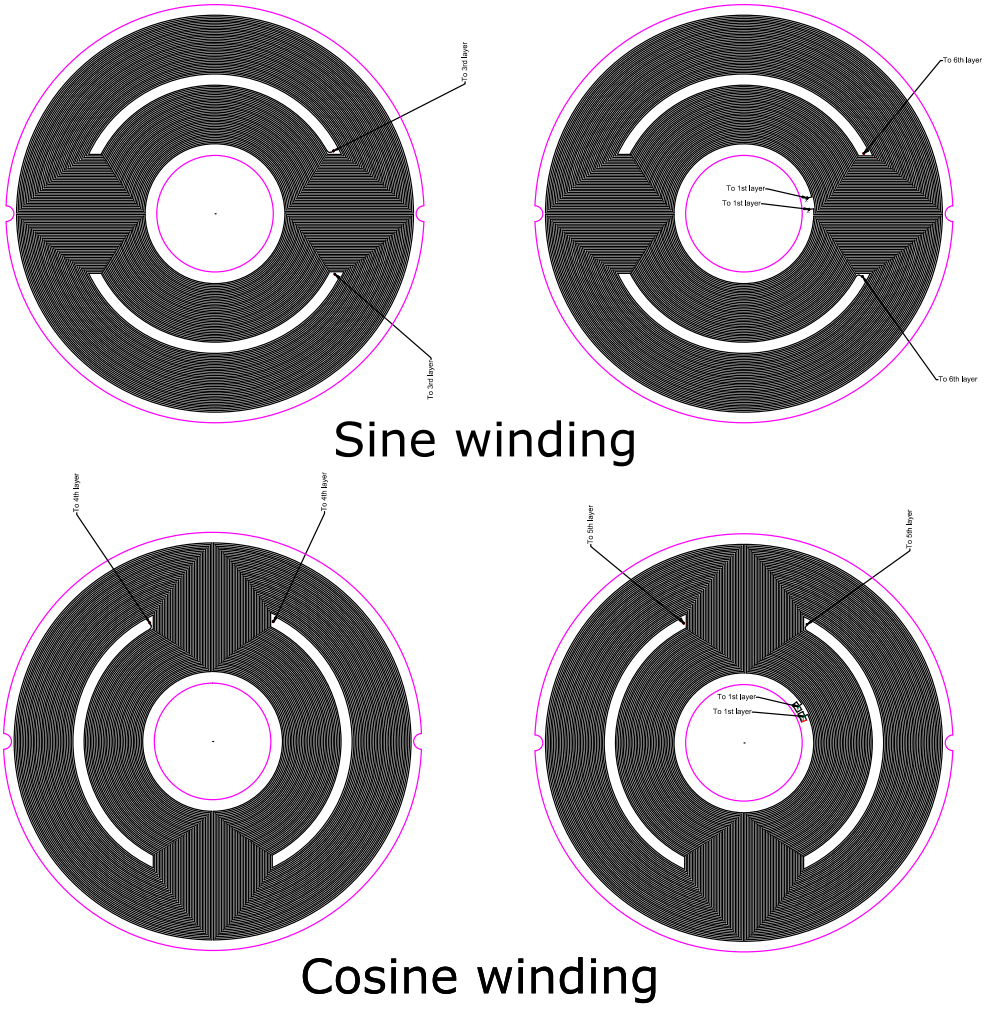

Figure 6.25. Sensing transformer secondary windings for fabrication

Utilizing the piecewise linear regions of the two outputs shown in Figure 6.22, the effective operation range of PCB linear resolver can be 360 degrees. This however requires a proper algorithm to select the segments and map the measured signal amplitudes to corresponding angle values.

6.11 Prototype of PCB resolver

To verify the feasibility of PCB resolver, a PCB resolver is fabricated based on the parameters and the material specified. The cut-away view of the prototype and the exploded view of the PCB resolver are shown in Figures 6.26 ~ 6.27.

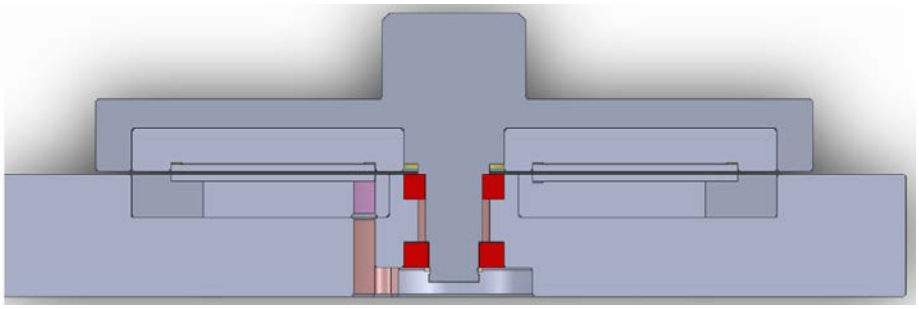

Figure 6.26. PCB resolver: cut-away view

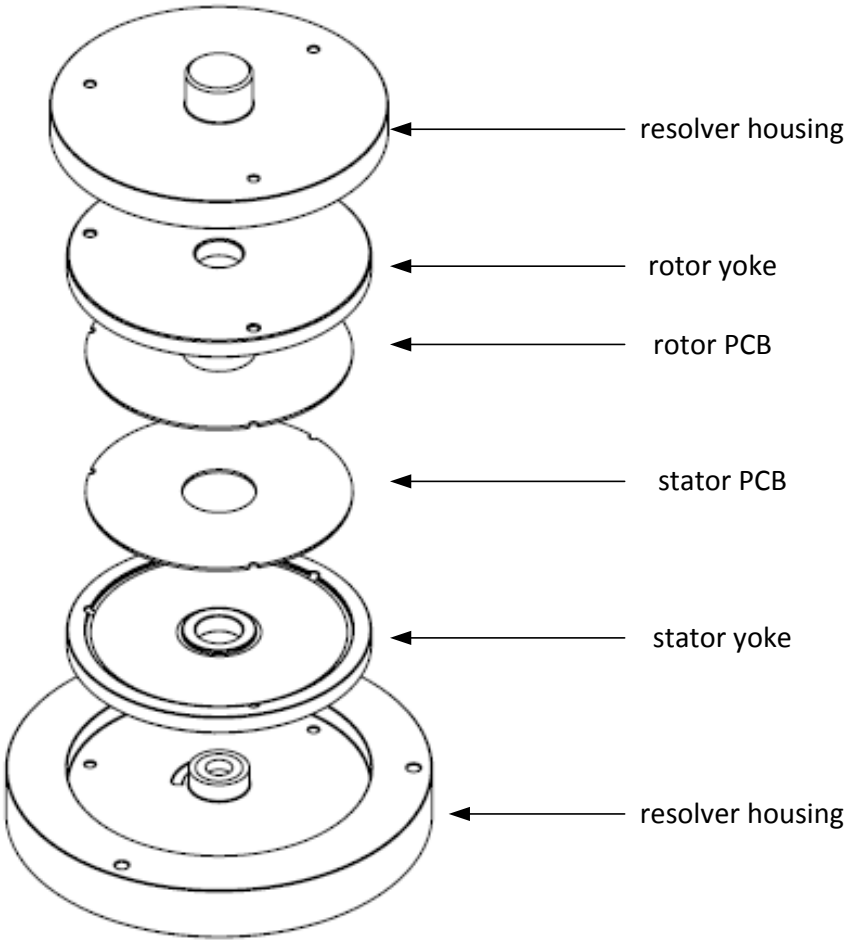

Figure 6.27. PCB resolver: exploded view

As described in the design procedure, the resolver has two main parts: the stator and the rotor. The stator and rotor windings are formed by PCB and their yokes are made with soft magnetic composite material to minimize the eddy current effect and to facilitate manufacturing process. In order to shield from the undesired effects from the outside, the resolver is enclosed in its aluminum housing.

6.12 Comparison of computation and measurement results

The validity of the computed results is verified with the measurement results from the fabricated PCB windings. It should be noted that the effect of core is not considered in the comparison. The compared results are shown in Table 10.

Table 10. Comparison of computed and measured results

	Rotor Winding	Excitation primary winding	Sine winding	Cosine winding
Calculation: Inductance (H)	3.89E-03	1.42E-03	5.51E-04	5.63E-04
Measurement: Inductance (H)	3.47E-03	1.35E-03	4.90E-04	4.77E-04
Calculation: Resistance (ohm)	270.55	88.69	84.07	84.07
Measurement: Resistance(ohm)	319.78	83.703	71.34	111.761

The comparison shows that inductance calculation is in good agreement with the measured results but there is a noticeable difference in resistance calculation, especially for the rotor winding. The winding layout of rotor winding is composed of two layers from secondary excitation transformer and four layers from primary sensing transformer. For this six-layer PCB winding, there could be some variation in track thickness for the interlayer windings and this could result in some discrepancies with resistance calculation.

6.13 Experiment results of PCB resolver with two outputs

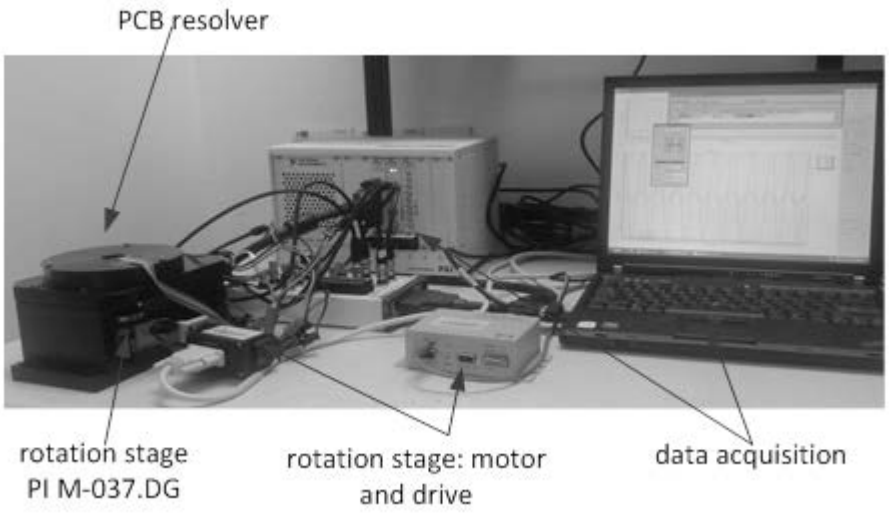

Figure 6.28. Experimental setup

The experimental setup shown in Figure 6.28 is in fact the same as the one used in verification of initial calibration method but now with the PCB resolver. In the setup, the resolver is rotated by the high precision rotary stage, PI M037 DG. The rotation of the stage is controlled by PI C-863 DC Motor Controller. The excitation signal is supplied to the resolver using NI PXI-5406 and the resolver outputs are simultaneously sampled using NI PXI-6133. Data are acquired and stored in the computer by the developed software module.

The excitation voltage has the peak value, 2.8V, and the frequency, 5kHz. The resolver outputs and the excitation signal are simultaneously acquired for every one degree step. The acquisition time is for one revolution. The normalized envelopes of the resolver outputs are obtained using DFT are shown in Figure 6.29.

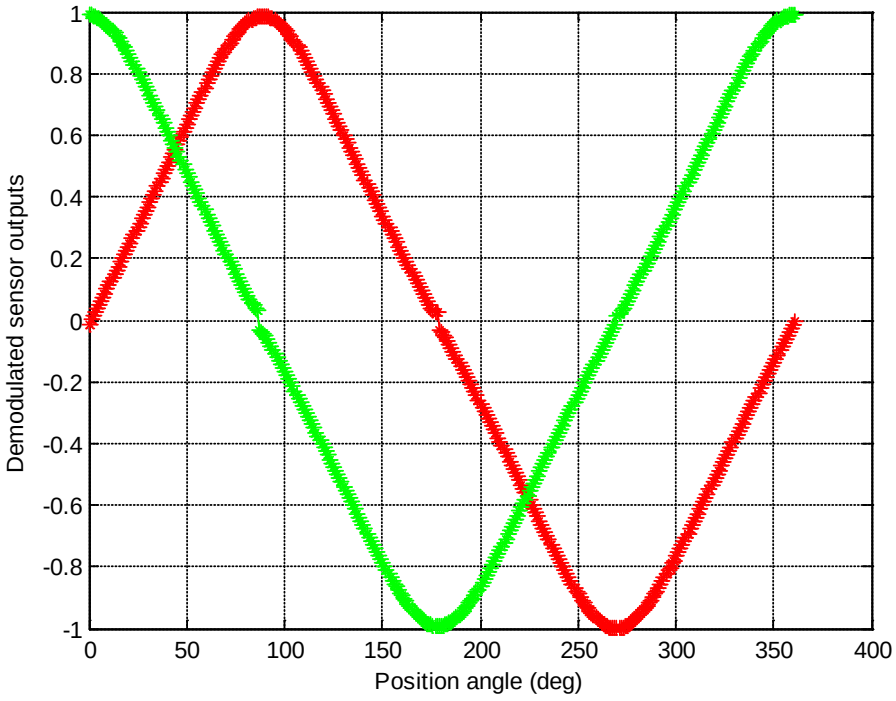

Figure 6.29. Demodulated PCB resolver outputs

It is observed that the demodulated outputs of the PCB resolver contain some harmonics and they are made up of linear region and non-linear regions. It can be found that the simulation results can well predict the physical resolver outputs. However, the null point errors, i.e., discontinuities at the zero crossings are found in the measured results. This effect could be due to constant flux linkage from excitation transformer primary windings to the resolver output windings, or sensing transformer secondary windings. Therefore the idea of using alternate linear segments to retrieve the position angle becomes impossible and the development of linear PCB resolver cannot be realized.

6.14 Development of 3-phase PCB linear resolver

In order to overcome the problem of null point errors, the efficient solution is to employ one additional winding in the resolver output windings. For a resolver with PCB winding structure, this just alters the initial design by adding an additional PCB layer and adjusting the air gap length accordingly. With the additional winding, the resolver output windings are distributed in such a way that the outputs are 120 degrees apart in space as a three phase system, i.e., a 3-phase linear resolver can be realized. The winding pattern is shown in Figure 6.30.

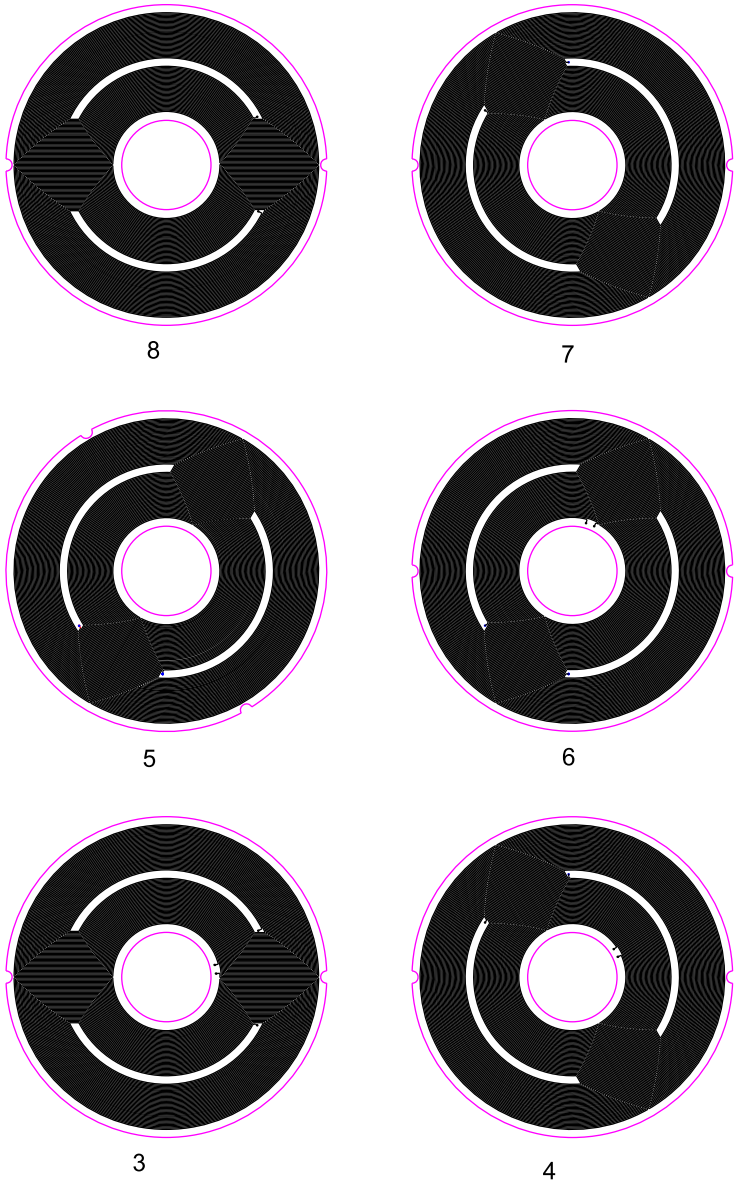

Figure 6.30. Sensing transformer winding pattern for 3-phase PCB linear resolver

6.15 Experimental results of 3-phase PCB linear resolver

In order to prove the concept of 3-phase PCB linear resolver, the new stator PCB having eight layers is fabricated. With the same experimental setup, the measurements are taken and the resolver outputs are demodulated. The result is shown in Figure 6.31.

With the additional resolver outputs, the realization of PCB resolver becomes possible. In Figure 6.31 the red segments represent the linear regions and an angle extraction algorithm is required to convert the data at these segments into angular positions.

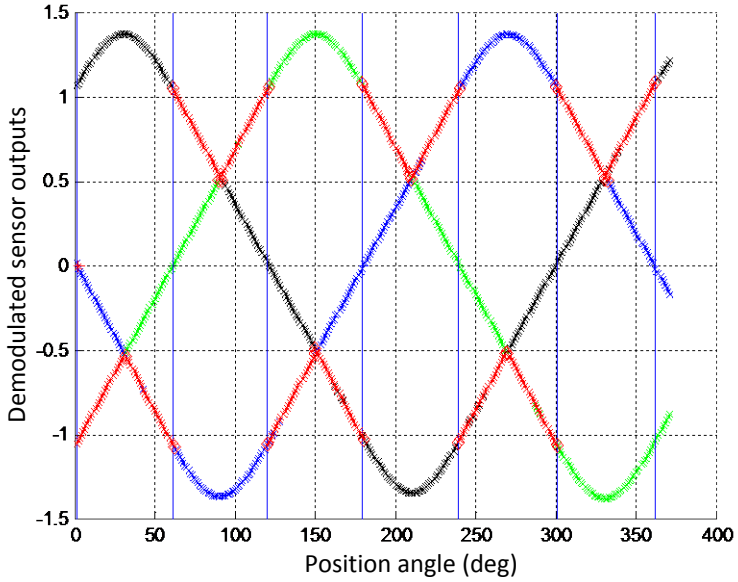

Figure 6.31. Demodulated PCB resolver outputs

6.16 Algorithm for extracting the position angle

There are three main steps to extract the position angle from demodulated resolver outputs:

1. Identifying the location of piecewise linear segments
2. Determining the slope and intercept of each segment
3. Mapping to angles from the segments.

The location of linear segments from the demodulated resolvers can be identified from the two curves, which are derived from the polarity of the demodulated outputs and the comparison of absolute value of the demodulated outputs. The two curves and

the logic illustrating the derivation of the curves are shown in Figures 6.32 ~ 6.33. Based on unique combinations from the two curves, the location of segments can be identified.

The slope and intercept of each segment are determined using LLSE method as described in Chapter 5. These two steps can be performed in initial calibration stage of the resolver.

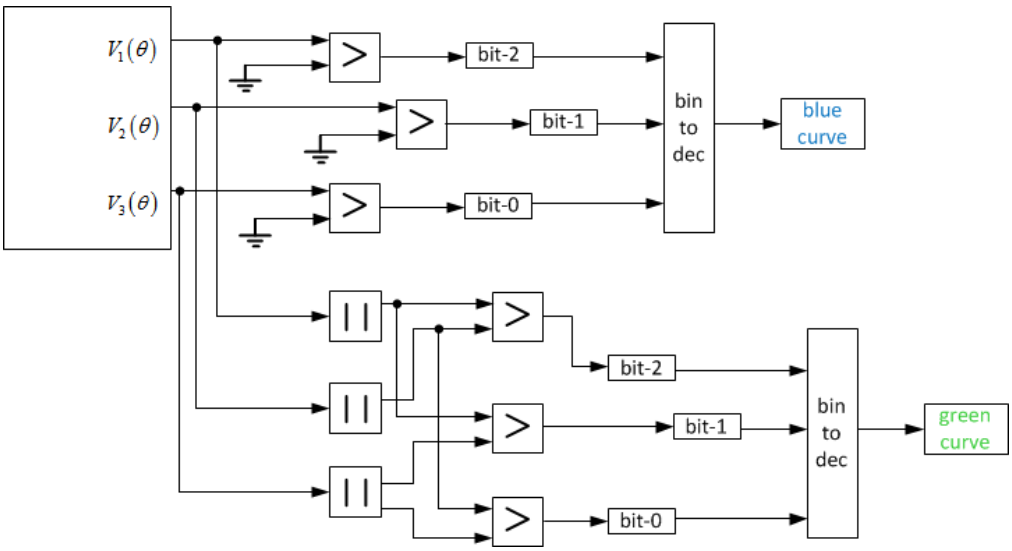

Figure 6.32. Block diagram to derive the curves

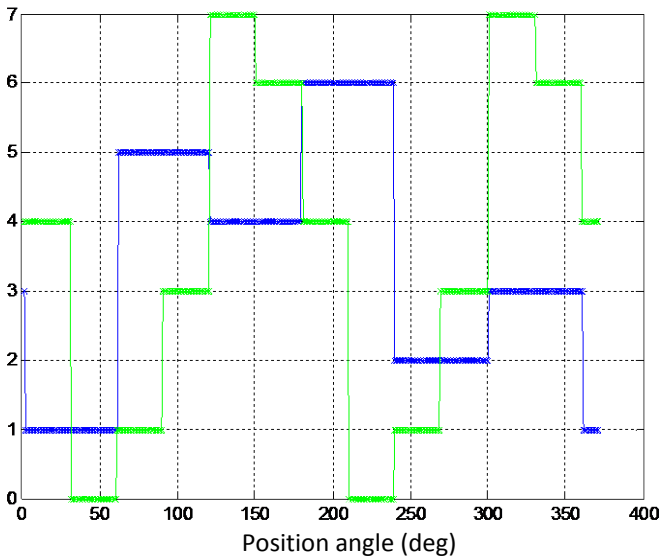

Figure 6.33. Two curves for identifying linear segments

Once the slopes and intercepts of the segments are determined, these values can be stored in a look-up table, the actual position angle can then be retrieved by

$$\theta_{measured} = \frac{V - c_{segment}}{m_{segment}}, \tag{6.5}$$

where V is the amplitude of the resolver output and $c_{segment}$ and $m_{segment}$ are the intercept and slope values of the segment where the resolver output belongs to, respectively.

6.17 Evaluation of the PCB resolver accuracy

Using the algorithm for extracting the position angle, evaluation is performed to investigate the accuracy of the fabricated PCB resolver. Two sets of experiment data are acquired and the angular position values are determined. The first experiment is carried out with the excitation voltage of 5V and the frequency of 5kHz. The second experiment keeps the same excitation voltage, but with the frequency of 10kHz.

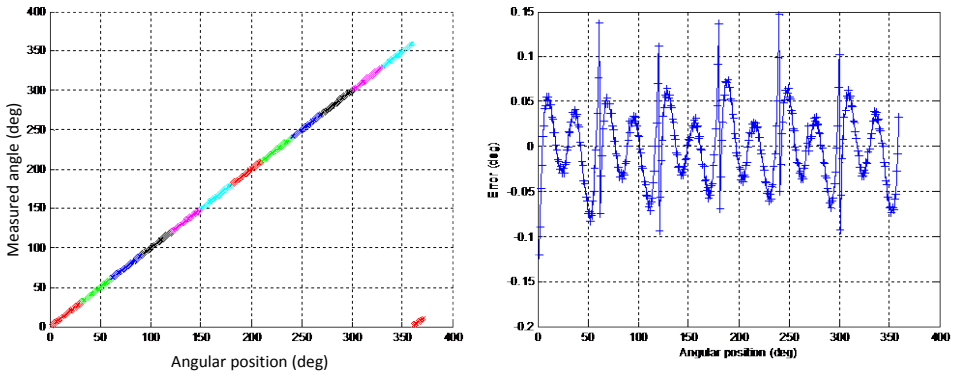

Figure 6.34. Measured position values and the error profile (5V, 5kHz)

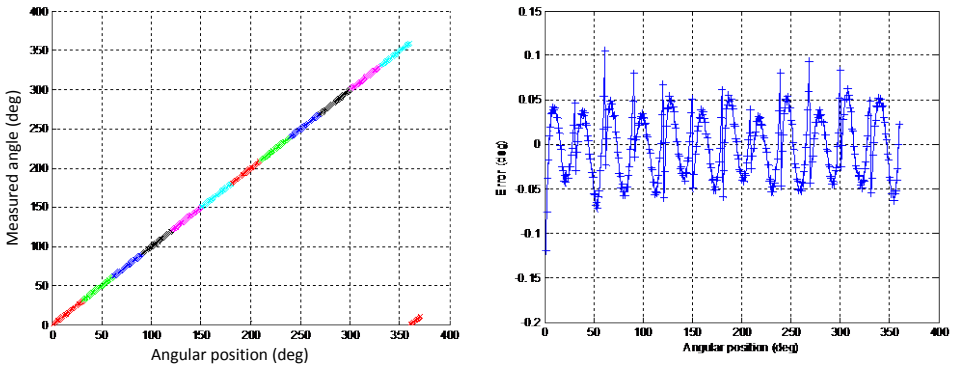

Figure 6.35. Measured position values and the error profile (5V, 10kHz)

The computed position angles and the respective error profiles are shown in Figures 6.34 ~ 6.35. It is known that the obtained accuracy of the new PCB resolver is in the range of 5 ~ 10 arc minutes, which is comparable to the accuracy of industrial resolvers. It was mentioned before that, so far there is no brushless rotatable linear resolver in the market. This PCB linear resolver is brushless and operation range is 360 degrees, and its potential market is huge.

6.18 Conclusion

Improving the accuracy and reducing the cost of a resolver are very challenging. With the existing structures of brushless resolvers and VR resolvers, the accuracy improvement and cost reduction are limited. Although error compensation methods can improve the accuracy, the better approach is to eliminate the source of errors.

In this regard, this chapter explores the development a novel resolver structure and introduces an absolute 3-phase PCB linear resolver. Since PCB windings are employed, both the design and manufacturing processes are much simplified. In fact, by taking advantage of the flexibility of winding pattern design, the resolver can be constructed to obtain various functions of rotor position. Based on the constraints of PCB winding and operating principle of resolver, detailed procedure to synthesize a

PCB resolver is presented. With the linear segments of the resolver outputs, an algorithm to retrieve the angular position is derived. It has shown that the achievable accuracy of the new resolver is comparable to that of industrial resolvers. With the simplicity of the structure and linear outputs, it is believed that the PCB linear resolver can find wide range of applications that require shaft position sensing.

7 Conclusions and future work

In this research, the analysis and synthesis of precision resolver system are presented. Analysis of a brushless resolver is carried out based on its operating principle and the equations are derived to determine the parameters which can affect the performance. Taking into account of possible factors that influence the accuracy of a resolver, the characteristics of errors based on the tolerance of parameters are investigated. The analysis of results highlights the constraints of design parameters and their influence on the accuracy. In order to make the high precision brushless resolvers, the production cost will be high due to tight design constraints and combination of the two different electromagnetic structures.

As the resolver outputs are amplitude modulated signal, demodulation is required to retrieve the position signal. In order to suppress the noise in resolver outputs in the demodulation process, a new approach which is based on synchronous integration of the direct outputs of a resolver is presented. The proposed approach makes a compromise between the computational resources and accuracy, yielding good suppression of noise and improvement in accuracy. The performance of the proposed method is verified with simulations and experiments. It is shown that the proposed method can minimize the noise effect up to 30dB SNR level.

In practice, sensors require calibration to maintain their designed accuracy. Due to rugged applications of resolvers, it can be reasoned that both initial calibration and online error compensation are needed. This research proposed an initial calibration method based on parameter estimation of a sinusoidal signal. The proposed initial calibration method is extended to online error compensation method using the error model expressed in complex frequency domain. Parameters of sinusoids are estimated by feedback integration approach and amplitude tracking is incorporated in the

method. The effectiveness of the method is demonstrated with simulations and experiments.

Discerning the results from error analysis and position retrieving process, this research develops a new type of resolver. The new resolver adapts the PCB technology and attempts to overcome the shortcomings of the traditional resolver. It has an axial orientation and slot-less structure with SMC cores. Taking advantage of the flexibility in winding pattern design, the presented PCB axial field resolver can even realize linear rotational resolver. The linear resolver with this novel design can be used in many areas, and solve the big concerns in the application of existing linear resolver. The detailed development of the synthesis of the new resolver is presented and its workability is verified with the prototypes. It has demonstrated that the obtained accuracy of the new resolver is comparable with that of industrial resolvers.

There are still many research areas that should be carried out to realize robust demodulation of the resolver signal. Most of the demodulation methods depend on reference signal and the phase shift has a negative effect on resolver accuracy. Application specific demodulation schemes are also possible as the frequency of reference signal is related to the shaft speed.

As the calibration is an essential process, further research should be focused to make the calibration time shorter, and the accuracy of the calibration better, and the calibration more robust.

The research on the PCB axial field resolver presented in the thesis show only our research in the linear resolver. There is still a very wide space to explore the new structure and new application of this kind of resolver. One direction is to realize the other kind of output signal functions to the rotor position, e.g., polynomial functions and triangle functions. As there is flexibility in selecting the phase number, the resolver can also be designed with different phase for different application.

In the results presented in the thesis, the sensor windings are designed with one pole-pair. Actually, the fast development of PCB technology will certainly give researchers more freedom in winding pattern design. It means that the resolver can be designed with multipoles. This will allow us to realize resolver with higher resolution.

It can be estimated that the performance of SMC material will also be improved significantly in the coming years. Some other high performance ferrite materials could also enter market soon. All these will allow the researchers to use more complicated 3D structure to realize high performance and compact resolvers,

As its low cost and high performance, the new resolver solution presented in the thesis should inspire more research directions in the related areas, and get very wide applications in industrial, defense and domestic products.

Bibliography

[1] E. Kiel and E. Kiel, Drive Solutions: Mechatronics for Production and Logistics. Springer Berlin Heidelberg, 2008.

[2] “The Measurement, Instrumentation, and Sensors Handbook”, CRC Press and IEEE Press, 1999, pp. 6.108-6.141.

[3] J. Figueiredo, “Resolver Models for Manufacturing,” IEEE Transactions on Industrial Electronics, vol. 58, no. 8, pp. 3693–3700, Aug. 2011.

[4] David Laing, “A Look into the Linear Displacement and Rotary Position Sensor Markets,” http://www.sensorsmag.com/sensors/position-presence-proximity/a-look-linear-displacement-and-rotary-position-sensor-market-7699,. Web. 6 Jan, 2011.

[5] DU, Chun-yang, Sheng LIU, and Kai-qi ZHAO. "A DSP-Based Fast Tracking Resolver-to-Digital Conversion Method [J]." Control Engineering of China 1 (2010): 011

[6] http://www.ormec.com/Portals/0/files/Services/Applications/ApplicationNotes/EncoderVsResolver.pdf, .Web. 10 Aug, 2013.

[7] http://www.usa.canon.com/cusa/semiconductor/products/encoder_optolectronic_components/laser_rotary_encoder/x_1m, Web 6 Jan, 2013.

[8] http://www.navymars.org/national/training/nmo_courses/NMOC/module15/14187_ch1.pdf, .Web. 6 Feb, 2013.

[9] “Rotary Transformer Design,” in Transformer and Inductor Design Handbook, Fourth Edition, 0 vols., CRC Press, 2011, pp. 1–10.

[10] http://www.moog.com/literature/MCG/synchrohbook.pdf, Web. 15, Nov, 2012.

[11] C. Ebbesson, “Comparative study of different rotary position sensors for electrical machines used in an hybrid electric vehicle application,” Master Thesis, Lund university, Lund, Sweden, 2011.

[12] L. Z. Sun, J. B. Zou, and Y. P. Lu, “New variable-reluctance resolver for rotor-position sensing,” in TENCON 2004. 2004 IEEE Region 10 Conference, 2004, vol. D, pp. 5 – 8 vol. 4.

[13] D. C. Hanselman, R. E. Thibodeau, and D. J. Smith, “Variable-reluctance resolver design guidelines,” in , *15th Annual Conference of IEEE Industrial Electronics Society*, 1989. IECON ’89, 1989, pp. 203 –208 vol.1.

[14] L. Z. Sun and Y. P. Lu, “Rotor-position Sensing System based on one type of Variable-reluctance Resolver,” in *IECON 2006 - 32nd Annual Conference on IEEE Industrial Electronics*, 2006, pp. 1162–1165.

[15] L. Z. Sun, “Analysis and Improvement on the Structure of Variable Reluctance Resolvers,” *IEEE Transactions on Magnetics*, vol. 44, no. 8, pp. 2002–2008, Aug. 2008.

[16] Greg Leibovich and Sara Senanian, "Development of Variable Reluctance Resolver for Position Feedback", Proceedings of the 41st Aerospace Mechanisms Symposium, Jet Propulsion Laboratory, May 16-18, 2012.

[17] C. Liu, M. Qi, and M. Zhao, “Analysis of Novel Variable Reluctance Resolver with Asymmetric Teeth on the Stator,” Mathematical Problems in Engineering, vol. 2013, pp. 1–9, 2013.

[18] Shang Jing, Liu Chengjun, and Zou Jibin, “The analysis for new axial variable reluctance resolver with air-gap complementary structure,” presented at the International Conference on Electrical Machines and Systems, 2009. ICEMS 2009, 2009, pp. 1–6.

[19] S. jing, Z. Meng, and J. Shanlin, “The Principle of Reluctance Resolver and EMF Waveform Optimization Based on FEM,” in 2011 First International Conference on Instrumentation, Measurement, Computer, Communication and Control, 2011, pp. 615–618.

[20] D. Pazouki, M. Ghafarzadeh, R. Abedini, A. D. Aliabad, and E. A. Kamali, “A novel brushless synchro: Operation principle and experimental results,” in Electrical Engineering (ICEE), 2013 21st Iranian Conference on, 2013, pp. 1–6.

[21] W. Jiuqing, L. Xingshan, and G. Hong, “The analysis and design of high-speed brushless resolver plus R/D converter shaft-angle measurement system,” 2001, vol. 1, pp. 289 –292 vol.1.

[22] D. Arab-Khaburi, F. Tootoonchian, and Z. Nasiri-Gheidari, “Parameter identification of a brushless resolver using charge response of stator current,” Iranian Journal of Electrical & Electronic Engineering, vol. 3, no. 1&2, pp. 42–52, 2007.

[23] D. Arab-Khaburi, F. Tootoonchian, and Z. Nasiri-Gheidari, “Dynamic Performance Prediction of Brushless Resolver,” Iranian Journal of Electrical & Electronic Engineering, vol. 4, no. 3, pp. 94–103, 2008.

[24] F. Tootoonchian, K. Abbaszadeh, and M. Ardebili, “Novel Axial Flux Brushless Resolver Analysis and Optimization using 3D Finite Element and DQ Model Method,” Iranian Journal of Electrical & Electronic Engineering, vol. 8, no. 3, p. 243, 2012.

[25] F. Tootoonchian, K. Abbaszadeh, and M. Ardebili, “A New Technique for Analysis of Static Eccentricity in Axial Flux Resolver,” Measurement Science Review, vol. 12, no. 1, Jan. 2012.

[26] A. Michalski, J. Sienkiewicz, and Z. Watral, “Universal Magnetic Circuit for Resolvers with Different Speed Ratios [Instrumentation Notes],” IEEE Instrumentation & Measurement Magazine, vol. 10, no. 5, pp. 58–68, Oct. 2007.

[27] A. Kaewpoonsuk, W. Petchmaneelumka, T. Kamsri, and V. Riewruja, “A Simple Resolver-to-DC Converter,” in SICE-ICASE, 2006. International Joint Conference, 2006, pp. 5754 –5757.

[28] A. Kaewpoonsuk, T. Kamsri, W. Petchmaneelumka, and V. Riewruja, “A full-range-360° resolver-to-DC converter,” in Control, Automation and Systems, 2007. ICCAS ’07., pp. 802–805.

[29] L. Ben-Brahim, M. Benammar, and M. A. Alhamadi, “A Resolver Angle Estimator Based on Its Excitation Signal,” IEEE Transactions on Industrial Electronics, vol. 56, no. 2, pp. 574–580, Feb. 2009.

[30] A. Kaewpoonsuk, R. Katman, T. Kamsri, A. Rerkratn, and V. Riewruja, “A simple amplitude detector-based demodulator for resolver converters,” in 2010 International Conference on Control Automation and Systems (ICCAS), 2010, pp. 370–373.

[31] Choong-Hyuk Yim, In-Joong Ha, and Myoung-Sam Ko, “A resolver-to-digital conversion method for fast tracking,” Industrial Electronics, IEEE Transactions on, vol. 39, no. 5, pp. 369–378, 1992.

[32] A. O. Di Tommaso and R. Miceli, “A new high accuracy software based resolver-to-digital converter,” in Industrial Electronics Society, 2003. IECON ’03. The 29th Annual Conference of the IEEE, 2003, vol. 3, pp. 2435 – 2440 Vol.3.

[33] Ji-Hye Jeon, Dong-Yoon Shin, Yoon-Gi Yang, Jin-Kwon Hwang, and Chang-Su Lee, “A FPGA implementation of resolver-based absolute position detector,” presented at the International Conference on Control, Automation and Systems, 2007. ICCAS ’07, 2007, pp. 2375–2378.

[34] S. Sarma, V. K. Agrawal, and S. Udupa, “Software-Based Resolver-to-Digital Conversion Using a DSP,” IEEE Transactions on Industrial Electronics, vol. 55, no. 1, pp. 371–379, Jan. 2008.

[35] S. Sarma, V. K. Agrawal, S. Udupa, and K. Parameswaran, “Instantaneous angular position and speed measurement using a DSP based resolver-to-digital converter,” Measurement, vol. 41, no. 7, pp. 788–796, Aug. 2008.

[36] Zhu Yi, Wang Jian-ming, and Zhu Ming, “An approach based on AD converted resolver demodulation,” in 2010 3rd International Conference on Advanced Computer Theory and Engineering (ICACTE), 2010, vol. 5, pp. V5–192–V5–195.

[37] D. C. Hanselman, “Techniques for improving resolver-to-digital conversion accuracy,” IEEE Transactions on Industrial Electronics, vol. 38, no. 6, pp. 501–504, Dec. 1991.

[38] D. C. Hanselman, “Resolver signal requirements for high accuracy resolver-to-digital conversion,” IEEE Transactions on Industrial Electronics, vol. 37, no. 6, pp. 556–561, Dec. 1990.

[39] D. C. Hanselman, “Signal processing techniques for improved resolver-to-digital conversion accuracy,” in , 16th Annual Conference of IEEE Industrial Electronics Society, 1990. IECON ’90, 1990, pp. 6–10 vol.1.

[40] B. A. Murray and W. D. Li, “A digital tracking R/D converter with hardware error calculation using a TMS320C14,” in Power Electronics and Applications, 1993., Fifth European Conference on, 1993, pp. 472 –477 vol.4.

[41] A. Bunte and S. Beineke, “High-performance speed measurement by suppression of systematic resolver and encoder errors,” IEEE Transactions on Industrial Electronics, vol. 51, no. 1, pp. 49– 53, Feb. 2004.

[42] V. D. Aksenenko and S. I. Matveyev, “Digital Angle Sensor Self-Calibration: Two Approaches to Accuracy Increasing,” in Proceedings of the IEEE Instrumentation and Measurement Technology Conference, 2005. IMTC 2005, 2005, vol. 1, pp. 543–547.

[43] A. Bellini and S. Bifaretti, “A digital filter for speed noise reduction in drives using an electromagnetic resolver,” Mathematics and Computers in Simulation, vol. 71, no. 4–6, pp. 476–486, Jun. 2006.

[44] R. Hoseinnezhad, A. Bab-Hadiashar, and P. Harding, “Calibration of Resolver Sensors in Electromechanical Braking Systems: A Modified Recursive Weighted Least-Squares Approach,” IEEE Transactions on Industrial Electronics, vol. 54, no. 2, pp. 1052–1060, Apr. 2007.

[45] S. K. Kaul, A. K. Tickoo, R. Koul, and N. Kumar, “Improving the accuracy of low-cost resolver-based encoders using harmonic analysis,” Nuclear Instruments and Methods in Physics Research Section A: Accelerators, Spectrometers, Detectors and Associated Equipment, vol. 586, no. 2, pp. 345–355, Feb. 2008.

[46] S. Sarma and A. Venkateswaralu, “Systematic error cancellations and fault detection of resolver angular sensors using a DSP based system,” Mechatronics, vol. 19, no. 8, pp. 1303–1312, Dec. 2009.

[47] Seon-Hwan Hwang, Hyun-Jin Kim, Jang-Mok Kim, Liming Liu, and Hui Li, “Compensation of Amplitude Imbalance and Imperfect Quadrature in Resolver Signals for PMSM Drives,” IEEE Transactions on Industry Applications, vol. 47, no. 1, pp. 134–143, Feb. 2011.

[48] Bergas-Jané, J.; Ferrater-Simón, C.; Gross, G.; Ramírez-Pisco, R.; Galceran-Arellano, S.; Rull-Duran, J.; , "High-Accuracy All-Digital Resolver-to-Digital Conversion," Industrial Electronics, IEEE Transactions on , vol.59, no.1, pp.326-333, Jan. 2012.

[49] Zhu Ming, Wang Jianming, Ding Ling, Zhu Yi, Dou Ruzhen, and Leng Yu, “A Software Based Robust Resolver-to-Digital Conversion Method in Designed in Frequency Domain,” in 2011 International Symposium on Computer Science and Society (ISCCS), 2011, pp. 244–247.

[50] G. Gross, M. Teixido, A. Sudria, and J. Bergas, “All-digital resolver-to digital conversion,” in Proc. Eur. Conf. Power Electron. Appl., Sep. 11–14, 2005, pp. P.1–P.8.

[51] X. Yongxiang, Z. Dianchen, W. Yanyu, Z. Jibin, and S. Jing, “DSP based all-digital resolver-to-digital conversion using DSRF-PLL,” in Power Electronics

and Motion Control Conference (IPEMC), 2012 7th International, 2012, vol. 2, pp. 1210 –1215.

[52] D. A. Khaburi, “Software-Based Resolver-to-Digital Converter for DSP-Based Drives Using an Improved Angle-Tracking Observer,” IEEE Transactions on Instrumentation and Measurement, vol. 61, no. 4, pp. 922–929, Apr. 2012.

[53] K. Bouallaga, L. Idkhajine, A. Prata, and E. Monmasson, “Demodulation methods on fully FPGA-based system for resolver signals treatment,” in 2007 European Conference on Power Electronics and Applications, 2007, pp. 1–6.

[54] A. Ziarani and A. Konrad, “A method of extraction of nonstationary sinusoids,” Signal Processing, vol. 84, no. 8, pp. 1323–1346, Aug. 2004.

[55] L. Pellecchia, Differential coils to oppose polar flux asymmetry in synchro and resolver transmitters. Google Patents, 1966.

[56] Phyu, H.N.; Aung, N.L.H.; Bi, C., "Influence of Winding Structure and the Effect of MMF Harmonics to the Spindle Motor Performance for Ultrahigh TPI HDD," Magnetics, IEEE Transactions on , vol.49, no.6, pp.2776,2781, June 2013.

[57] J. G. Zhu, Y. G. Guo, Z. W. Lin, Y. J. Li, and Y. K. Huang, “Development of PM Transverse Flux Motors With Soft Magnetic Composite Cores,” IEEE Transactions on Magnetics, vol. 47, no. 10, pp. 4376–4383, Oct. 2011.

[58] D. Živanovic, J. Lukic, and D. Denic, “A Novel Linearization Method of Sin/Cos Sensor Signals Used for Angular Position Determination.”

[59] I. Tsals, “Resolver having planar windings,” 5239288, 24-Aug-1993.

[60] J. G. Weit, “Brushless printed circuit resolver,” 4092579, 30-May-1978.

[61] L. Hultman and Z. Ye, “Soft Magnetic Composites-Properties and Applications,” Advances in Powder Metallurgy and Particulate Materials, no. 14, pp. 14–26, 2002.

[62] E.C.W. de Jong, J.A. Ferreira, P. Bauer, “3D Integration with PCB Technology”, Applied Power Electronics Conference and Exposition, 2006. APEC ’06. Twenty-First Annual IEEE, 19-23 March 2006.

[63] W. G. Hurley and W. H. Wölfle, Transformers and Inductors for Power Electronics: Theory, Design and Applications. Wiley, 2013.

[64] M. Kamon, M. J. Tsuk, and J. K. White, Fasthenry: a multipole-accelerated 3-d inductance extraction program, 42(11994), no. 9, 1750-1758.

[65] A. Ruehli, G. Antoninin, J. esch, J. Ekman, A. Mayo, and A. Orlandi, “Nonorthogonal PEEC formulation for time-and frequency-domain EM and circuit modeling,” IEEE Trans. Electroamagn, Compat., vol.45, no.2, pp.167-179, 2003.

[66] http://www.ipc.org/TOC/IPC-2221B.pdf, .Web, Mar 8, 2014.

[67] http://www.ipc.org/3.0_Industry/3.5_Councils_Associations/3.5.0_IPC/SPVC/0607/IPC-9592-Final-Draft-0407.pdf, .Web, Mar 8 2014.

Author's publications

Journal

[1] Aung, N.L.H.; Bi, C.; Al Mamun, A.; Soh, C.S.; YinQuan, Y., "A Demodulation Technique for Spindle Rotor Position Detection With Resolver," *Magnetics, IEEE Transactions on* , vol.49, no.6, pp.2614,2619, June 2013.

[2] Phyu, H.N.; Aung, N.L.H.; Bi, C., "Influence of Winding Structure and the Effect of MMF Harmonics to the Spindle Motor Performance for Ultrahigh TPI HDD," Magnetics, IEEE Transactions on , vol.49, no.6, pp.2776,2781, June 2013.

[3] N.L.H. Aung, C. Bi, A. Al-Mamun, "Initial Calibration and Online Error Compensation of a Resolver System", Key Engineering Materials, Vol. 605, pp. 523-526, Apr. 2014 .

Conference

[1] Aung, N.L.H.; Bi, C.; Al-Mamun, A.; Soh, C.S.; YinQuan Yu, "A demodulation technique for spindle rotor position detection," APMRC, 2012 Digest , vol., no., pp.1,2, Oct. 31 2012-Nov. 2 2012.

[2] Nay Lin Htun Aung, Bi Chao and Abdullah Al Mamun, "Initial Calibration and Online Error Compensation of a Resolver System", 3rd International Conference on Materials and Applications for Sensors and Transducers (ICMAST), Prague, 13-17th September, 2013.

[3] Aung, N.L.H.; Bi, C.; Yu, Y.Q.; Jang, Q.; Al-Mamun, A.; Lim, C.P., "Synthesis of a novel linear-rotary electromagnetic induction sensor using printed circuit coils," *Magnetics Symposium 2014 - Celebrating 50th*

Anniversary of IEEE Magnetics Society (MSSC50) , vol., no., pp.1,2, 22-23 Sept. 2014 doi: 10.1109/MSSC.2014.6947687

Appendix A

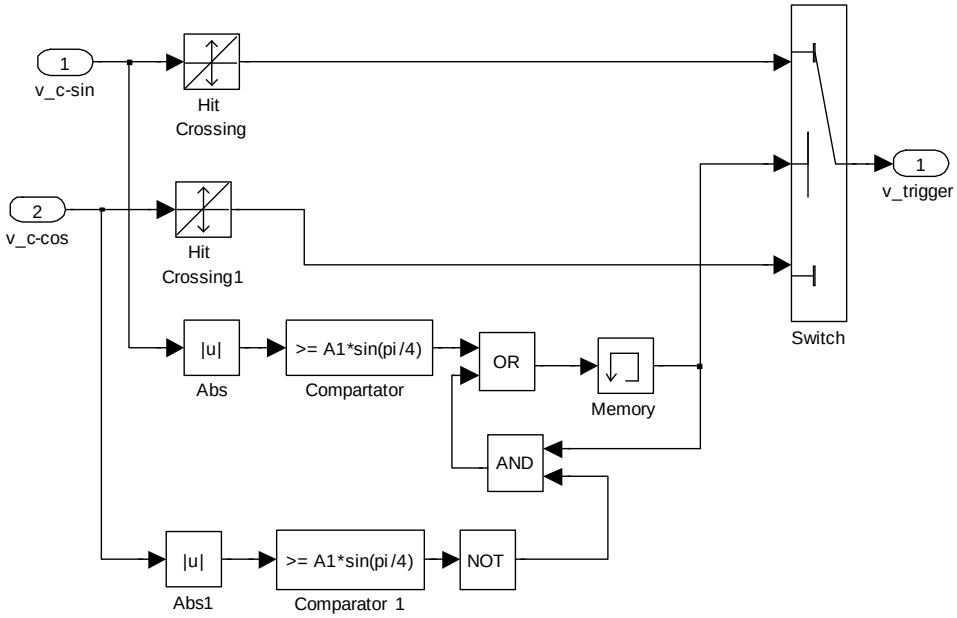

Figure. A1. Simulink model for TIRS

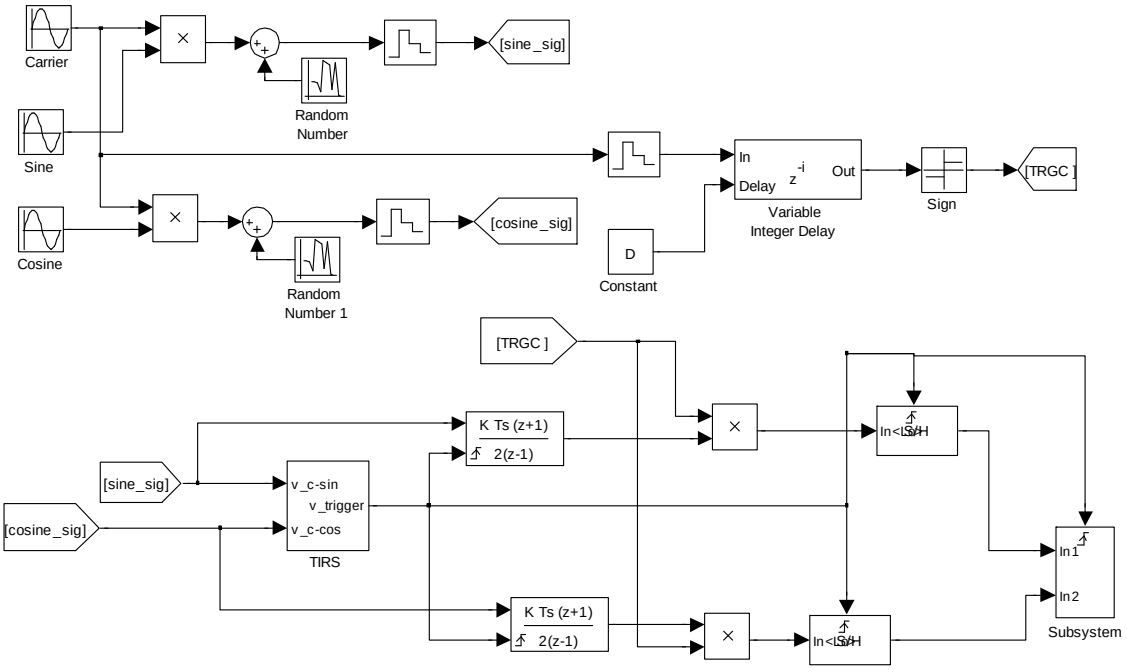

Figure. A2. Simulink model for DBSI

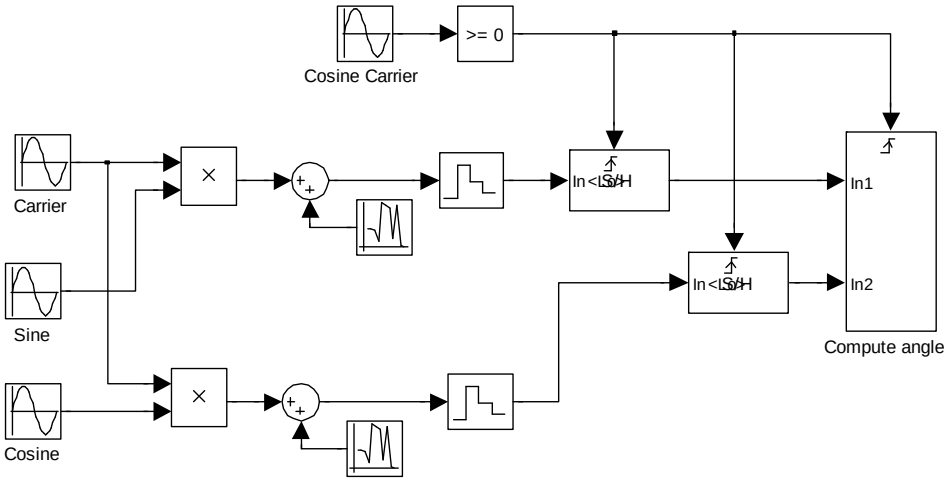

Figure. A3.Simulink model for demodulation by synchronous peak detection

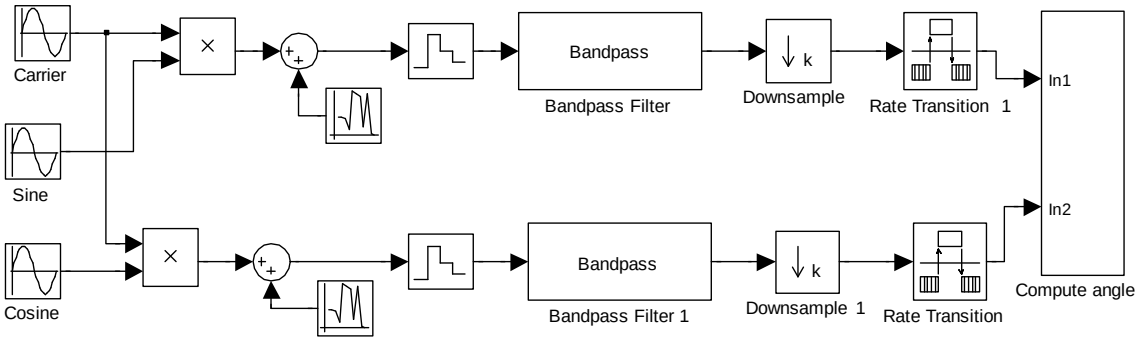

Figure. A4. Simulink model for demodulation by FIR decimation

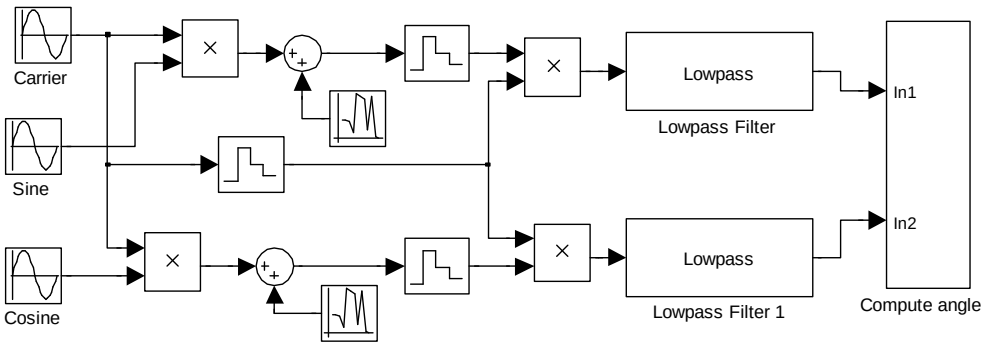

Figure. A5. Simulink model for demodulation by product detection

Appendix B

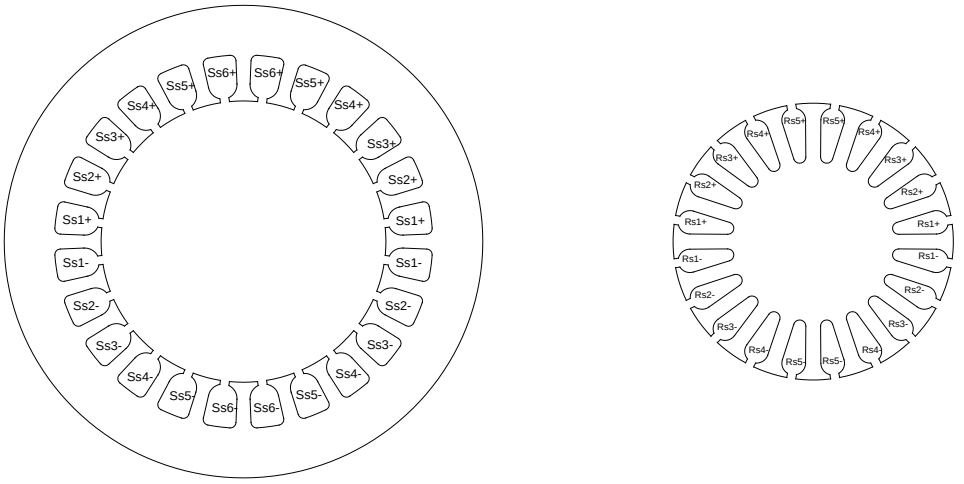

Slot	Number of turns	Slot	Number of turns
Ss1:	13	Rs1:	11
Ss2:	39	Rs2:	33
Ss3:	61	Rs3:	51
Ss4:	80	Rs4:	64
Ss5:	93	Rs5:	72
Ss6:	100		

Figure B. 1. Winding distribution in stator and rotor

Table B. 1. Resolver Specifications

Model	J36XFW001
Rated Excitation Voltage	4V
Rated Excitation Frequency	5000Hz
Phase shift	2.43 degrees
Accuracy	+/- 5.5 min
Null Voltage	17 mV

Technical Data

Models	M-037.00	M-037.DG	M-037.PD	M-037.2S	Units
Rotation range	Continuous	Continuous	Continuous	Continuous	
Design resolution	-	0.59 (34 x 10^{-6})	8.75 (0.0005)	1.75 (0.0001)	µrad (deg)
Min. incremental motion	-	5	8.75	17.5	µrad
Unidirectional repeatability	-	30	30	30	µrad
Backlash	-	200	200	200	µrad
Max. velocity	-	6	45	10	deg/sec
Wobble	< 150	< 150	< 150	< 150	µrad
Maximum axial force	±300	±300	±300	±300	N
Maximum torque (θ_x, θ_y)	±3	±3	±3	±3	Nm
Maximum torque CW**	1	1	1	1	Nm
Maximum torque CCW**	0.5	0.5	0.5	0.5	Nm
Encoder resolution	-	2000	4000	-	counts/rev.
Motor resolution	-	-	-	20000*	steps/rev.
Gear ratio	-	$(28/12)^4$:1 ≈29.6:1	-	-	
Worm Gear ratio	180:1	180:1	180:1	180:1	
Nominal motor power	-	3	30 ***	- *	W
Motor voltage range	-	0 to ±12	0 to ±24	24 *	V
Weight	0.3	0.65	0.62	0.64	kg
Body material	Al	Al	Al	Al	
Recommended motor controller	-	C-842, C-844, C-860	C-842, C-844, C-860	C-600, C-630	

** 2-phase stepper, 24 V chopper voltage, max. 1.5 A / phase, 20,000 microsteps with C-600, C-630 controllers;*
*** CW: clockwise; CCW: counter-clockwise;*
**** ActiveDrive™ (integrated PWM servo amplifier)*

Figure B. 2. Technical data of rotation stage